MEASURING THE SPATIOTEMPORAL ELECTRIC FIELD OF ULTRASHORT PULSES WITH HIGH SPATIAL AND SPECTRAL RESOLUTION

A Thesis
Presented to
The Academic Faculty

by

Pamela Bowlan

In Partial Fulfillment
of the Requirements for the Degree
Doctor of Philosophy in the
School of Physics

Georgia Institute of Technology
May 2009

MEASURING THE SPATIOTEMPORAL ELECTRIC FIELD OF ULTRASHORT PULSES WITH HIGH SPATIAL AND SPECTRAL RESOLUTION

Approved by:

Professor Rick Trebino, Advisor
School of Physics
Georgia Institute of Technology

Professor John Buck
School of Electric and Computer Engineering
Georgia Institute of Technology

Professor Steven Ralph
School of Electric and Computer Engineering
Georgia Institute of Technology

Professor Jennifer Curtis
School of Physics
Georgia Institute of Technology

Professor Mike Chapman
School of Physics
Georgia Institute of Technology

Date Approved: Fill-in

To my mother Wendy Applegate and my father Bill Mashburn

ACKNOWLEDGEMENTS

I would like to thank my advisor Rick for giving me an initial problem to solve that turned into a very exciting thesis project! Thank you, Rick, for your constant encouragement, advice, and the many things that you have taught me.

It has been a pleasure working with all of the other members of the Trebino lab including Mark, Aparna, Dongjoo, Xuan, Lina, Neeraj, Qiang, Saman, Selcuk, Pablo, Vikrant, Peter, and Jake. Thank you for your help, encouragement, and entertainment. I especially want to thank Pablo who was really wonderful to work with and taught me a tremendous amount especially when I was new to the lab.

I am also grateful to Linda Trebino and everyone in the School of Physics finance and main offices who have been most helpful with administrative issues.

Over the past several years I have had some really great collaborators outside of Georgia Tech! The pulse shaping and polarization measurements (see chapter 4 and section 2.3.5) were done in collaboration with Robert Levis, Matt Coughlan, and Mateusz Plewicki from Temple University. I have had a lot of help from Ulrike Fuchs at Fraunhofer Institute in Jena, Germany with the focusing pulse simulations. Most recently I have been involved in some very exciting work to measure superluminal pulses with Professor Peeter Saari and his students Heli Valtna, Peeter Piksarv, and Madis Lohmus from the University of Tartu in Estonia. All of the work shown in chapters 7 and 8 was done in close collaboration with Peeter's group.

I would also like to thank professor John Buck from Georgia Tech for very helpful discussions about fiber optics.

Thank you to Marie Thursby and everyone else from the TI:GER program and the NSF for providing me with the fellowship IGERT-0221600.

I thank the OSA for permission to use some of the text and figures from the following references [50,51,55,91].

I also owe a lot to my family, Wendy, Bill, and Kathy for their love and support. And I am very lucky to have an amazing husband John, who has not only helped me with his unending love and support, but also by answering my physics, math and programming questions. Discussions with John were especially enlightening when doing the minimization discussed in chapter 4.

TABLE OF CONTENTS

DEDICATION iii

ACKNOWLEDGEMENTS iv

LIST OF FIGURES x

SUMMARY xiv

I A QUICK INTRODUCTION TO ULTRAFAST OPTICS AND PULSE MEASUREMENT 1

1.1 Ultrashort pulses 3

1.1.1 Generation of Ultrashort pulses 3

1.1.2 Mathematical description of ultrashort pulses 5

1.1.3 Time bandwidth product 9

1.2 Measuring ultrashort pulses 10

1.2.1 FROG 12

1.3 Goals of this thesis 13

II MEASURING THE COMPLETE TEMPORAL ELECTRIC FIELD OF COMPLEX ULTRASHORT PULSES 15

2.1 Motivation 15

2.2 Spectral Interferometry 16

2.2.1 The experimental setup for spectral interferometry 17

2.2.2 Reconstructing the unknown field from the spectral interferogram 18

2.2.3 Problems with spectral interferometry 20

2.3 SEA TADPOLE 22

2.3.1 SEA TADPOLE experimental setup 23

2.3.2 Reconstructing the unknown field from the SEA TADPOLE interferogram 24

2.3.3 Other issues and comments 27

2.3.4 Testing SEA TADPOLE 28

2.3.5 Measuring shaped pulses with SEA TADPOLE 31
2.4 Conclusions 32
III SPECTRAL SUPER RESOLUTION IN SEA TADPOLE 34
3.1 Mathematical description of a spectrometer's response function . . 35
3.2 Simulations to test SEA TADPOLE's spectral resolution 38
3.3 Experimentally testing SEA TADPOLE's spectral resolution 41
3.4 Other issues and comments 44
IV MEASURING POLARIZATION SHAPED PULSES 46
4.1 Introduction 46
4.2 Method 48
4.2.1 Reconstructing the complete polarization state from the measured SEA TADPOLE traces 50
4.2.2 Experimental setup for measuring polarization shaped pulses with SEA TADPOLE 51
4.2.3 Ambiguities 52
4.3 Simulations 54
4.4 Measurements 60
4.5 Conclusions and future outlook 65
V MEASURING THE SPATIOTEMPORAL ELECTRIC FIELD OF FOCUSING ULTRASHORT PULSES 66
5.1 Introduction and background 66
5.1.1 Motivation 66
5.1.2 Numerically modeling focusing ultrashort pulses with low NA's 70
5.1.3 Radially varying group delay 74
5.2 Details of the method scanning SEA TADPOLE 75
5.2.1 Loss of the spatial phase in scanning SEA TADPOLE . . . 77
5.3 Measurements of focusing pulses 77
5.4 Measuring focusing pulses in the presence of linear spatiotemporal distortions 88
5.5 Spatial resolution in scanning SEA TADPOLE 92

5.5.1 Measuring the transfer function of an optical fiber 95
5.6 Conclusions 97
VI MEASURING THE SPATIOTEMPORAL ELECTRIC FIELD OF ULTRASHORT PULSES WITH SUB-MICRON SPATIAL RESOLUTION . . . 98
6.1 Introduction and background 98
6.1.1 Motivation 98
6.1.2 Numerically modeling focusing ultrashort pulses with high NA's 100
6.2 Experimental setup 104
6.3 Measuring the transfer function of NSOM probes 105
6.4 Experimental results 108
6.4.1 Microscope objectives 108
6.4.2 Singlet lenses 111
6.5 Other issues and comments 119
6.6 Conclusions 120
VII MEASURING THE SPATIOTEMPORAL FIELD OF ULTRASHORT BESSEL X PULSES 122
7.1 Introduction 122
7.2 Bessel pulses 123
7.3 Experimental results and numerical simulations 124
7.4 Conclusions 126
VIII DIFFRACTION IN THE TIME DOMAIN 128
8.1 Introduction 128
8.2 Boundary wave theory of diffraction 130
8.3 Measuring the spatiotemporal field of diffracted ultrashort pulses . 133
8.4 Conclusions 139
APPENDIX A EXAMPLES OF SEA TADPOLE TRACES 140
APPENDIX B ABSOLUTE PHASE DRIFT IN SEA TADPOLE 144
APPENDIX C POLARIZATION ELLIPSES 148

APPENDIX D COMPARISON OF THE NON-PARAXIAL AND THE PARAXIAL DIFFRACTION INTEGRALS 150

REFERENCES 153

LIST OF FIGURES

1.1 Plotting the complex electric field of an ultrashort pulse 7

1.2 The spectrum and temporal intensity for pulses with different TBP's 9

1.3 Experimental setup for FROG (taken from [12]) 12

1.4 Experimental setup for GRENOUILLE (taken from [35]) 13

2.1 Experimental setup for spectral interferometry 18

2.2 Schematic of FTSI 20

2.3 SEA TADPOLE experimental setup 24

2.4 SEA TADPOLE retrieval 26

2.5 SEA TADPOLE GDD measurement 29

2.6 SEA TADPOLE double pulse measurement 29

2.7 SEA TADPOLE double train of pulses measurement 30

2.8 Measured and correct spectra 31

2.9 Measured shaped pulse 33

3.1 Approximate eigenfunctions of the convolution operator 37

3.2 Examples of the $S_{unk}(\omega)$ compared to $S_{sp}(\omega)$ 39

3.3 Example of the $S_{unk}(\omega)$ compared to $S_{sp}(\omega)$ 41

3.4 Illustration of how $h(\omega)$ was measured 42

3.5 Measured temporal and spectral response functions 42

3.6 Comparison of spectrometer and SEA TADPOLE measurement of a train of pulses 44

3.7 Variation of $I_{unk}(t)$ and $S_{unk}(\lambda)$ with delay 45

4.1 Reconstructing φ_{rel} from measured SEA TADPOLE spectra 51

4.2 Schematic for measuring different field components to measure the polarization state with SEA TADPOLE 51

4.3 Error plots for determining the relative phase absolute phase have two minima when the spectral phases of $E_x(\omega)$ and $E_y(\omega)$ are the same. . 53

4.4 Simulation of reconstructing the polarization state of a Gaussian pulse with $\varphi_{rel} = 45^\circ$ and a delay between E_x and E_y. 55

4.5 Simulation of reconstructing the polarization state of a Gaussian pulse with $\varphi_{rel} = 90°$ and a delay between E_x and E_y, and chirp. 57

4.6 Simulation of reconstructing the polarization state of complex pulse . 59

4.7 Experimental reconstruction of an circularly polarized pulse. 61

4.8 Experimental reconstruction of an elliptically polarized pulse. 62

4.9 Experimental reconstruction of a circularly polarized double pulse. . . 64

5.1 Simulation of the focus of an ideal lens 67

5.2 Simulation of the focus of a lens with a lot of chromatic aberrations . 67

5.3 Schematic of the Fresnel integral for modeling a focusing pulse 72

5.4 Experimental setup for scanning SEA TADPOLE 76

5.5 Measured and theoretical spatiotemporal field of a pulse focused with an aspheric lens 79

5.6 Measured and theoretical spatiotemporal field of a pulse focused with an achromatic doublet 81

5.7 Measured and theoretical spatiotemporal field of a pulse focused with a plano-convex lens 82

5.8 Measured and theoretical spatiotemporal field of a pulse focused with a higher NA plano-convex lens 84

5.9 Measured and theoretical spatiotemporal field of a pulse focused with a znse lens 85

5.10 (Click on the above picture to start the movie) $E(x,t)$ where each frame is a different z. 87

5.11 $E(x,z,t)$ in the focal region of beam which had angular dispersion . . 90

5.12 $E(x,z,t)$ in the focal region of beam which had spatial chirp 91

5.13 Spatial intensity measured with SEA TADPOLE for a Bessel beam . 96

5.14 Measuring the transfer function of a single mode fiber 97

6.1 Two different approaches to solving Kirchhoff's integral for a focusing beam 101

6.2 Experimental set for scanning SEA TADPOLE with an NSOM fiber probe 104

6.3 Measurement of the transfer function of two NSOM probes 106

6.4 Measured spatiotemporal field of a pulse focused with a 10X microscope objective . . . 109

6.5 Measured spatiotemporal field of a pulse focused with a 20X microscope objective . . . 110

6.6 Measured spatiotemporal field of a pulse focused with a 0.28 NA SF11 lens . . . 112

6.7 Measured spatiotemporal field of a bessel-like pulse . . . 113

6.8 Measured spatiotemporal field of a bessel-like pulse . . . 115

6.9 (Click on the above picture to start the movie) $|E(x,t)|$ where each frame is a different z. . . . 116

6.10 Measured spatiotemporal field of a 0.44 NA asphere . . . 117

6.11 (Click on the above picture to start the movie) $E(x,t)$ where each frame is a different z. . . . 118

7.1 Measurement (left) and simulations (right) of a Bessel pulse . . . 125

8.1 One-dimensional diffraction examples . . . 129

8.2 Simulation of Diffraction of ultrashort pulses off of a circular aperture using the boundary wave diffraction integral (Image taken from ref [114]) 131

8.3 Illustration of the propagation speed of the boundary wave along the z axis. The arrows indicate the path length for the spherical waves that add up to make this wave. The Gray lines represent the plane waves that illuminate and propagate through the aperture. . . . 132

8.4 Experimental setup for measuring diffracted pulses with SEA TADPOLE 133

8.5 Diffraction boundaries used for the measurements in this chapter . . . 134

8.6 Measured $|E(x, y = 0, t)|$ after propagating through a circular aperture (Color is intensity). . . . 135

8.7 Measured $|E(x,t)|$ after propagating through a circular aperture (Color is intensity). . . . 136

8.8 Measured $|E(x,t)|$ after propagating through a leaky annular slit. . . . 138

A.1 Example SEA TADPOLE traces (simulations) . . . 141

A.2 Example SEA TADPOLE traces (simulations) . . . 142

A.3 Example SEA TADPOLE traces (simulations) . . . 143

B.1 Measured phase drift in our interferometer . . . 144

B.2 Effect of the absolute phase drift on the measured spatial phase . . . 145

B.3 Effect of the absolute phase drift on the measured spatial phase . . . 146
B.4 Effect of the absolute phase drift on the measured spatial phase . . . 146
C.1 Polarization eclipses for various polarization states 149
D.1 Simulations of the focal region of an aspheric lens with NA=0.2 . . . 150
D.2 Simulations of the focal region of an aspheric lens with NA=0.4 . . . 151
D.3 Simulations of the focal region of an aspheric lens with NA=0.8 . . . 152

SUMMARY

In this thesis a powerful and practical method for characterizing ultrashort pulses in space and time is described (called SEA TADPOLE). SEA TADPOLE is a linear interferometric technique for measuring pulses that are very complex in time and/or space, and it uses a simple experimental setup.

First we focus on measuring pulses that are spatially uniform but potentially very complicated in time or frequency. We demonstrate and verify that SEA TADPOLE can measure temporal features as small as 30 femtoseconds over durations as long as 15 picoseconds, and these measurements can be made at video-rates. The spectral resolution of this device is carefully studied and we demonstrate that for certain pulses, we achieve spectral super resolution. We also develop and test an algorithm for measuring polarization shaped pulses with SEA TADPOLE.

Our simple experimental setup for SEA TADPOLE can even be used to measure the spatiotemporal electric field of ultrashort pulses at a focus. This is because SEA TADPOLE samples the field with an optical fiber which has a small core size. Therefore this fiber can be used to spatially sample the beam, so that the temporal electric field can be measured at every position to obtain $E(x, y, z, t)$. The single mode fiber can be replaced with an NSOM (Near Field Scanning Optical Microscopy) fiber so that spatial resolution as low as 500nm (and possibly lower) can be achieved. Using this device we make the first direct measurements of the compete field of focusing ultrashort pulses. These measurement can be viewed as "snap shots" in flight of the focusing pulse. Also, for the first time, we have observed some of the interesting distortions that have been predicted for focusing ultrashort pulses such as the "forerunner" pulse, radially varying group delay dispersion, and the Bessel-like

X-shaped pulse.

In addition to characterizing focused pulses with SEA TADPOLE, we have also made some of the first direct measurements of the electric field of Bessel X-pulses. We demonstrate their propagation invariance as well as their superluminal velocity. We also use SEA TADPOLE to study the "boundary wave pulses" which are due to diffraction of the laser beam off of a circular aperture and these pulses are also superluminal.

CHAPTER I

A QUICK INTRODUCTION TO ULTRAFAST OPTICS AND PULSE MEASUREMENT

Ultrashort (or ultrafast) pulsed lasers emit a continuous train of short bursts of light which last on the order of a few femtoseconds (10^{-15} s) but can be as long as 10's of picoseconds (10^{-12} s). Ultrafast lasers have many useful properties which have led to numerous applications. Their high peak power (imagine cramming all of the energy of a continuous laser into a few femtoseconds) is very useful for creating nonlinear optical effects such as filamentation (or self guiding) and high harmonic generation to produce x-rays or atto-second pusles [1, 2]. Ultrashort pulses can have a high peak power but a low average power (most of the time in the pulse train, the power is equal to 0) which is ideal for micro-machining because material can be ablated without heating it (heating is what tends to make the features larger and distorted) [3]. This property has also made ultrashort pulses very useful for imaging live cells with depth resolution in the technique known as multi-photon microscopy [4]. Ultrafast lasers have revolutionized high precision spectroscopy, because the broad spectrum of a phase stabilized laser pulse contains on the order of 10,000 very narrow spectral lines known as a frequency comb [5]. Ultrashort pulses can even be used for controlling the quantum state of molecules and the outcome of chemical reactions. When combined with an optical synthesizer (a pulse shaper) the pulses can be made into "electromagnetic catalysts" [6–10]. Because ultrashort pulses also enable femtosecond time resolution (which is the time scale over which many chemical reactions happen) these pulses can be used to study the time evolution of molecules during reactions, in what is known as femtochemistry [11]. And there are even more applications than those listed here.

To successfully work with ultrashort pulses, it is important to know and control the pulse's shape in both time and frequency including the phase of the pulse, or how its temporal shape varies with color. How do you even know if a pulse is a femtosecond pulse and not a picosecond pulse if you do not measure its temporal profile? To completely characterize a pulse, its intensity and phase as a function of time must be determined, and it is not a trivial task to measure an event that has a duration of more than three order's of magnitude shorter than the time resolution of the fastest oscilloscopes or electronics. In general to measure an event you need a shorter event. For example, high speed photography requires the use of a strobe light that turns on and off faster than the speed of what is being photographed. Of course there are no events available that are shorter than a femtosecond pulse, and usually the only event that we have that even happens on a similar time scale is the pulse itself or another similar laser pulse. So we have to use the laser pulse to measure itself. All approaches for doing this involves interacting the pulse with itself in a nonlinear crystal. Once we have a characterized laser pulse, we can use it as a reference pulse to measure other unknown pulses either through another nonlinear interaction, or by interfering the pulses with one another [12].

In 1993 the first technique for measuring the intensity and the phase of ultrashort pulses, known as FROG or Frequency Resolved Optical Gating was introduced [13]. Today it is routine to measure the temporal intensity and phase of ultrashort pulses directly out of most commercial lasers.

A lot happens to a pulse after it leaves the laser and goes through an experiment, and in fact it becomes a lot more complicated, a lot more interesting, and much more difficult to measure. For example, a pulse shaper (which is an optical synthesizer) may be used to make the pulse several picoseconds long but with femtosecond features in time in order to optimize a chemical reaction [14]. Measuring a pulse such as this could lead to insights about how reactions happen. As another example, the

focus is probably the most important place to measure the pulse because this is where everyone uses it. But focused pulses are very difficult to measure because they often have complex space-time couplings due to lens aberrations, meaning that their temporal shape varies across the focus and as it propagates, and measuring these spatial variations often requires a spatial resolution of less than 1 μm [15]. It turns out that even the diffraction that ultrashort pulses experience due to apertures produces interesting, very small, sub-pulses with superluminal speeds [16]. Studying these pulses could lead to new insights about the diffraction of light.

1.1 Ultrashort pulses

1.1.1 Generation of Ultrashort pulses

From the Fourier transform it is easy to see that to have a short pulse of light in time, it is necessary to have a broad spectrum of colors present, where all of the colors are in phase with one another, or mode-locked. Nanosecond pulsed lasers usually use what is called active mode-locking which simply involves making a continuous wave laser and then adding a fast shutter to it so that the output intensity is modulated in time so that a train of nanosecond pulses is emitted by the laser. The fastest shutters are pockels cells which involve applying a voltage to a crystal in order to quickly change its polarization axis. The pockels cell can be used as the end mirror of the laser cavity by placing it in between crossed polarizers (though configurations using parallel polarizers are also used). When an appropriate voltage is applied to the pockels cell to make it a half wave plate, the light leaves the cavity, and then the voltage is quickly turned off so that only a short burst of light escapes. This is known as Q-switching. The shortest pulses from Q-switched lasers are usually around 10-100 nanoseconds.

Passively mode-locking lasers—or using the light inside of the laser as the mode-locking signal—results in much shorter pulse durations than can be achieved with

active mode-locking. The earliest passively mode-locked lasers used what are called saturable absorbers to make the laser emit shorter pulses. Saturable absorbers absorb light when its intensity is below a certain thresh hold, but become saturated and thus transparent for light above the intensity threshold [17]. Therefore if you have a long pulse of light in time (imagine that it is shaped like a Gaussian), the saturable absorber will absorb the light at early and later times where its intensity is lower, but close to the center of the pulse where it is most intense, the saturable absorber will be transparent and not absorb any of the light. This of course makes the pulse shorter in time. Adding a saturable absorber to a laser, makes longer pulses inside of the laser shorter, and it also greatly increases the likelihood for a laser to emit shorter pulses because these experience much less loss at the saturable absorber. Pulsed solid state as well as dye lasers are built using saturable absorbers and these usually emit pulses with durations of 500fs at the shortest [17, 18].

The most commonly used femtosecond laser, and the one that was used for all of the work in this thesis is the Ti:Sa mode-locked laser [19]. Ti:Sa lasers use what is known as kerr-lens mode-locking [20, 21]. In Ti:Sa lasers, the mode locking conveniently happens in the lasing medium, or the Ti:Sa crystal. Kerr lensing is a non-linear effect that happens when intense light propagating through a crystal spatially modulates the crystal's refractive index causing the light to focus (this is also called self focusing). Because this is a non-linear process the strength of this effect depends on the intensity of the light. So the shorter the pulse, the more it is focused. Therefore, Ti:Sa lasers can be aligned to recollimate the light after the crystal accounting for the self focusing that will select shorter more intense pulses. This optimizes the laser cavity to amplify the pulsed or self focused radiation much more than the continuous light which does not self focus so it will diverge in the cavity and not overlap well with the pump laser at the gain medium. The other key ingredient in a kerr-lens mode-locked laser is dispersion compensation (see section 1.1.2) [22, 23]. Usually a

prism pulse compressor (or sometimes chirped mirrors are used) is added to the path of the laser to remove the dispersion acquired by the pulse in each pass through the crystal, so that it stays short in time and intense enough to experience self-focusing. Pulses with durations as short as 5fs have been generated with Ti:Sa lasers [24]. Ti:Sa lasers also have the nice property that their wavelength and pulse duration (or bandwidth) are tunable, and typically they have durations between 20-200fs, center wavelengths between 700 and 1000nm, and spectral bandwidths from 20-95nm. Usually Ti:Sa lasers have repetition rates around 80MHz (or one pulse every 12.5ns) and average powers around 0.5 Watts resulting in an energy of 1-10 nanojoules per pulse. It is very common to amplify Ti:Sa lasers to achieve millijoules of energy per pulse, though amplification was not necessary for any of the work done in this thesis (see for example [25, 26]).

1.1.2 Mathematical description of ultrashort pulses

To write an expression for the electric field of an ultrashort pulse we will assume that it is polarized along one direction, so that its temporal electric field can be written as a scalar. Even focused pulses with numerical apertures less than 0.8 can still be approximated well with a scalar field (see chapter 6). In chapter 4, when we deal with polarization shaped pulses, we will write the field with two scalar equations, one for the x component and one for the y component. The equation for the field of an ultrashort pulse is shown below.

$$\mathscr{E}(t) = \frac{1}{2}\sqrt{I(t)}\exp\left(\omega t - \phi(t)\right) + c.c \tag{1.1}$$

In the above equation, $I(t)$, $\phi(t)$, are the temporal intensity and phase of the pulse and ω_0 is the carrier frequency in radians per second. It is conventional, and much more convenient to leave out the complex conjugate and only work with the complex field of the pulse and to leave out the high carrier frequency as shown in equation 1.2.

$$E(t) = \sqrt{I(t)}\exp\left(-i\phi(t)\right) \tag{1.2}$$

The field $E(t)$, is the one that we will work with most of the time. $E(t)$ can be fourier transformed to the frequency domain to get the following field for the pulse as a function of frequency.

$$E(\omega - \omega_0) = \sqrt{S(\omega - \omega_0)} \exp\left(-i\varphi(\omega - \omega_0)\right). \tag{1.3}$$

In Eq. 1.3, $\varphi(\omega - \omega_0)$ is the spectral phase and $S(\omega - \omega_0)$ is spectral intensity or the spectrum. The FWHM or rms width of the spectrum is referred to as the bandwidth. Though, technically $E(t)$ Fourier transforms to $E(\omega - \omega_0)$, most of the time we will plot the spectral field as $E(\omega)$ or $E(\lambda)$ (λ is the wavelength) so that the center frequency or wavelength can be seen.

Figure 1.1 illustrates the difference in plotting the real part of field as opposed to the intensity and the phase separately for a chirped pulse (meaning that different colors arrive at different times). It is conventional to plot the intensity and the phase separately because this is easiest to interpret and unambiguously displays all of the information about the pulse.

The spectral phase of the pulse is often approximated by the first few terms in a Taylor expansion of $\varphi(\omega)$ about $\omega = \omega_0$ as shown below.

$$\varphi(\omega) = \frac{d\varphi}{d\omega}\Big|_{\omega_0}(\omega - \omega_0) + \frac{1}{2}\frac{d^2\varphi}{d\omega^2}\Big|_{\omega_0}(\omega - \omega_0)^2 + \frac{1}{6}\frac{d^3\varphi}{d\omega^3}\Big|_{\omega_0}(\omega - \omega_0)^3 + ... \tag{1.4}$$

The first order coefficient is the group delay or the arrival time of the pulse. The second order coefficient, or $\frac{d^2\varphi}{d\omega^2}\Big|_{\omega_0}$ is referred to as linear chirp. If this term is present then the pulse's arrival time will vary linearly with frequency. Note that this term is also referred to as the group delay dispersion (GDD), though GDD is usually refers to the second order phase introduced to the pulse by a medium or a device (often due to a frequency dependent refractive index). The examples in Fig. 1.1a are for a positively chirped pulse. In Fig. 1.1a, the real part of the field shows that the oscillations have a lower frequency at earlier times, or that the redder colors are ahead of the bluer colors, due to the positive chirp. In Fig. 1.1d, you can see that this corresponds to a

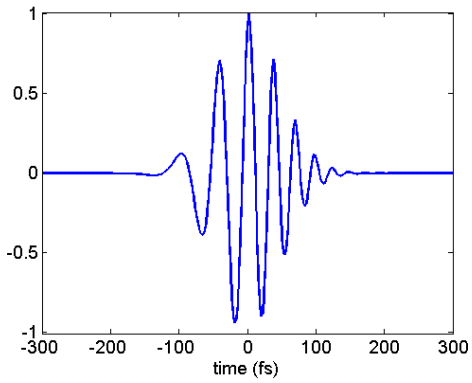

(a) The real part if $E(t)$

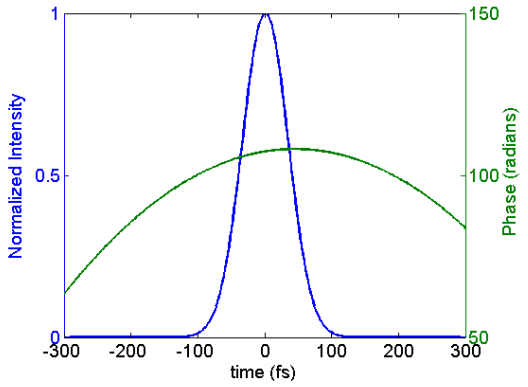

(b) The intensity and phase of $E(t)$

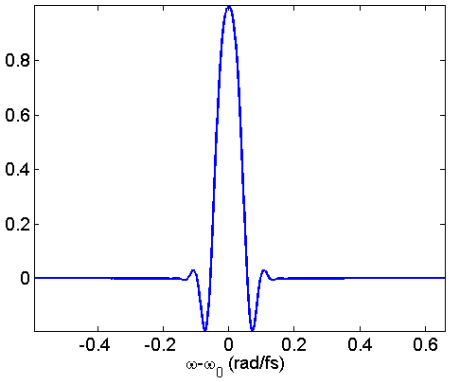

(c) The real part if $E(\omega - \omega_0)$

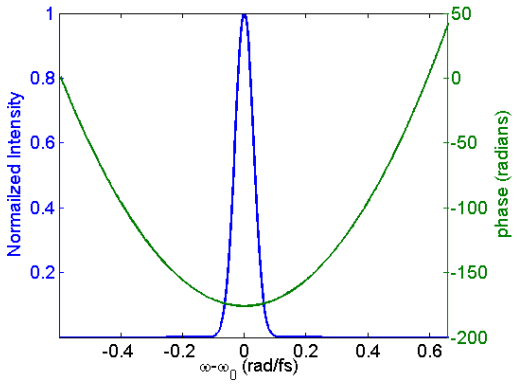

(d) The intensity and phase of $E(\omega - \omega_0)$

Figure 1.1: Plotting the complex electric field of an ultrashort pulse

quadratic spectral phase. When there are higher order terms in Eq. 1.4, the chirp can be nonlinear, or the arrival time of the pulse can vary nonlinearily with frequency.

Because we will be dealing with pulses whose electric fields may vary in time and contain couplings between time and space (or frequency and space), we need to define the electric field as a function of space. Below we show the equation of the spatiotemporal electric field of the pulse where $\varphi(\omega, x, y, z)$, is referred to the spatiospectral phase.

$$E(\omega, x, y, z) = \sqrt{S(\omega, x, y, z)} \exp\left(-i\varphi(\omega, x, y, z)\right) \tag{1.5}$$

$$E(t, x, y, z) = \sqrt{I(x, y, z, t)} \exp\left(-i\phi(t, z, y, z)\right) \tag{1.6}$$

Most of the time we will discuss the spatiotemporal field at a fixed value of z, where z is the propagation direction of the pulse, and in all of the cases that we have considered here, the x and y parts of the field were separable. The spatiospectral phase is also best understood in terms of coefficients in a Taylor expansion which is shown below considering only the x and the ω dependence of the field [27].

$$\begin{aligned}\varphi(\omega, x) = \frac{\partial^2\varphi}{\partial\omega\partial x}x(\omega-\omega_0) + \frac{\partial^2\varphi}{\partial\omega^2}(\omega-\omega_0)^2 + \frac{\partial^2\varphi}{\partial x^2}x^2 + \\ \frac{\partial^2\varphi}{\partial x^2\partial\omega}x^2(\omega-\omega_0) + \frac{\partial^2\varphi}{\partial x^2\partial\omega^2}x^2(\omega-\omega_0)^2 + ...\end{aligned} \tag{1.7}$$

This expansion shows the first order coupling terms in the phase, where the coefficient of the $x\omega$ term is known as the wave front tilt dispersion [27]. While first order spatiotemporal couplings are usually due to the beam propagating in the presence of angular dispersion [27–29], the next order terms are commonly introduced by lenses and will be discussed in more detail in chapters 5 and 6. The terms on the second line are some of the higher order couplings that are introduced by lenses with the ωx^2 term which is radially varying group delay and the $\omega^2 x^2$ term which is radially varying group delay dispersion. There are also spatiotemporal coupling terms such as these that can be found in the intensity.

1.1.3 Time bandwidth product

The time bandwidth product (TBP) is a useful metric for describing how complicated a pulse is in time or frequency, because it gives a rough estimate of the number of sub-peaks that there are within the pulse. The TBP is defined as the width of $S(\omega)$ times the width of $I(t)$. The width can be defined in many different ways, such as the rms width (which is best for complicated pulses), or the FWHM (the full width at half maximum), or any other definition). It is easy to show from the Fourier transform that there is an uncertainty principle associated with the TBP, or that it has to be greater than a minimum value. These vary with the definition of width and if rms width is used then $TBP \geq \frac{1}{2}$ or if FWHM (the full width at half maximum) definition is used then, $TBP \geq 2.76$ (we are using angular frequency here, as usual) [12]. The figure below shows some examples of pulse shapes corresponding to different time bandwidth products. This figure nicely illustrates that the TBP is approximately

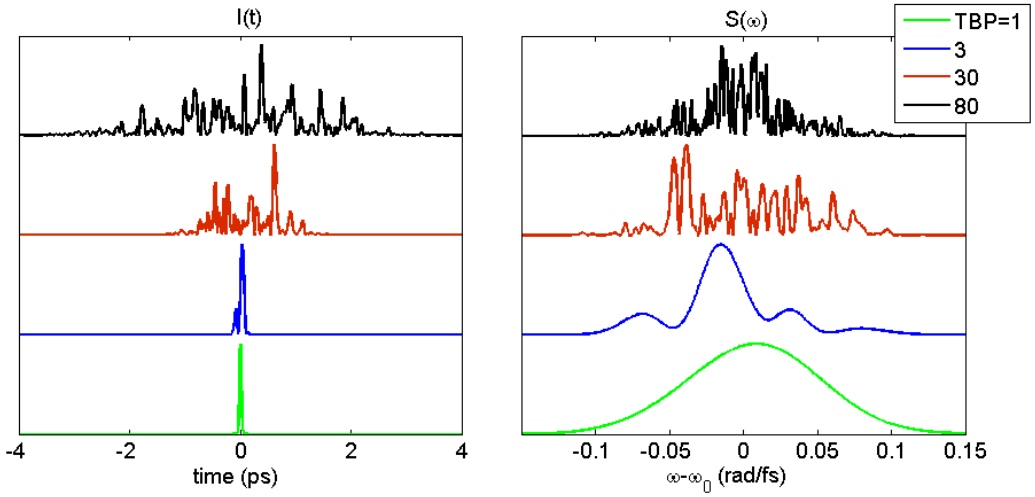

Figure 1.2: The spectrum and temporal intensity for pulses with different TBP's

consistent with the number of peaks that there in the pulse. Figure 1.2, also shows that as the size of the features in the spectral field decrease, the temporal duration (or temporal spread) of the pulse increase. This is also a result of the uncertainty

principle, and the smallest feature in the spectrum is approximately equal to one over the pulse duration (or $\delta\lambda \approx \frac{1}{\Delta t}$).

1.2 Measuring ultrashort pulses

To measure an ultrashort pulse (assuming that it is spatially homogenous), its intensity and phase must be determined. This can be done in the frequency domain or the time domain, because these fields contain the same information, and one can be obtained by Fourier transforming the other. So everything in either Eq. 1.2, or Eq. 1.3 must uniquely determined. If the field is not spatially homogenous, or if spatiotemporal couplings might be present, the field cannot just be measured at one spatial position, because the time duration, or the spectrum could vary with position along the beam. So in this case the complete field versus space and time or frequency (see Eq. 1.5) must be measured (again in either domain) though the z dependence is not necessary to measure, because the diffraction integral can be used to propagate this field to another value of z. Also, if the beam can safely be assumed to have cylindrical symmetry, then it is only necessary to measure $E(x, y = 0, \omega)$ or $E(x, y = 0, t)$ (or the y dependence can equivalently be determined).

In general, there are two ways to characterize ultrashort pulses, either through a nonlinear interaction or linearly with interference (some methods use a combination of these two approaches [30]). If there is no pre-characterized reference pulse available, then the pulse must be used to measure itself. These so called self-referential techniques require a nonlinear interaction, and it is not possible to self-referentially measure a pulse with a linear method [31].

While self-referential techniques such as FROG work very well for simple pulses (TBP$<$ 30), they are often slow, or non-convergent for very complicated pulses (TBP$>$ 100) [32]. Also, because they are nonlinear, they are much less sensitive than interferometric techniques which have been used to measure pulses with as little

energy as few zeptojoules (zepto=10^{-21}) while nonlinear techniques have measured pulses in the attojoule range at the best [33].

Also note, that pulse measurements techniques like FROG, that require scanning, work under the assumption that all of the pulses in the pulse train are identical. These so called "multi-shot" techniques average over billions of pulses to make a measurement. But some pulse measurement techniques like GRENOUILLE (see section 1.2.1) can measure the pulse in a single camera frame. These so called "single shot" techniques provide the option of measuring a single, isolated pulse in the pulse train. Single shot measurements are necessary for very low repetition rate lasers, or if there are reasons to suspect that all of the pulses in the pulse train are not identical.

In this thesis, our approach for measuring high TBP pulses with spatiotemporal couplings is to use a spatially and temporally simple (low TBP) reference pulse to measure the spatial and temporal profile complicated unknown pulse. The pulse directly out of the laser can often be used as the reference pulse, as long as it contains all of the colors that are in the unknown pulse. We do this by measuring the interference of the unknown and reference pulses (see chapter 2). Interference only allows the measurement of the spectral phase difference between the unknown and reference pulse, or it measures the spectral phase acquired by the pulse after propagating through an optical element, pulse shaper or experiment (what is measured can also be thought of as the response function). While this information is useful for certain applications such as pulse shaping, or characterizing lenses, to determine the phase of the unknown pulse, the phase of the reference pulse must be known. But the reference pulse is simple, so it is easy to measure with FROG. Since we will sometimes use FROG (or its experimentally simplified counter part GRENOUILLE) to measure the reference pulse, it is briefly described below.

1.2.1 FROG

The most common and most reliable self-referential technique is Frequency Resolved Optical Gating or FROG. There are several different types of FROG techniques, and the most common one is SHG FROG which involves measuring the spectrally resolved intensity autocorrelation of the pulse. This is done by crossing the pulse with itself in a nonlinear crystal. A second harmonic signal is created if the two pulses overlap in time, and the spectrum of this second harmonic signal is measured. A delay stage is used so that the spectrum of the autocorrelation of the pulse can be measured at every delay. This is illustrated in the Fig. 1.3. Once the FROG trace is measured, an

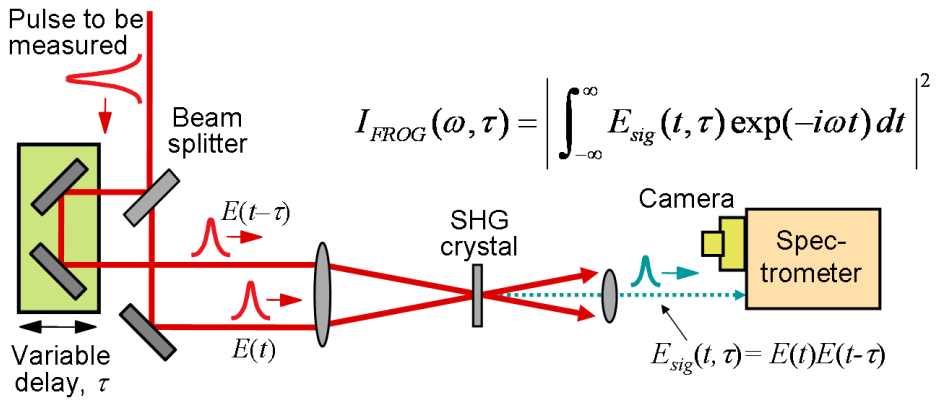

Figure 1.3: Experimental setup for FROG (taken from [12])

iterative algorithm is used to essentially, uniquely determine the intensity and phase of the pulse [32].

It is also possible to make a SHG FROG trace using a simplified, single shot experimental setup called GRENOUILLE, which is shown in Fig. 1.4 [34, 35]. It turns out that the delay stage can be replaced with a fresnel biprism, which can map delay onto the vertical axis of a camera so that the autocorrelation can be generated in a single shot. And if a thick SHG crystal is used each color will leave the crystal at a different angle along the direction that the beam is focused (the horizontal axis) due to phase matching. This can be used to map color to the camera's horizontal position,

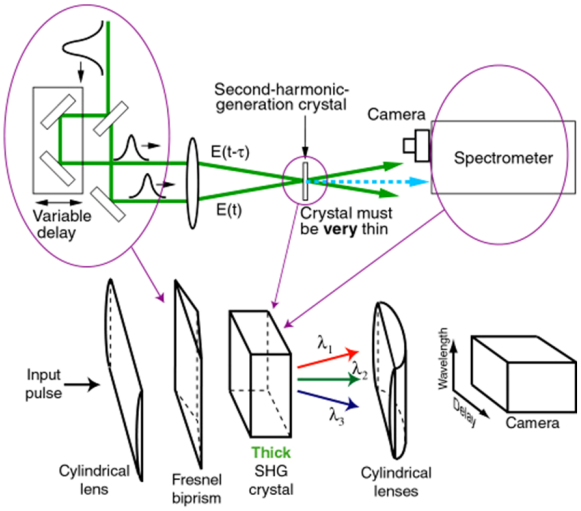

Figure 1.4: Experimental setup for GRENOUILLE (taken from [35])

so that we get the spectrum of the autocorrelation at each delay, or the FROG trace in a single camera frame. The same retrieval algorithm is used to reconstruct the intensity and phase from the FROG trace. Typically, GRENOUILLE can measure pulses with TBP's less than 10, and our reference pulse is usually much simpler than this.

1.3 Goals of this thesis

The goals of this thesis are to develop a technique that can measure pulses that are very complicated in time such as shaped pulses. Additionally, we need the option of being able measure the pulse when its temporal field varies with polarization. We would also like to able to measure ultrashort pulses at a focus (which might also be shaped), where the pulse can be both complicated in space and time, and contain complicated space-time couplings (due to commonly occurring lens aberrations). Because it is possible to focus a beam down to a spot size of $\lambda/2$ we will need to have sub-μm spatial resolution. Therefore we would like to develop, demonstrate and thoroughly test a technique for measuring the spatiotemporal electric field of ultrashort pulses with femtosecond temporal resolution, picosecond temporal range,

sub-μm spatial resolution, and a large acceptance angle (meaning that it is able to collect a large range of k-vectors).

CHAPTER II

MEASURING THE COMPLETE TEMPORAL ELECTRIC FIELD OF COMPLEX ULTRASHORT PULSES

2.1 Motivation

Many applications of ultrashort pulses, such as coherent control of quantum dynamics [14, 36–38] or multi-photon microscopy [39, 40], utilize very complicated shaped pulses. To optimize these experiments, it is important to be able to completely characterize these complicated pulses. Coherent control experiments use feedback loops to select the appropriate pulse shape, and usually pulse measurement is a required part of these loops. Therefore a fast (video-rate) pulse measurement technique that is capable of measuring shaped pulses would be very useful for these experiments and before the work in this thesis was done, there was no such technique.

Shaped pulses have small features in their spectrum or spectral phases making them longer in time (as long as 10ps) and therefore they have a large time bandwidth product (this is what we mean by complicated). There are three techniques that are good candidates for measuring shaped pulses: frequency-resolved-optical gating (FROG) [12], cross-correlation FROG (XFROG) [41], and spectral interferometry (SI). FROG techniques, while quite fast for simple pulses (TBP < 10), are much slower or even non-convergent for more complex pulses. SI has the advantage that it is inherently a single-shot technique and the interferogram can be directly and quickly inverted regardless of the complexity of the pulse. Therefore SI could in principle be used to measure very complicated pulses in real-time. Another useful property of SI is that it is a linear and heterodyne technique, and so it is extremely sensitive and can measure pulses that are approximately nine orders of magnitude weaker than those

that can be measured using nonlinear-optical methods(like FROG) [33].

SI's only fundamental drawback is that it requires a reference pulse that contains all of the colors of the unknown pulse[1]. This is because, like all interferometers, with SI you can only measure the phase difference between the interfering fields, or $\varphi_{unk}(\omega) - \varphi_{ref}(\omega)$ is what is measured rather than just $\varphi_{ref}(\omega)$. So if you want to know the spectral phase of the unknown pulse, then you have to know the spectral phase of the reference pulse to subtract out its contribution. But fortunately, when measuring shaped pulses, the unshaped pulse provides an ideal reference pulse, and it is easily measured using another technique, such as FROG or its experimentally simpler version, GRENOUILLE [12].

For many cases, a differential measurement in which the phase added to the pulse, or the transfer function is of interest and therefore, the phase of the reference pulse does not have to be known or removed from the measured phase difference. All of the measurement shown in this thesis are differential measurements, and this type of measurement has been useful in the past when for pulse shaping [42, 43], studying plasmas [44] and for characterizing photonics devices [45].

But, as explained in section 2.2.3, there are a few other problems with SI that we need to overcome in order to make it a practical method that is capable of measuring shaped pulses. And this is why we have developed SEA TADPOLE which is an experimentally simplified high spectral resolution version of SI which most of the work in this thesis is based on. We will discuss SEA TADPOLE in detail in section 2.3.

2.2 Spectral Interferometry

Spectral interferometry is a linear-optical technique for measuring the spectral intensity and phase of an ultrashort pulse when a characterized reference pulse is available

[1]Here we refer to the pulse that is to be measured $E_{unk}(\omega)$ as the unknown pulse and the reference pulse $E_{ref}(\omega)$ as the reference pulse.

[33, 46, 47]. SI simply involves measuring the combined spectrum of an unknown and a reference pulse where one of them is delayed by an amount τ so that the signal shown in Eq 2.1 is recorded.

$$\begin{aligned} S_{SI}(\omega) &= |\mathscr{F}(E_{ref}(t-\tau) + E_{unk}(t))|^2 \\ &= |E_{ref}(\omega)\exp i\omega\tau + E_{unk}(\omega)|^2 \\ &= |E_{ref}(\omega)|^2 + |E_{unk}(\omega)|^2 + |E_{ref}(\omega)||E_{unk}(\omega)|\cos(\varphi_{ref}(\omega) - \varphi_{unk}(\omega) + \omega\tau) \end{aligned} \tag{2.1}$$

In the above equation the first two terms are usually referred to as the "DC" component and they are the spectra of the unknown and reference pulses. The second term is what we are really interested in because it contains the spectral phase of the unknown pulse.

Another way to view the spectral interferogram is that phase difference between the interfering pulses is encoded in the the periodicity of the interference fringes. For example if $\varphi_{ref}(\omega) - \varphi_{unk}(\omega)$ is quadratic which could happen if the unknown pulse is more chirped than the reference pulse then the period of the fringes will increase linearly with omega (see the interferogram in fig. 2.2).

2.2.1 The experimental setup for spectral interferometry

In principal, the experimental setup for SI is quite simple; you just need a Mach Zender interferometer and a spectrometer. Figure 2.1 shows the typical setup that is used for an SI measurement. A first beam splitter is placed just after the laser to pick off a reference pulse and a second beam splitter recombines the unknown and reference beams and then they are sent collinearly into a spectrometer. The unknown pulse travels through some experiment and the spectral phase that the experiment introduces to the pulse is the phase of the interference fringes that can be be retrieved. There is a delay stage in the reference arm so that the the appropriate delay (see section 2.2 for a discussion of this) can be introduced to produce fringes in the spectrum with the needed frequency.

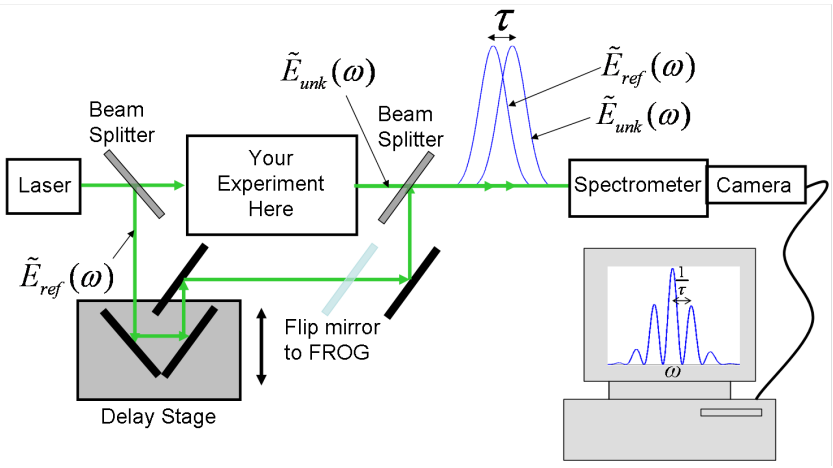

Figure 2.1: Experimental setup for spectral interferometry

2.2.2 Reconstructing the unknown field from the spectral interferogram

Once the spectral interference is recorded, the next step is to extract (or "reconstruct") the unknown electric field, $E_{unk}(\omega)$ from the interferogram. This might seem trivial to do because you could just isolate the cosine term by subtracting and dividing out the unknown and reference spectra and then take the arccosine of what is remaining. The problem with doing this is that arccosine is only defined between 0 and π and the phase is defined between $\pm\pi$. In other words if you use the arcosine to isolate $\varphi_{unk}(\omega)$ there will be a minus sign ambiguity at every value of ω. So we need a different method to do this that will both remove the DC from the measured spectra and isolate $E_{unk}(\omega)$ from its complex conjugate[2].

Fourier Transform Spectral Interferometry (FTSI) is the most commonly used reconstruction algorithm for doing this [46]. Using what is called Fourier filtering, the field of the unknown pulse is isolated from both the spectra (or the DC) and its complex conjugate. This algorithm requires that the unknown pulse be delayed by an amount τ from the reference pulse which is why the reference field is delayed in

[2]Of course if the phase only varies between 0 and π this is not a problem, but we do not want to restrict ourselves to such simple pulses.

Eq 2.1.

The FTSI algorithm is illustrated by the Fig. 2.2. The top left image shows the $S_{SI}(\omega)$ as well as the two spectra of the unknown and reference fields. The first step is to Fourier transform $S_{SI}(\omega)$ to the time domain where the data separates into three parts as shown in the top right of Fig. 2.2. At the center (because they have a frequency of 0) are the DC terms or the spectra and one of the side bands is the product of $E_{unk}(\omega)$ and $E_{ref}(\omega)^*$ and the other side band is the complex conjugate of this. This is a very nice arrangement of the data because now $E_{unk}(\omega)$ is separated from the rest of the information so we will be able to determine its phase (and intensity) without any ambiguities. Therefore the next step is to crop out either of the two sidebands and then inverse fourier transform this back to the frequency domain. At this point we are left with $E_{ref}(\omega)E_{unk}(\omega)^*$ and now we just have to divide out $E_{ref}(\omega)$ in order to isolate $E_{unk}(\omega)$. The final results (the intensity and phase of the unknown pulse) are shown at the bottom right in Fig. 2.2.

In the FTSI algorithm, both the delay and the size of the filtering window have to be chosen carefully to get the best reconstruction. Consider that the interference pattern is sampled with n points and a resolution of $\delta\omega$. If the data is filtered in the Fourier domain so that n_2 points are remaining, then after the inverse Fourier transform, the spectral resolution of the reconstructed phase will only be $\delta\omega n_2/n$. So the filtering should be done so that n_2 (or equivalently, the delay τ) is as large as possible. However, larger delays correspond to finer spectral fringes that may exceed the spectral resolution of the spectrometer, resulting in poor fringe visibility, a reduced signal-to-noise radio, and a more distorted retrieved field due to the effects of the spectral response function for larger delays.

Also note that since spectrometers linearly map position to λ rather ω, the raw data points of a measured spectral interferogram are not equally spaced with respect to ω. Yet it is $S_{SI}(\omega)$, and not $S_{SI}(\lambda)$, that needs to be Fourier transformed, and

the most common Fourier transform implementation on a computer (the fast Fourier transform, or FFT) requires that the data points be equally spaced. It is therefore necessary to interpolate the measured data set before the FFT is applied, otherwise some errors will result [48].

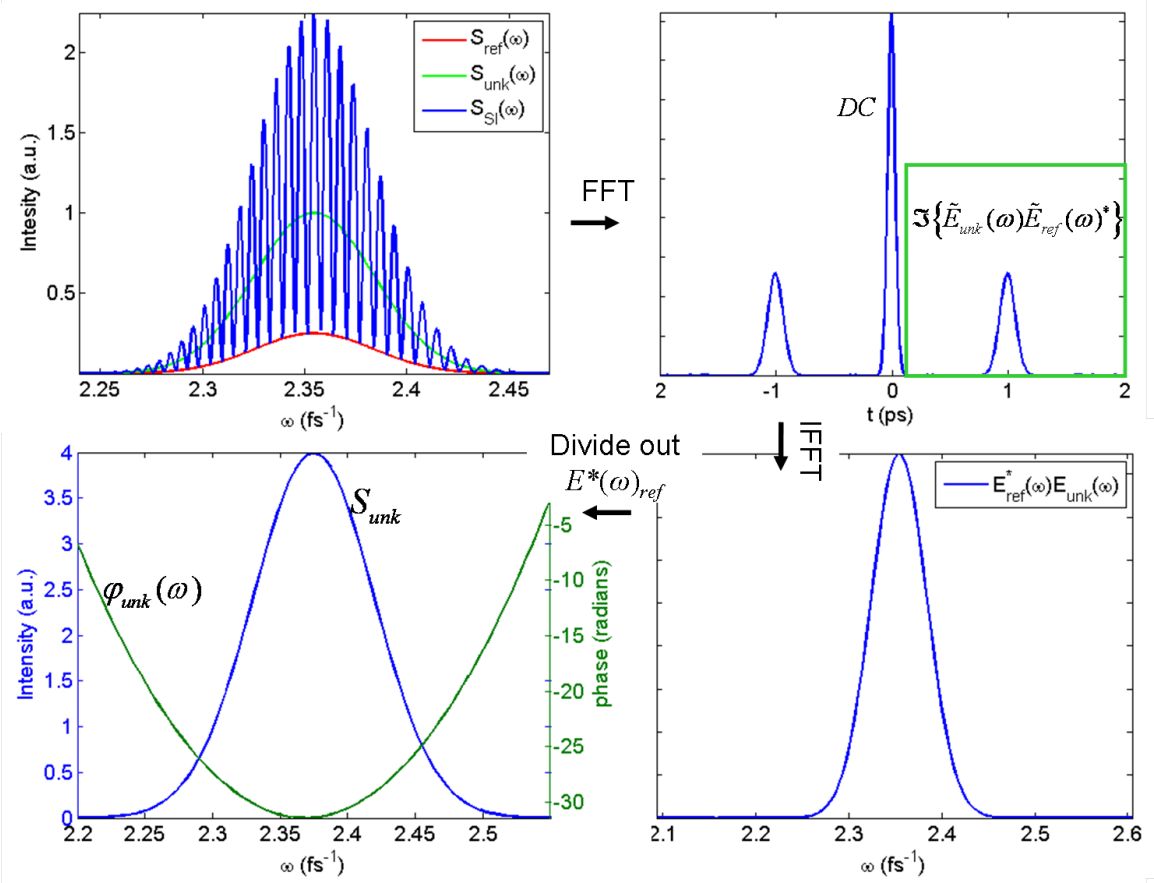

Figure 2.2: Schematic of FTSI

2.2.3 Problems with spectral interferometry

Unfortunately, SI has some serious limitations. The Fourier-transform spectral interferometry (FTSI) retrieval algorithm results in a loss of spectral resolution and temporal range due to the filtering step where one side band is isolated from the rest of the data (see the top right image in Fig. 2.2). The delay τ has to be large enough that the sidebands are completely separated from the other peaks. In theory this

means that one third of the points could kept after the filtering. But in practice the resolution suffers more due to the fact that the spectrometer's instrument response function has a greater effect on the pulse when the delay is non-zero (see chapter 3) and in practice we have found that the typical resolution loss is around a factor of 5 [33, 46, 49].

The link between spectral resolution and temporal range comes from the fact that when taking a discrete Fourier transform from t to $\nu = 2\pi\omega$, the resolution in one domain is given by the inverse of the range in the other domain. Therefore this loss of range on the time axis is equivalent to a loss in spectral resolution. So the filtering should be done so that filtering window (or equivalently, the delay τ) is as large as possible. If SI is used to measure such a pulse, then the spectrometer that we use would require a resolution that is five times smaller than the smallest feature in the spectral electric field of the pulse. For a 10ps pulse, this means that we need a spectral resolution around 0.08nm which requires using a very big, expensive spectrometer which we would like to avoid[3].

Also, while simple in principle, in practice SI has an unwieldy experimental setup. To get the best results the interfering beams must enter and travel perfectly collinearly through the spectrometer; This is difficult to set-up and maintain in the lab. The spatial modes of the interfering beams must also be identical to achieve optimal results. And because the device is an interferometer, it has to be mechanically very stable. These complexities and constraints have prevented the spectral interferometer from becoming a practical device.

SI is the best candidate for measuring shaped pulses due to its real-time retrieval speed and the fact that it is linear. Therefore we set out to develop a high spectral resolution and experimentally simple version of SI that will be described in the next

[3]To calculate this we used the formula $\delta\lambda = \frac{2\lambda^2}{\Delta T c}$ and divided this by 5. This formula will be explained in more detail in chapter 3 and can be found in reference [50].

section.

2.3 SEA TADPOLE

In this section, a version of SI called SEA TADPOLE that is both experimentally very simple and high-spectral resolution is discussed [50, 51]. This method employs a quick, direct inversion algorithm, and it measures the spectral phase with the full resolution of the spectrometer. In fact,this technique sometimes achieves better spectral resolution than that of the spectrometer involved (see chapter 3). Even more importantly, this device is very easy to use and insensitive to alignment. Therefore we expect this device to be especially useful for pulse shaping. We have tested this technique on complex pulses including shaped pulses and these measurements are shown here.

In our method the trick that we use to make the apparatus simple is that we combine the two pulses using two short, equal-length optical fibers. Also, rather than producing the interference in the spectrum, we make a spatial interferogram by crossing the two beams emerging from the fibers at a small angle. We then spectrally resolve the crossing beams, so that we have a spatial interferogram (or a hologram) for each color in the beam. This results in an interferogram much like that shown in equation 2.1 except that it is two-dimensional $S(\omega, x)$. This interferogram can be thought of as a spectrally resolved spatial interferogram (or a spectrally resolved hologram). Also unlike traditional SI, our method involves overlapping the pulses in time ($\tau = 0$) which happens to improve the spectral resolution (see chapter 3).

Spectrally resolved spatial interferometry has been used in the past, but in all of these techniques either the phase was not retrieved or complicated curve fitting methods were used [40, 52, 53]. A simpler fourier filtering technique which we use here has been demonstrated before for measuring the group velocity of a plasma [49] but not for characterizing ultrashort pulses. To retrieve the phase from $S(\omega, x)$, we

use an algorithm that Fourier filters the trace along the camera's spatial dimension, rather than the spectral coordinate (as it is done in SI), to remove the DC component and one of the interference terms without loosing any spectral resolution. In view of previous work using such a spatially encoded arrangement (SEA) and also work using the combination of SI and FROG to measure the reference pulse (called TADPOLE), we call our technique SEA TADPOLE, or Spatial Encoded Arrangement for Temporal Analysis by Dispersing a Pair of Light E-fields [33, 54].

2.3.1 SEA TADPOLE experimental setup

To make a SEA TADPOLE measurement we couple the reference and unknown pulses into two identical fibers. The output ends of the fibers are placed close together, so that when the light diverges from them, both beams are collimated with the same spherical lens (focal length f). Because the fibers are displaced from the optic axis (with a distance d between them which is usually $< 1mm$) the collimated beams cross at angle θ which is equal to $\frac{d}{f}$ and we place a camera at the crossing point in order to record their interference. In the other dimension we use a diffraction grating and a cylindrical lens to map wavelength onto horizontal position (as in a conventional spectrometer) so that we record a two-dimensional interferogram given by Eq. 2.2. Figure 2.3b illustrates the experimental setup.

Typical experimental parameters include a crossing angle of 0.06°, a camera with about 10^6 pixels, each having a pitch around 6 μm, a collimating lens with a focal length of 150 mm, 40 cm long fibers with a mode size of 5.6 μm, and we typically build the spectrometer to have a range of 80 nm and a spectral resolution of about 0.14 nm (as we will show later). The range of the wavelength axis can be decreased in order to increase the spectral resolution simply by using a longer focal length cylindrical lens, as in any spectrometer, and the usual limitations of grating spectrometers apply.

This experimental setup is very convenient to use because the beams enter it

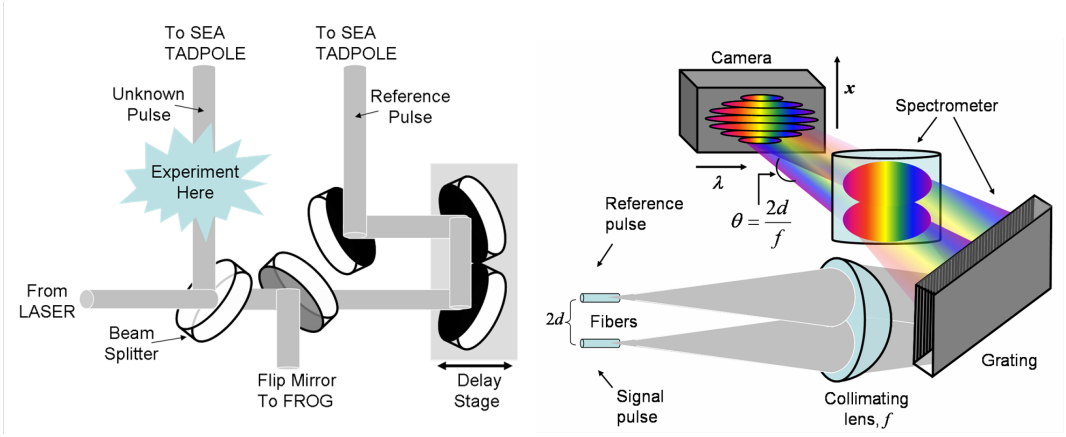

(a) Before SEA TADPOLE (b) SEA TADPOLE

Figure 2.3: SEA TADPOLE experimental setup

through fiber optics which erase the spatial dependence of the beams (such as their entrance angle or mode shape). In other words, if the reference or unknown beams move around this does not change the alignment that they take through the interferometer and therefore it does not make the measured interferogram incorrect as it would if the fibers were not present; it only attenuates the beams which is usually not a problem because cameras are very sensitive. The fibers also ensure that the interfering beams will have identical modes which optimizes the fringe contrast.

2.3.2 Reconstructing the unknown field from the SEA TADPOLE interferogram

The SEA TADPOLE interferogram described in the previous section is given by the following equation:

$$\begin{aligned} S_{ST}(\omega, x) &= |E_{ref}(\omega)\exp(i\vec{k}_{ref}\cdot\vec{r}) + E_{unk}(\omega)\exp(i\vec{k}_{unk}\cdot\vec{r})|^2 \\ &= |E_{ref}(\omega)\exp(ikxcos(\theta) + ikzsin(\theta)) + E_{unk}(\omega)\exp(-ikxcos(\theta) + ikzsin(\theta))|^2 \\ &= |E_{ref}(\omega)|^2 + |E_{unk}(\omega)|^2 + |E_{ref}(\omega)||E_{unk}(\omega)|\cos(\varphi_{ref}(\omega) - \varphi_{unk}(\omega) + kxsin(\theta)) \end{aligned} \tag{2.2}$$

In Eq. 2.2 θ is the half crossing angle, k is the wave number, x is the vertical dimension (the dimension in which the beams are crossing) and z is the propagation direction.

This is similar to the interferogram measured in SI (see 2.1), except that the light is both spectrally and spatially resolved, and there is a linear term in the position, x, in the argument of the cosine (rather than the linear term in ω due to the delay). Because we use fiber optics as the entrance to this device, all spatial information about beams is lost, and therefore we leave out the spatial dependence of the reference and unknown fields in Eq. 2.2.[4] The top right image in Fig. 2.4, shows a typical interferogram. As you can see from Eq. 2.2, the location of the maxima, or the shape of an interference fringe is the spectral phase difference between the interfering pulses. This means that spectral phase added to the pulse can be qualitatively read off of the unprocessed interferogram. The interferogram shown in Fig. 2.4 shows parabolic fringes because the unknown pulse is chirped (or it has group delay dispersion) as you can see in the image at the bottom left. See Appendix 1 to see several simulations of SEA TADPOLE traces for different pulses.

The advantages of this interferogram become apparent when we go to reconstruct $E_{unk}(\omega)$ and this is done much like that described in the following references [49, 51, 55]. First we take a 1D Fourier transform of the 2D interferogram with respect to camera's position axis, so that the Eq. 2.2 becomes:

$$\begin{aligned} S_{ST}(\omega, k_x) &= |E_{ref}(\omega)|^2 + |E_{unk}(\omega)|^2 \\ &+ E^*_{ref}(\omega)E_{unk}(\omega)\delta(k_x + 2\frac{\omega}{c}sin(\theta)) + E_{ref}(\omega)E^*_{unk}(\omega)\delta(k_x - 2\frac{\omega}{c}sin(\theta)) \end{aligned} \tag{2.3}$$

As a result, the data separates into three bands (in k_x) in which each of the two sidebands contains the complex field of the unknown pulse (see the top right image in Fig. 2.4), and we can extract the required information from either of these. The sidebands are slightly tilted because the argument of the delta function is frequency dependent, or equivalently because the fringe spacing in the x domain, is frequency

[4]The spatial dependence of the pulses is only measured so that fourier filtering can be done along the position axis and then now spectral resolution is lost in this reconstruction. We assume for the moment that the beam that we are measuring is spatially uniform. In chapters 5 and 6 we will discuss how to extend this method to measure pulses when this is not the case.

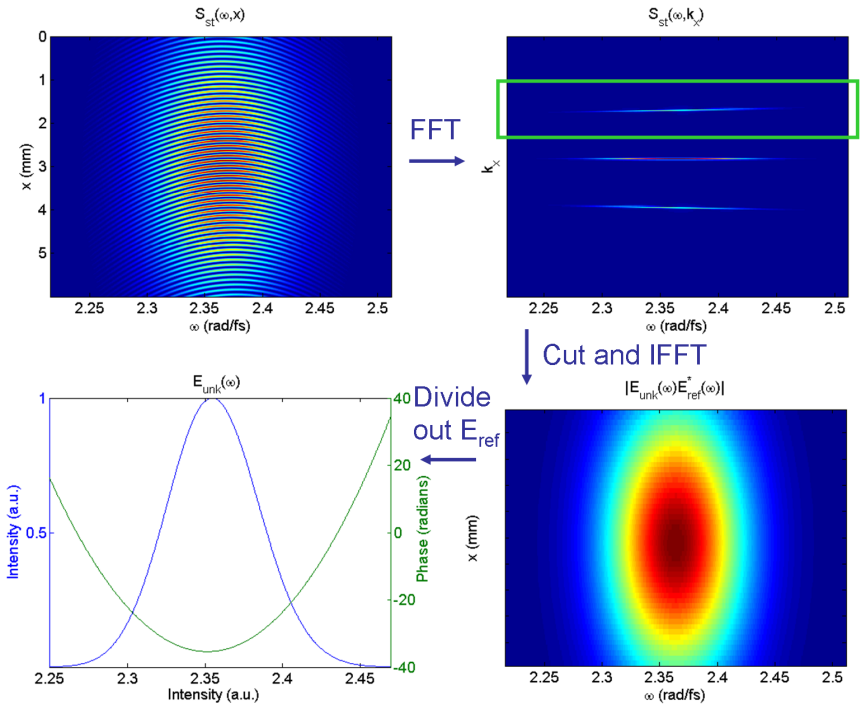

Figure 2.4: SEA TADPOLE retrieval

dependent. Although we could isolate the unknown spectral field at this point, it is easier to inverse-Fourier transform back to the x domain where the tilt becomes a small, linear phase term given by $\frac{2xsin\theta}{c}\omega$, which is small enough to neglect.[5] At this point $E_{unk}(\omega)$ can be obtained in several ways (taking one line, or averaging) and we have found that what works best (especially in the presence of noise) is to average the 2D data over x and then divide out the reference electric field. When averaging is done, it is important to average over the spectral phase and the spectrum separately otherwise the small cross term in the phase will distort the spectrum as shown in the bottom right image in Fig. 2.4. The bottom right image in this figure shows the retrieved pulse.

SEA TADPOLE's simple experimental setup (see Fig. 2.1 combined with this

[5]This linear spectral phase term will shift the origin of time axis by a small amount which is usually on the order of 100fs. This shift is unimportant because it will be the same for all measurements with a given device and therefore we can still measure relative delays or see the pulse's arrival time change.

retrieval algorithm that reconstructs $E_{unk}(\omega)$ with the full resolution of the spectrometer used to make the measurement makes this technique the first practical device for measuring ultrashort pulses with durations anywhere from 10fs-20ps.

2.3.3 Other issues and comments

Much like SI, the only requirements of the reference pulse in SEA TADPOLE are that it be from the same laser as the unknown pulse so that the interfering pulses are coherent (time-synchronized).[6] Also its spectrum must contain that of the unknown pulse (otherwise the spectral-interference term is zero at that frequency). The best reference pulse is generally the pulse taken directly out of the laser, because this is usually a spatially and spectrally smooth pulse that is easy to measure using FROG or GRENOUILLE [12]. Figure 2.3b illustrates this. If it is only necessary to determine the phase and spectrum introduced by an experiment such as some material, a lens, or a pulse shaper, then it is not necessary to characterize the reference pulse.

As long as the experimental setup is considered, there is no direction of time ambiguity in SEA TADPOLE. If the unknown pulse enters the device from the bottom fiber, then the phase difference will have the sign shown in Eq. 2.2, and it will have the opposite sign if the unknown pulse enters through the top fiber. It is also necessary to consider which interference term (in our analysis we used the top one) is used in the reconstruction because these are complex conjugates of one another so their spectral phase differences have opposite signs as illustrated by Eq. 2.3.

A calibration can be performed if the spectral phase difference between the two arms of the interferometer is not zero (possibly due to different fiber lengths) [51, 55]. This is simply done by measuring the spectral-phase difference between the two arms of the interferometer when the unknown arm also contains the reference pulse and

[6] In principle we could use a reference pulse from another laser, but the measurement would either have to be of an isolated pulse in the pulse train, or the two lasers would have to be time synchronized so that they would have the same absolute phases.

then this phase can be subtracted out from all subsequent measurements. In principle, the phase difference in the interferometer as a function of x and ω can be measured so that any spatial phase difference introduced by the interferometer is also removed. In practice, because an interferometer only measures phase differences and both beams travel through the same optics and very similar fibers, we find that it is not necessary to do the two-dimensional calibration. But the one-dimensional calibration is useful because it is difficult to cut the fibers to have the exact same lengths.

2.3.4 Testing SEA TADPOLE

We performed several measurements to demonstrate and test SEA TADPOLE using a KM Labs Ti:Sa oscillator with a center frequency of 800nm.

First, to test the accuracy of SEA TADPOLE, we measured the group delay dispersion (GDD, and also know as chirp) of a 1.85cm thick SF11 glass window by placing it in the unknown pulse arm of the device so that the phase difference between the interfering pulses yields the GDD of the glass. Figure 2.5a shows the SEA TADPOLE trace obtained in this measurement. The fringes appear parabolic, because the spectral phase difference between the unknown and reference pulses is encoded in the curvature of the fringes. Figure 2.5b shows the retrieved spectral phase of the pulse. We found the GDD to be 1840 $\frac{fs^2}{rad}$, in reasonable agreement (4% error) with the theoretical value of 1770 $\frac{fs^2}{rad}$.

To demonstrate the high spectral resolution of our technique, we measured the spectral phase of a 14 ps double pulse (two identical pulses with 14 ps between them) generated by a Michelson interferometer. See Fig. 2.6. Ordinarily, SI devices lack the spectral resolution to measure such a long pulse due to the fine structure in the pulse spectrum and spectral phase. In SEA TADPOLE, however, the spectral fringes, as well as the jumps in the spectral phase, are easily seen. To confirm that our reconstructed electric field is correct we measured the ratio of the intensities of

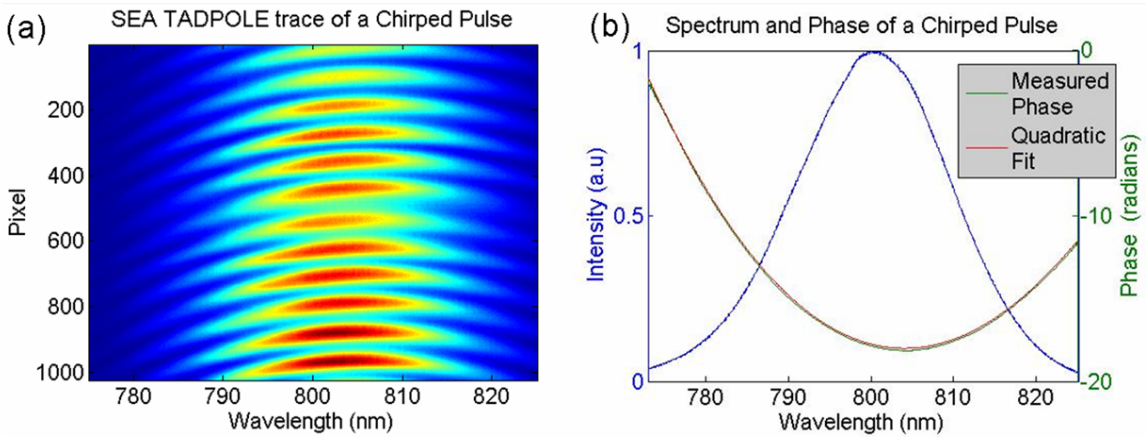

Figure 2.5: SEA TADPOLE GDD measurement

the pulses from our Michelson interferometer and found them to be 1:2, in agreement with our result shown in Fig. 2.6b. We also confirmed that the pulse separation was in fact 14 ps by making an independent measurement of the spectrum, which is shown in blue in Fig. 2.8. The inserts in Fig. 2.6b show a linear temporal phase for the pulses because our spectrum was not precisely centered on the wavelength axis.

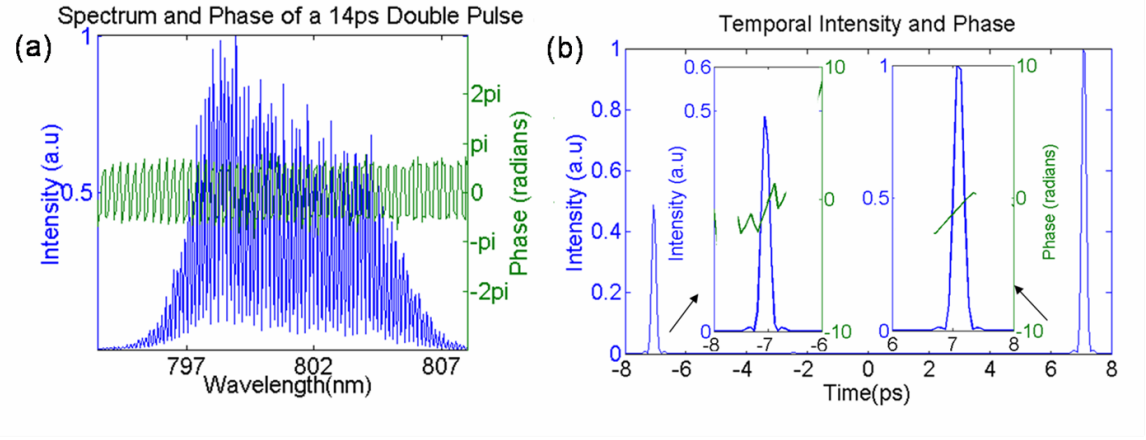

Figure 2.6: SEA TADPOLE double pulse measurement

We also measured a very complicated pulse generated by a Michelson interferometer and an etalon to produce two trains of pulses. The intensity and phase measured by SEA TADPOLE are shown in Fig. 2.7, which nicely reveals the double train of

pulses and shows the high complexity of the pulse, whose time bandwidth product is ≈ 400. The spectral phase shows the jumps of the double pulse and also a slower modulation, which is the phase introduced by the etalon. We used a well calibrated etalon whose reflectivity was 50% at 800 nm, and the spacing between the partial reflectors was 52 μm, yielding a 350 fs round trip time. The intensity of the first and second reflections of the pulse in the time domain should be 25% and 6% and this is close to what our reconstructed temporal intensity in Fig. 2.7b shows.

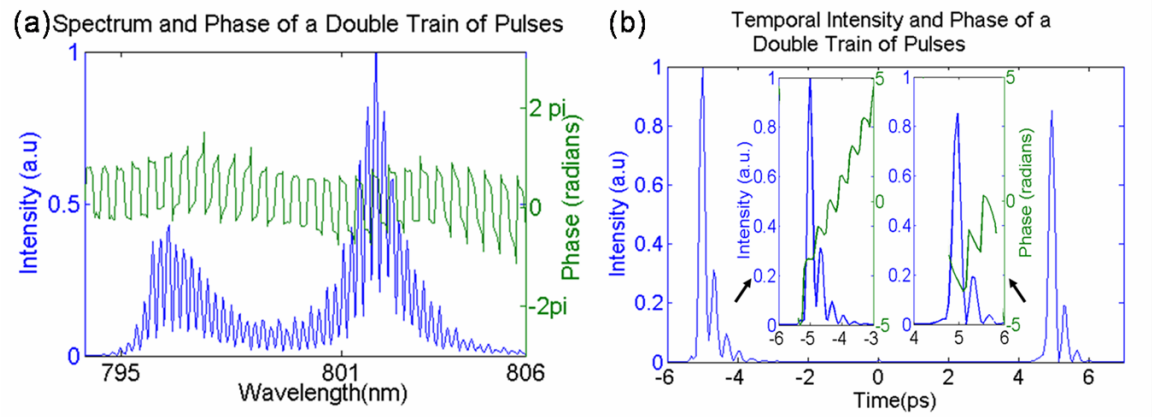

Figure 2.7: SEA TADPOLE double train of pulses measurement

Although we routinely monitor our pulses' intensity and phase using a Swamp Optics GRENOUILLE to confirm their approximately flat phase, in these experiments the key quantity was only the spectral phase difference between the unknown and reference pulses, which was the phase introduced by the SF11 glass in the first experiment, the phase due to the double-pulse behavior in the second experiment, and the phase of the double train of pulses in the last experiment. To measure the phase of an arbitrary unknown pulse, it is, of course, necessary to use FROG to characterize the reference pulse.

In all of our measurements, we retrieved the unknown pulse spectra from the same interference term used to obtain the spectral phase (the last term in equation 2.1). Noting that the amplitude of this term is proportional to the geometric mean of the

reference and unknown spectra, we simply squared this amplitude and divided by the spectrum of the known reference pulse. This not only worked well, but, interestingly, it achieves a type of spectral super-resolution which we discuss in detail in the next chapter.

Consider that, with one arm of our SEA TADPOLE device blocked, it is a simple spectrometer. Using the device in this manner, we measured spectra of the various unknown pulses, shown as the blue curves in Fig. 2.8. Also shown in Fig. 2.8 (in green) are the spectra obtained from the above SEA TADPOLE algorithm from the interference pattern. Note the significantly higher spectral resolution in the SEA TADPOLE spectra.

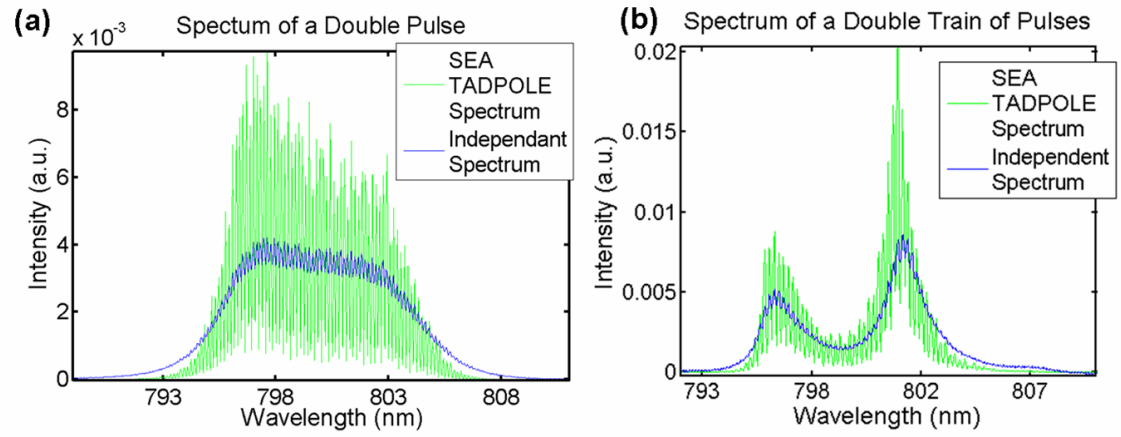

Figure 2.8: Measured and correct spectra

2.3.5 Measuring shaped pulses with SEA TADPOLE

Previous work has shown that SEA TADPOLE (without fibers) is useful for measuring shaped pulses [42]. To further demonstrate this, we used SEA TADPOLE to measure a phase-shaped pulse, which was shaped using a 256-element liquid crystal display (LCD) pulse shaper. For this experiment, we used an 85MHz repetition rate KM labs Ti:Sapphire oscillator, which had approximately 30nm of bandwidth. For the reference pulse, we used the unshaped oscillator pulse so that the phase difference that

we measured with SEA TADPOLE was the phase introduced by the pulse shaper. Figure 2.9 shows the results of this experiment. Figure 2.9b shows the phase that was applied by the shaper and the phase that was measured by SEA TAOPOLE and you can see that the two are in good agreement. Figure 2.9c shows the reconstructed spectrum ($S_{unk}(\omega)$) compared to the spectrometer measurement (taken by blocking the unknown beam just as we described in the previous section). You can see that $S_{unk}(\omega)$ is essentially a better resolved version the spectrometer spectrum as is often the case in SEA TAPDOLE (we discuss this in detail in the next chapter). Figure 2.9d shows the reconstructed temporal field and you can see that this pulse had a TBP of around 100. Figure 2.9a is the SEA TAPDOLE trace and it nicely illustrates that the curvature of the fringes is the phase difference between the interfering pulses.

2.4 Conclusions

We have introduced a new technique, which we call SEA TADPOLE, and we have shown that is can accurately determine the pulse intensity and phase, even for quite long pulses with fine spectral structure. SEA TADPOLE uses the spectrometer's full spectral resolution and even supersedes it. With our compact home-made spectrometer, it can measure pulses as long as 14 ps and it is experimentally much simpler and more convenient than other implementations of SI. It is also computationally simple and fast, making it ideal for real-time implementation. And it can measure quite complex pulses including shaped pulses as we have demonstrated. We believe that SEA TADPOLE will finally make SI practical and will be especially useful for measuring, confirming, and optimizing shaped pulses.

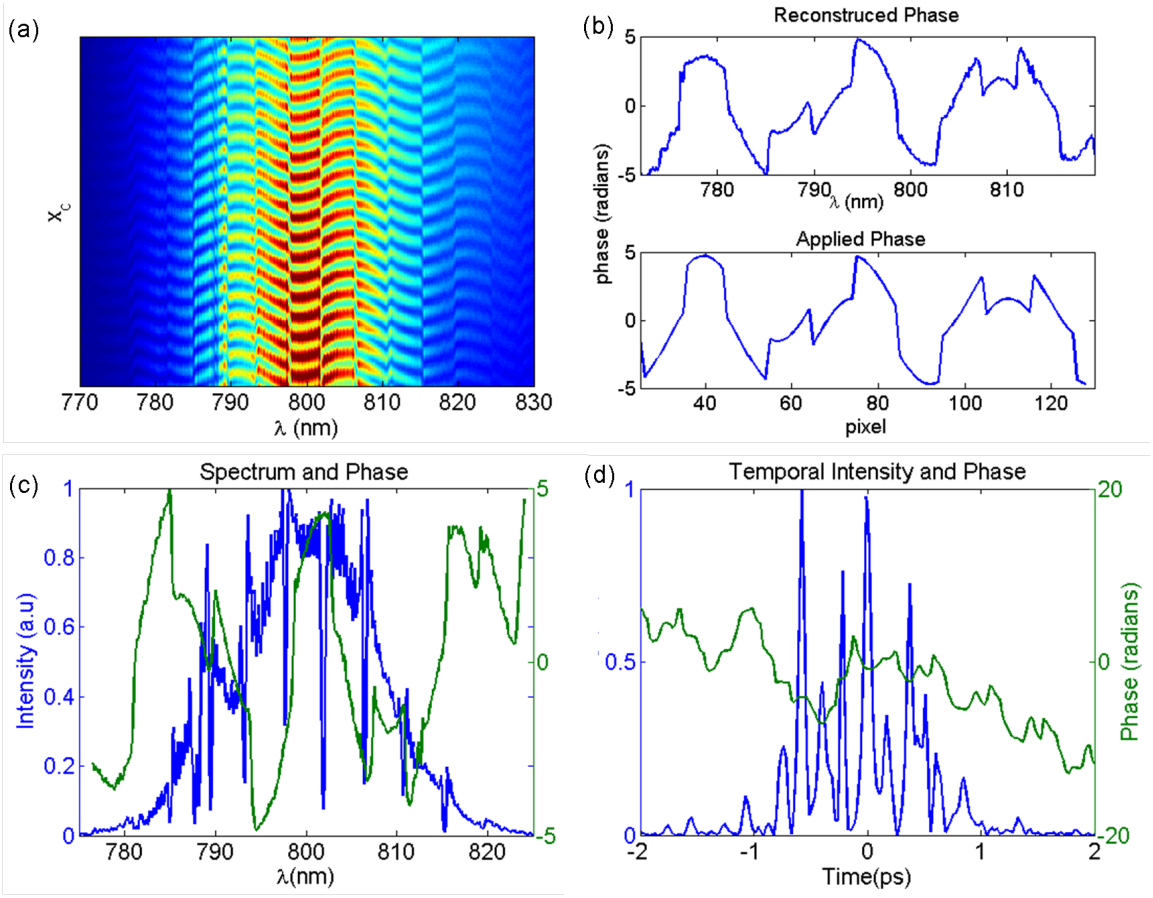

Figure 2.9: Measured shaped pulse

CHAPTER III

SPECTRAL SUPER RESOLUTION IN SEA TADPOLE

In section 2 (see figure 2.9) and in a previous publication [51], we showed that the spectrum retrieved from the SEA TADPOLE interferogram, which we call $S_{unk}(\omega)$, can be better resolved than the spectrum measured directly with the same spectrometer that is used in SEA TADPOLE. Experimentally we make this comparison by directly measuring the spectrum of the unknown pulse with the spectrometer, (which we call $S_{sp}(\omega)$) simply by blocking the SEA TADPOLE reference beam and $S_{unk}(\omega)$ is the amplitude squared of the interference term after dividing out the reference pulse's field (see 2.3.4). By retrieving the spectrum from the interferogram ($S_{unk}(\omega)$) we have been able to measure features in the pulse's spectrum that are $\sim$7 times smaller than what we could measure directly with the spectrometer [51]. Interferometry has also been used to improve spatial resolution in microscopy [56]. In spectral interferometry (see section 2.4) this spectral resolution improvement still occurs though is not noticeable due to the much larger resolution loss that happens because of the Fourier filtering that has to be done on the time axis [33, 46, 47].

In this section the spectral resolution of our measurements—or the smallest measurable spectral feature and the largest measurable temporal feature—is discussed in detail. It turns out that the spectral resolution of the field measured with SEA TADPOLE depends on the pulse's shape (intensity and phase). For some pulses, features that are significantly smaller than the spectrometer's resolution can be resolved, but there are some cases where a SEA TADPOLE measurement results in worse spectral resolution than the spectrometer.

3.1 Mathematical description of a spectrometer's response function

The resolution improvement achieved by interferometry can be explained by looking at one of the interference terms which is given by $E_{unk}(\omega)E^*_{ref}(\omega)$[1]. In this chapter we consider only the case where the reference pulse has a simple or smooth spectrum and the unknown pulse is very complicated, which is the case for measuring shaped pulses, and all of the examples that were shown in Chapter 2. Also for this discussion we will assume that the reference pulse has a flat spectral phase, and that it is at zero delay (although these are not strict requirements). Given these assumptions the interference term is approximately equal to $E_{unk}(\omega)$, or the complex electric field of the unknown pulse[2]. As a result, SEA TADPOLE directly measures the unknown electric field, while a spectrometer measures $|E_{unk}(\omega)|^2$ or the magnitude squared of the interference term.

To see why these two measurements can result in different spectra, we must include the effect of the spectrometer's instrument response function $H(\omega)$ whose width is the spectral resolution of the spectrometer $\delta\omega$. The finite resolution of the spectrometer effectively smears out, or averages together neighboring frequency components in the measured quantity, which can be modeled as a convolution [48, 57, 58]. Therefore, the spectrum measured with a spectrometer is given by $H(\omega) \otimes |E_{unk}(\omega)|^2$, and the spectrum retrieved from a SEA TADPOLE measurement is given by $H(\omega) \otimes E_{unk}(\omega)$.

If we view the effect of finite spectral resolution in the time domain, the convolution becomes a product where $h(t)$ is the fourier transform of $H(\omega)$ and $h(t)$ can be interpreted as a time window. As shown by equation 3.1, $S_{sp}(\omega)$ in the time domain

[1]The other interference term is given by the complex conjugate of this, but for this section, we will use the interference term given by $E_{unk}(\omega)E^*_{ref}(\omega)$

[2]Note, that if $E_{unk}(\omega)$ is as smooth as the reference pulse, or if $E_{ref}(\omega)$ is as complicated as the unknown pulse, then this approximation is not true, and the resolution of SEA TADPOLE is similar to that of the spectrometer

becomes the autocorrelation of $E(t)$ times $h(t)$.

$$\begin{aligned} S_{sp}(\omega) &= S_{unk}(\omega) \otimes H(\omega) \\ \mathscr{F}(S_{sp}(\omega)) &= (E_{unk}(t) \otimes E^{*}_{unk}(t)) \times h(t) \end{aligned} \tag{3.1}$$

Also shown in equation 3.2, the SEA TADPOLE spectrum in the time domain is simply the product of $E(t)$ and $h(t)$.

$$\begin{aligned} S_{unk}(\omega) &= E_{unk}(\omega) \otimes H(\omega) \\ \mathscr{F}(S_{unk}(\omega)) &= E_{unk}(t) \times h(t) \end{aligned} \tag{3.2}$$

Therefore, when using SEA TADPOLE, the pulse duration of $E_{unk}(t)$ has to be less than the width of the time window $h(t)$ which we will refer to as ΔT. And for a spectrometer, the width of the pulse's temporal field autocorrelation has to be less than ΔT; Most of the time this will be a wider function than $E_{unk}(t)$ itself. Given the shape of the spectral response function, the relationship between the spectral resolution and the time window can be determined. For example, if the spectral response function is a Gaussian, then $\Delta T = \frac{2\lambda^2}{c\delta\lambda}$.

From Eqs. 3.1 and 3.2, it is immediately apparent, that if the amplitude of $E_{unk}(\omega)$ is a delta function (or just very thin), then $S_{unk}(\omega)$ will have a width equal to that of $H(\omega)$ and $S_{sp}(\omega)$ with have a width equal to $H^2(\omega)$. Therefore, if $H(\omega)$ is a Gaussian, $S_{sp}(\omega)$ will be become wider than $S_{unk}(\omega)$ by a factor of $\sqrt{2}$ as we will illustrate in the next section (see Fig. 3.3).

It is also interesting to note that the convolution operator has eigenfunctions which are given $\exp(i\omega\tau)$ or $\cos(i\omega\tau)$ which corresponds to a purely oscillatory function. Therefore if a pulse has a spectral electric field given by one of these eigenfunctions then the spectrometer's instrument response function will not change or smear the shape of measured field, regardless of its width in time! But this seemingly infinite resolution does come at cost which is a loss in intensity that increases as τ increases.

Of course in practice, we never encounter fields that are purely oscillatory. Though we do commonly use pulses that are very close to being purely oscillatory such as a Gaussian spectrum multiplied by $\cos(i\omega\tau)$, which, if viewed in the time domain, is a double pulse, or a Gaussian pulse followed by an identical replica of itself τ later (for sufficiently large values of τ). As long as the Gaussian spectrum is much wider than the oscillations due to the cosine, this function is approximately an eigenfunction of the convolution operator and therefore, it is almost unchanged by the convolution. And, if we measure the double pulse with a spectrometer, because we are not measuring the complex field it is not an eigenfunction and therefore $S_{sp}(\omega)$ is much more effected than $S_{unk}(\omega)$ is. In fact, the spectrometer may not see any oscillations in the spectrum, while SEA TADPOLE will retrieve them nearly perfectly. But this spectacular resolution comes with a cost and as the frequency of the oscillations increase, the field is attenuated and eventually noise becomes a problem, and at some point the interference term will be too weak to detect. This is illustrated in Fig. 3.1.

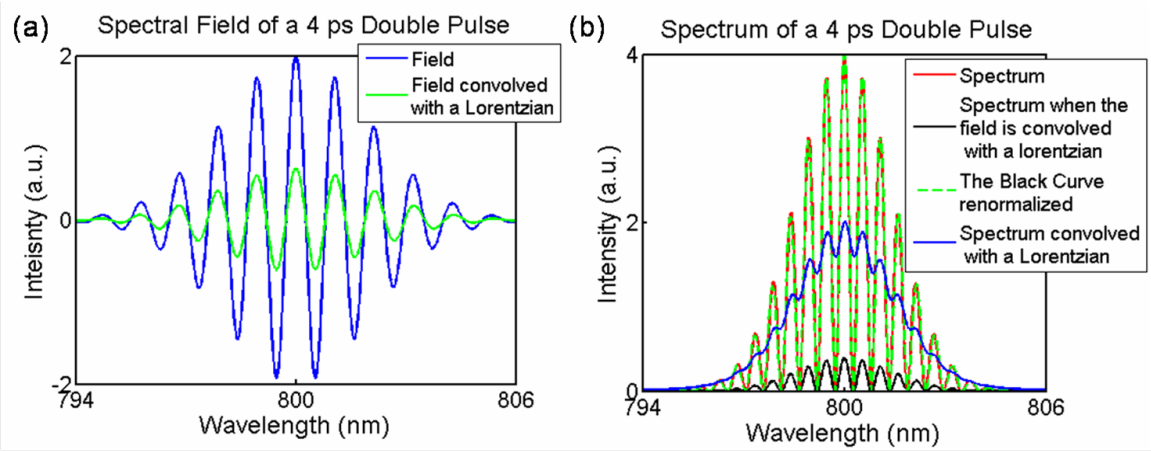

Figure 3.1: Approximate eigenfunctions of the convolution operator

Figure 3.1(a) shows $E_{unk}(\omega)$ for a double pulse before and after being numerically convolved with a spectral response function $H(\omega)$ which is Lorentzian with a width of 0.4nm for this example. The convolution does not noticeably change the shape of the field, it only attenuates it. Figure 3.1(b) shows the real spectrum (no convolution) in

red, the spectrometer spectrum $S_{sp}(\omega)$ in blue, $S_{unk}(\omega)$ in black and then also in green after being renormalized. You can see that $S_{unk}(\omega)$ is essentially unchanged in shape and only attenuated by the convolution while $S_{sp}(\omega)$ is badly smeared. In section 2.3.4 we experimentally demonstrate resolution enhancements such as this. In general we expect the improvement in spectral resolution offered by SEA TADPOLE to vary with the shape of the pulse involved and be somewhere between $\sqrt{2}$ (A very thin Gaussian spectrum) and a factor of $\sim$7 as we have observed for oscillatory spectral fields [51].

An important difference between $S_{unk}(\omega)$ and $S_{sp}(\omega)$ is that the spectral phase can have no effect on $S_{sp}(\omega)$ (because spectrometers measure only the spectrum and not the phase), but for $S_{unk}(\omega)$ this is not true. Because SEA TADPOLE resolves the complex field, (or the convolution acts on the complex field), to make a SEA TADPOLE measurement the spectral resolution of the spectrometer must be smaller than the smallest feature in the pulse's spectral amplitude and also its spectral phase (or equivalently, just its complex field). And because the convolution acts on the unknown pulse's complex field, it can mix together the spectrum and phase if the features in either one are too small. When the spectral phase has features that are too small to be resolved by the spectrometer, then its spectrum cannot be accurately measured using the interferometer (nor can its phase), but a spectrometer could still measure this pulse's spectrum. Therefore, as long as the pulse's complexity comes from its spectrum rather than its phase, or from both, $S_{unk}(\omega)$ will essentially always be better resolved than $S_{sp}(\omega)$.

3.2 Simulations to test SEA TADPOLE's spectral resolution

Because the difference between $S_{unk}(\omega)$ and $S_{sp}(\omega)$ is pulse dependent, this is best illustrated using examples. Figure 3.2 shows a simulation of how $S_{unk}(\omega)$ compares to $S_{sp}(\omega)$ and the ideal spectrum for 6 different pulse shapes. In Fig. 3.2, the white line

shows the actual spectrum, $S_{unk}(\omega)$ is shown in gray, and $S_{sp}(\omega)$ is shown in black. In this simulation, we used a Gaussian spectral response function with a width of 0.3 nm and all of the spectra are normalized to have an area of 1.

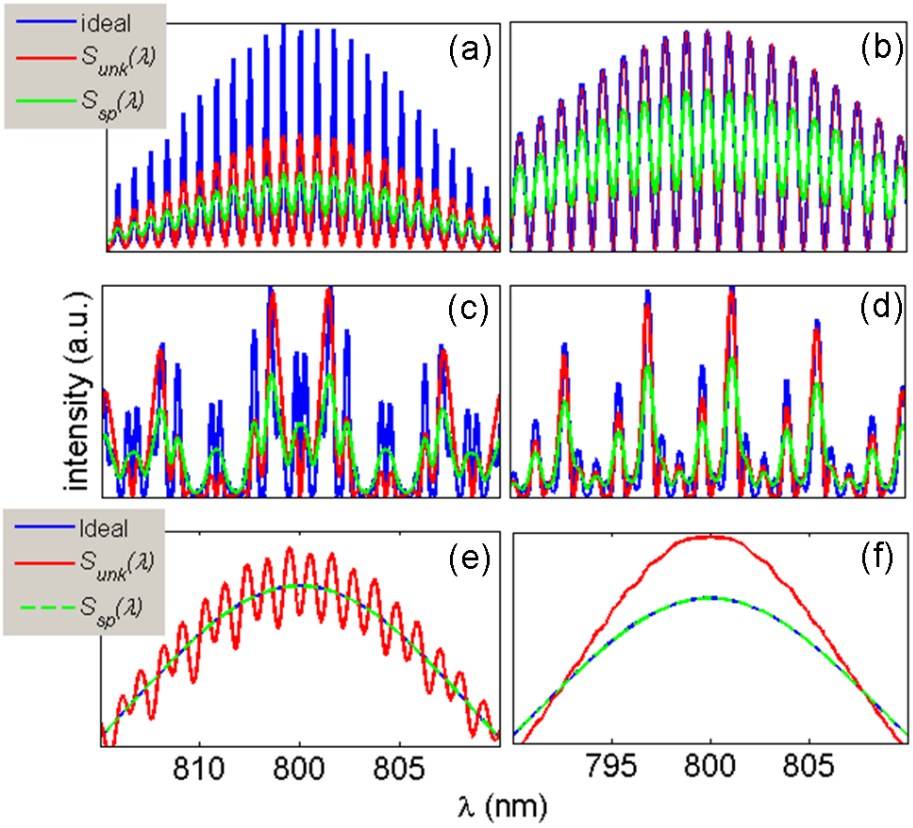

Figure 3.2: Examples of the $S_{unk}(\omega)$ compared to $S_{sp}(\omega)$

In Fig. 3.2, which was generated using a double pulse as unknown field (such as that generated by a Michelson interferometer), $S_{unk}(\omega)$ is identical to the real spectrum even though the duration of the double pulse is 50% of the width of $h(t)$. As discussed above this is because double pulses are approximately the eigenfunctions of the convolution operator as long as the individual pulses are much shorter that their spacing which was the case for this simulation. This can also be understood in the time domain, because the double pulse is approximately two delta functions with one at τ and the other at $-\tau$ and therefore when the $E(t)$ gets multiplied by $h(t)$ this

just attenuates each of the peaks and does not change the shape of the pulses.

Figures 3.2a, 3.2c, and 3.2d show the more typical improvement that we see with SEA TADPOLE and while $S_{unk}(\omega)$ is not identical to the real spectrum, it is noticeably closer to this than $S_{sp}(\omega)$ is. Figure 3.2a is a train of pulses such as that produced by a Fabry-Pérot etalon, Fig. 3.2c is a sum of 3 double pulses with different delays, and Fig. 3.2d is the same as c except that the double pulses are shorter.

Figures 3.2e and 3.2f show two examples in which $S_{sp}(\omega)$ is identical to the real spectrum and $S_{unk}(\omega)$ is distorted. These are pulses with Gaussian spectra and a sinusoidal spectral phase (Fig. 3.2e) and a huge amount of chirp (Fig. 3.2f). So these pulses have simple spectra (that are very easy to resolve with a spectrometer), but complex spectral phases that make their pulse durations very long in time (80% of $h(t)$ for Fig 3.2e and 140% for Fig. 3.2f). Therefore $S_{unk}(\omega)$ is distorted, while a spectrometer can perfectly measure these spectra. While we are accustomed to seeing smeared features in the spectrum when a spectrometer lacks sufficient resolution to make the measurement, when SEA TADPOLE lacks resolution to resolve a pulse because it is too long compared to h(t) due to its spectral phase, the distortions look quite different.

The numerical factor for the resolution difference in $S_{sp}(\omega)$ and $S_{unk}(\omega)$ depends on the exact shape of the pulse. For a Gaussian spectrum, squaring it decreases the rms width by $\sqrt{2}$, which is the resolution improvement for SEA TADPOLE in this case (as long as the spectral phase is relatively small). Figure 3.3 shows the result of a simulation that illustrates the difference in the $S_{sp}(\omega)$ and $S_{unk}(\omega)$ for a spectrum that is a very thin Gaussian centered at 800nm with an rms bandwidth of 0.1nm. In Fig. 3.3 you can see that, while $S_{unk}(\omega)$ is affected by the convolution, it is closer to the actual spectrum than $S_{sp}(\omega)$ In this example, the rms width of $S_{unk}(\omega)$ is 0.12 nm and, for $S_{sp}(\omega)$, this is 0.16 nm, which is a difference of about $\sqrt{2}$ as expected.

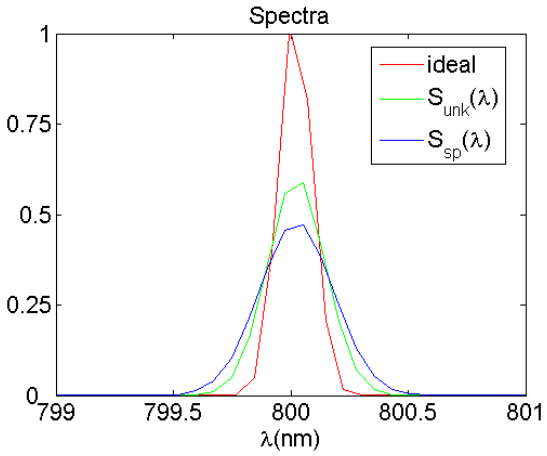

Figure 3.3: Example of the $S_{unk}(\omega)$ compared to $S_{sp}(\omega)$

3.3 Experimentally testing SEA TADPOLE's spectral resolution

Additionally we can do some experimental tests of the spectral resolution in SEA TADPOLE. First we experimentally measured the temporal response function of the spectrometer that we were using. We did this by observing the fringe visibility of the spectrum (the spectrum as measured with the spectrometer or $S_{sp}(\omega)$) produced by an etalon as we increased the spacing between the two reflectors (reflectivity = 57%), which is similar to the approach used in the following references [48, 59, 60]. This method is illustrated by the measurements shown in the Fig. 3.4. The etalon spacing is largest for the top spectrum and it is smallest for the bottom spectrum. And due to the the spectrometer's finite resolution the fringe visibility decreases as the etalon spacing increases (or as the fringes become smaller).

Quantitatively the change in visibility is most easily determined by Fourier transforming the spectrum to the time domain and looking at the relative height of a side band compared to the central peak as illustrated by the right image in 3.4. By measuring this relative height (which is attenuated due to the temporal response function) at different etalon spacings we can read off the temporal response function

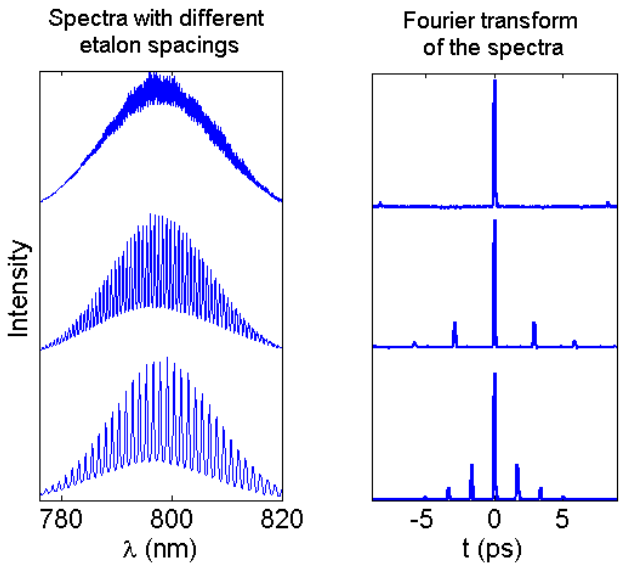

Figure 3.4: Illustration of how $h(\omega)$ was measured

of the spectrometer and this result is shown in Fig. 3.5. The left side of Fig. 3.5

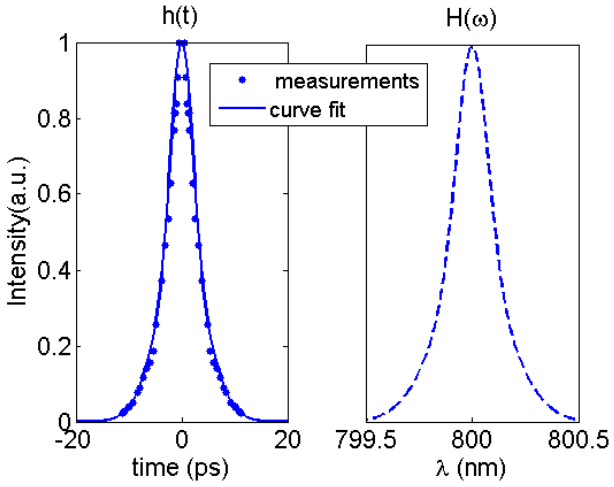

Figure 3.5: Measured temporal and spectral response functions

shows the measured temporal response function (dots) and a curve fit to the data (solid line) and the rms width of $h(t)$ was 3.9 ps (FWHM of 6.2 ps). Because we know that $H(\omega)$ is a real function, we know that $h(t)$ is symmetric and therefore we only measured one side of the temporal response function and assumed that it was

symmetric at t = 0[3]. The right plot in Fig. 3.5 shows the spectral response function which was obtained by Fourier transforming $h(t)$, and this curve has an rms width of 0.14 nm and this spectrometer had a spectral range of about 80nm. Therefore, if this spectrometer is used in SEA TADPOLE (assuming a relatively simple spectral phase) to measure $S_{unk}(\omega)$, the smallest feature in $E_{unk}(\omega)$ has to be greater than 0.14 nm, and if the spectrum $S_{sp}(\omega)$ is measured directly with this spectrometer, the same restriction applies to $|E_{unk}(\omega)|^2$, or the spectrum of the unknown pulse. Knowing the temporal response function is useful for determining precisely how well pulses can be measured using a given spectrometer in SEA TADPOLE. Additionally the experimentally determined $H(\omega)$ could be deconvolved from the reconstructed unknown field in order to further improve its resolution. In all of our measurements we have had sufficient spectral resolution in all, so that devonvolution, and the noise that this would introduce, could be avoided.

Fig. 3.6 shows a typical experimental example of how $S_{unk}(\omega)$ differs from $S_{sp}(\omega)$ using the spectrometer that was characterized above and an unknown pulse comprising a train of pulses produced by an etalon. The left plot in Fig. 3.6 shows $S_{sp}(\omega)$ and $S_{unk}(\omega)$ and when comparing the two spectra we can see, that $S_{unk}(\omega)$ is a better resolved version of $S_{sp}(\omega)$. To verify that $S_{unk}(\omega)$ is more accurate than $S_{sp}(\omega)$, we combined each of these spectra with the spectral phase that we retrieved from the SEA TADPOLE trace, and Fourier transformed this to the time domain which is shown on the right side of Fig. 3.6. Because we used an etalon with two identical 57% reflectors, the height of the second two peaks in the temporal intensity should be 0.33 and 0.11 respectively, so clearly the result from SEA TADPOLE is the more accurate one.

[3]If we did not use the spectrometer at the design wavelength, there would be off axis aberrations present in the spectrometer that would make $H(\omega)$ asymmetric, and then both size of $h(t)$ would need to be measured

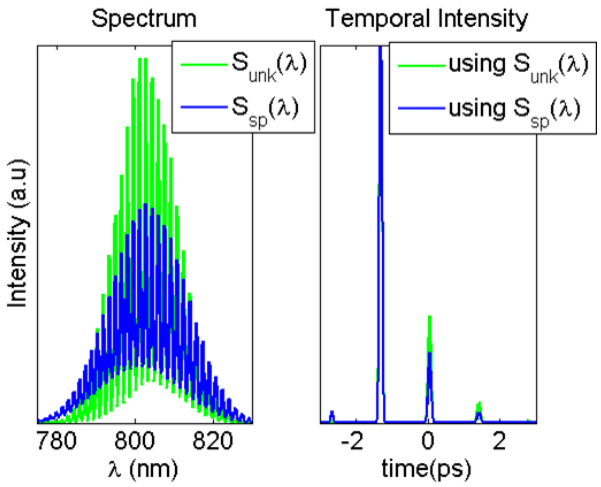

Figure 3.6: Comparison of spectrometer and SEA TADPOLE measurement of a train of pulses

Figure 2.9 (which was discussed in Chapter 2), shows another experimental example of how $S_{sp}(\omega)$ compares $S_{unk}(\omega)$ which represents a significant improvement and illustrates the typical improvement that we expect when measuring shaped pulses.

3.4 Other issues and comments

Another issue that must be considered when retrieving the spectrum from the SEA TADPOLE interferogram is the delay, or the location of $E_{ref}(\omega)$ underneath the temporal window. For example, if the unknown pulse is delayed with respect to the reference pulse (which is at zero delay) by τ then the interference term becomes $E_{unk}(t-\tau) \times h(t)$ and is no longer centered underneath the temporal response function. Because the temporal window is flattest at its center (because it is typically a Gaussian, or some similar function as we showed in the previous section), the unknown field will be more distorted by the temporal response function if it does not have a mean of zero, because it will then be multiplied by a steeper part of $h(t)$. To illustrate this, we performed a simulation, making SEA TADPOLE traces for a double pulse at several different delays. The temporal intensity and spectra retrieved from these three traces is shown in Fig. 3.7. The bottom plot in Fig. 3.7 shows $h(t)$

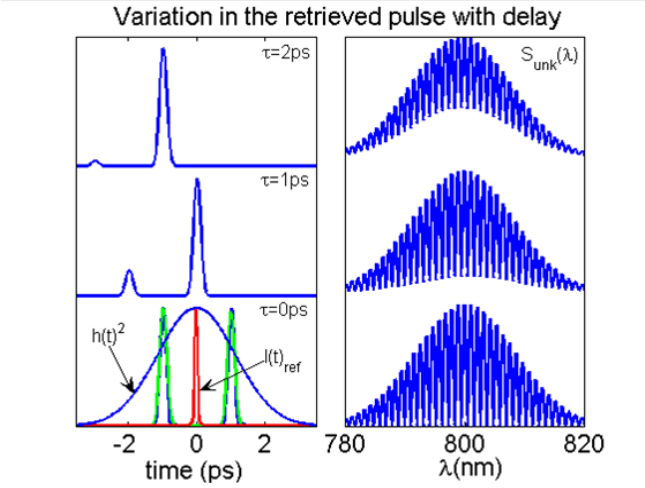

Figure 3.7: Variation of $I_{unk}(t)$ and $S_{unk}(\lambda)$ with delay

(blue), the ideal temporal intensity (green) and the reconstructed temporal intensity (blue) which is $h(t)$. The higher plots show the reconstructed temporal intensity when the unknown pulse was delayed by 1 ps (middle) and 2 ps (upper) and these results are much more distorted than the result of the zero delay interferogram. It is evident that it is important to measure the SEA TADPOLE interferogram at zero delay in order to minimize the damage done by the spectrometer's response function, and this becomes more important as the duration of the unknown pulse becomes close to the width of the temporal window.

As explained in section 2.2, spectral interferometry requires that the there be a delay between the $E_{unk}(\omega)$ and $E_{ref}(\omega)$, As illustrated here, this means that the retrieved field from the spectral interferogram, which already suffers a spectral resolution loss due to Fourier filtering on the time axis, will be further distorted due to the required delay.

CHAPTER IV

MEASURING POLARIZATION SHAPED PULSES

4.1 Introduction

In Chapter 2 we discussed SEA TADPOLE which is a method for measuring the temporal electric field of ultrashort pulses with high spectral resolution, which is easy to use, and can measure complex pulses at video rates. This method is ideal for measuring the shaped pulses that are commonly used in quantum coherent control experiments, as we demonstrated in chapter 2.

But molecules and atoms are three dimensional, so to really control them with laser fields, both the fields' temporal shape and polarization must be appropriately shaped. Therefore, there has been a trend in quantum control towards using not just pulse shaping, but polarization pulse shaping [6–10]. Control of the pulse's polarization to generate time dependent polarization states has also been used for generating attosecond pulses using high harmonic generation [61]. Polarization shaping typically involves using a polarizing beam splitter to separate the S and P polarization components and then two pulse shapers are used so that $E_x(\omega)$ and $E_y(\omega)$ can be given arbitrary and different temporal pulse shapes, and then the two polarizations are recombined with a second beam splitter [9]. Recently a more compact design for a polarization pulse shaper that uses only one SLM was introduced [62].

To optimize and build experiments that use polarization pulse shaping, it is important to be able to measure the complete polarization state of the pulse, or $E_x(\omega)$ and $E_y(\omega)$, including their relative spectral phase $(\varphi_x(\omega) - \varphi_y(\omega))$ must be determined. Quantum control experiments use optimization or feed-back loops that result

in complicated pulses with durations as long as 10ps. Therefore, to characterize polarization shaped pulses, a measurement technique that is fast, high spectral resolution, and that can measure the complete polarization state of such a pulse is needed.

In the past a technique known as POLLIWOG or Polarization Labeled Interference versus Wavelength of Only a Glint has been the primary method for measuring polarization shaped pulses [12]. POLLIWOG involves using a polarization beam splitter to break the pulse into its S and P components and then $E(\omega)$ for each of these components is measured using Spectral Interferometry (see section 2.2). POLLIWOG has all of the advantages of SI, such as being very sensitive and fast. But it also has the disadvantages, such as the strict alignment requirements and a loss of spectral resolution results when reconstructing $E(\omega)$ from the interferogram making it difficult to measure the more complex shaped pulses (see section 2.2.3). Another difficulty with POLLIWOG is that the interferometer has to be very stable, so that the measured relative phase of $E_x(\omega)$ and $E_y(\omega)$ is the real relative phase.[1]

Another, similar approach for measuring polarization shaped pulses called TURTLE, or Tomographic Ultrafast Retrieval of Transverse E-Fields, uses several FROG measurements to determine the pulse's complete polarization state [63]. Because a single FROG measurement is not sensitive to the absolute phase or the delay, simply measuring $E_y(\omega)$ and $E_x(\omega)$ will not tell you the relative absolute phase or the relative delay between the two components of the pulse. TURTLE is designed to regain this information by making FROG measurements of the S and P components as in POLLIWOG, but also a FROG measurement is made of $E_x(\omega) + E_y(\omega)$ by putting a quarter wave plate (QWP) in the beam before the FROG device. These three FROG measurements are then used to reconstruct the complete polarization state including the relative delay and absolute phase. The disadvantage to using FROG is that it is

[1] If there is a drift in the interferometer between the time that $E_y(\omega)$ and $E_x(\omega)$ are measured, the measured relative phase will contain this contribution due to the drift which will be indistinguishable from the pulse's relative phase.

a multi-shot technique and its retrieval can be quite slow (and even slower if three measurement have to be made) for complex shaped pulses [32].

In this chapter we use SEA TADPOLE to measure the complete polarization state of complex pulses, so that even complex polarization shaped pulses can be measured, quickly and using a simple device. Because the phase drift that happens in SEA TADPOLE (see Appendix B) causes us to loose the relative absolute phase (also just called the relative phase), we use an approach similar to that used in TURTLE to regain this information without having to stabilize the interferometer.

4.2 Method

To measure the complete polarization state of a pulse we need to measure $E_y(\omega)$ and $E_x(\omega)$ and the relative spectral phase including the relative absolute spectral phase which we will call φ_{rel}. The most straightforward way to make this measurement would be to make two SEA TADPOLE measurements, one of $E_y(\omega)$, and of $E_x(\omega)$. This measurement would yield the relative spectral intensity of the E_x and E_y and the all terms in the relative spectral phase, except for relative absolute phase[2]. This is because of the phase drift in SEA TADPOLE that we discuss in Appendix B which is due to a random change in the path length of the two arms of the interferometer that most likely happens because of small temperature fluctuations that change the index of refraction of the fibers. In Appendix B a measurement of the typical drift that we experience is shown which illustrates that the drift's effect on the higher order spectral phase terms is negligible. However, the average drift in the absolute phase is around 1.8 radians over one minute (though it varies equally as much over a few seconds). This is a large error for a quantity that only varies between 0 and 2π, and therefore, we effectively loose the absolute spectral phase difference information (or φ_{rel}). So, if we only make the two measurements described above, we will measure

[2]Just to clarify, by higher order relative spectral phase terms, we mean for example, the difference in the chirp, cubic phase and etc, between the x and y components of the field.

the following fields

$$E_x(\omega) = \sqrt{S_x(\omega)} \exp\left(\varphi_x(\omega) \times \varphi_{rel} \times \varphi_{rand}\right) \tag{4.1}$$

$$E_y(\omega) = \sqrt{S_y(\omega)} \exp\left(\varphi_y(\omega) \times \varphi_{rand}\right) \tag{4.2}$$

$$\varphi_{rel} = \varphi_{0x} - \varphi_{0y} \tag{4.3}$$

where φ_{rand} is a random number between 0 and 2π which we use to model the effect of the interferoemter's drift, and φ_{0x} and φ_{0y} refers the the absolute phases. Note that in the above equations, we have subtracted the the absolute phase $E_y(\omega)$ from both fields so that the relative phase appears only in $E_x(\omega)$.

In order to be able to measure the relative absolute phase we could take special care to stabilize the interferometer, for example, by building an acrylic box around it as was done in the following reference [64]. It also might be possible to very quickly make the two measurements before the drift effects the phase. But, considering that a path length change in the interferometer as small as $\frac{\lambda}{4}$ results in a phase drift of $\frac{\pi}{2}$, it is very difficult to make the interferometer stable enough. Therefore, we would like to use a technique that can measure the relative phase without having to stabilize the interferometer.

The trick is to not only make SEA TADPOLE measurements of $E_y(\omega)$ and $E_x(\omega)$, but to also measure $E_y(\omega) + E_x(\omega)$ for example, by putting a wave plate before SEA TADPOLE's entrance fiber to rotate the polarization of the unknown pulse [63, 65]. In this third measurement, which we will refer to as $E_{xy}(\omega)$, we get the following,

$$E_{xy}(\omega) = \left[\sqrt{S_x(\omega)} \exp\left(\varphi_x(\omega) \times \varphi_{rel}\right) + \sqrt{S_y(\omega)} \exp\left(\varphi_y(\omega)\right)\right] \times \exp\left(\varphi_{rand}\right). \tag{4.4}$$

You can see from Eq. 4.4 that in the measured field $E_{xy}(\omega)$, φ_{rel} is not lost by the random phase due to the drift because these two phase terms do not appear together as they do when only one of the field's components is measured as shown in Eq. 4.1. Therefore, with SEA TADPOLE measurements of $E_x(\omega)$, $E_y(\omega)$ and $E_{xy}(\omega)$, and an

appropriate algorithm to extract φ_{rel} from these three measurements, we should be able to reconstruct a pulse's complete polarization state.

4.2.1 Reconstructing the complete polarization state from the measured SEA TADPOLE traces

To reconstruct the polarization state from the three fields discussed above, we first measure the SEA TADPOLE traces for these three fields and then reconstruct $E_x(\omega)$, $E_y(\omega)$ and $E_{xy}(\omega)$ from the interferograms in the usual way (which is described in section 2.3.2). At this point we have everything except for the relative absolute phase. To determine this we use a minimization routine in order make the spectrum of $E_x(\omega) + E_y(\omega)$ the same as $I_{xy}(\omega)$ by adding a constant to the spectral phase of $E_x(\omega)$ as described by the equations below where we have factored the absolute phases out of the fields.

$$I_{x+y}(\omega) = \left|E_x(\omega) + E_y(\omega)\right|^2 = \left|E_x(\omega) + E_y(\omega)\exp\left(i\varphi_{rand} + i\epsilon\right)\right|^2 \tag{4.5}$$

$$I_{xy}(\omega) = \left|E_{xy}(\omega)\right|^2 = \left|E_x(\omega)\exp\left(i\varphi_{rel}\right) + E_y(\omega)\right|^2 \tag{4.6}$$

Equation 4.6, shows that taking the magnitude of the measured field $E_{xy}(\omega)$ completely removes the random phase.

Our goal is to pick a value of ϵ that will make $\varphi_{rand} + \epsilon = \varphi_{rel}$. When we have done this, the two spectra $I_{x+y}(\omega)$ and $I_{xy}(\omega)$ will be the same. The Example shown in the figures below illustrates this process. In this example, which is a simulation, we used a simple Gaussian pulse with a delay between E_x and E_y and with a relative phase of 45°. To do the minimization we plot the rms difference between $I_{x+y}(\omega)$ and $I_{xy}(\omega)$ summed over all frequencies as a function of ϵ and look for the minimum in this curve. As you can see in Fig. 4.1a, for this example, the minimum occurs at 45° as it should. Figure 4.1b, compares the spectra before and after the minimization and once we have picked the value of ϵ that makes the absolute relative phase correct, these two spectra overlap well.

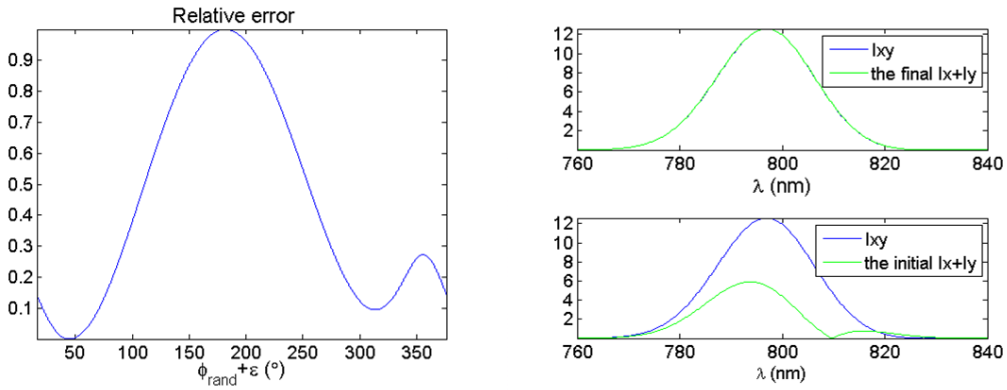

(a) RMS error (b) Spectra

Figure 4.1: Reconstructing φ_{rel} from measured SEA TADPOLE spectra

4.2.2 Experimental setup for measuring polarization shaped pulses with SEA TADPOLE

To measure the complete polarization state with SEA TADPOLE, we need to make three measurements of the field, one of $E_x(\omega)$, one of $E_y(\omega)$ and one of $E_{xy}(\omega)$. These three cuts, or projections of the field, can be obtained by placing a polarizer and a half wave plate in the unknown arm of SEA TADPOLE, just before the pulse's entrance fiber to SEA TADPOLE as illustrated in 4.2. All other parts of SEA TADPOLE's

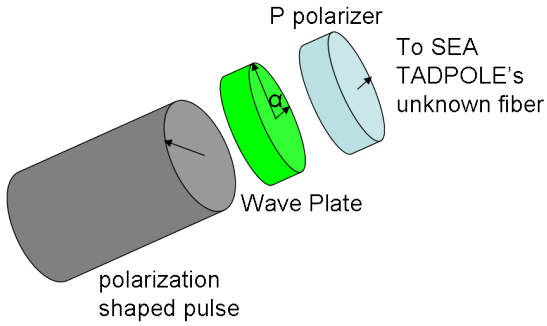

Figure 4.2: Schematic for measuring different field components to measure the polarization state with SEA TADPOLE

experimental setup remain unchanged and a schematic of SEA TADPOLE can be found in Fig. 2.3b. Using the analyzer illustrated in Fig. 4.2, the projection of the

unknown pulse's polarization state that we measure is given by,

$$E_{unk}(\omega,\alpha) = \Big[i\sin^2(\alpha) - i\cos^2(\alpha)\Big]E_x(\omega) - \Big[2i\sin(\alpha)\cos(\alpha)\Big]E_y(\omega) \tag{4.7}$$

where α is the angle between the beam's axis and the fast axis of the wave plate. Therefore, we can can simply rotate the waveplate to take the three measurements that we need, and at $\alpha = 0$, we will measure $iE_x(\omega)$, at $\alpha = \pi/8$ we will measure $i\frac{\sqrt{2}}{2}(E_x(\omega) + E_y(\omega))$ and at $\alpha = \pi/4$ we measure $iE_y(\omega)$.

There are several advantages to using this method to measure the fields. A motorized stage can be used to precisely and quickly rotate the wave plate to the needed angles. Also, having a polarizer after the half wave plate, assures that polarization of the unknown beam will be the same for all three measurements so that SEA TADPOLE's sensitivity to polarization (due primarily to the diffraction grating's polarization dependent efficiency) will not affect our results. With this approach we do not have to worry about mechanically stabilizing the interferometer and a we have the advantage of SEA TADPOLE's high spectral resolution, quick inversion algorithm and simple experimental setup (as opposed to using POLLIWOG or spectral interferometry).

4.2.3 Ambiguities

It is important to identify and understand any ambiguities that can occur in the absolute phase retrieval described above. For example, how can we be sure that the error plot will only have one minimum or that our algorithm will return only one answer? It turns out that there are some cases when we retrieve two answers and this can be easily understood by expanding out Eq. 4.6 as shown below.

$$I_{xy}(\omega) = S_x(\omega) + S_y(\omega) + \Big|E_x(\omega)E_y(\omega)\Big| \times \cos\left(\varphi_x(\omega) - \varphi_y(\omega) + \varphi_{rel}\right) \tag{4.8}$$

The relative absolute phase is contained only in our measured field E_{xy}, whose intensity is shown above. You can see by expanding out this quantity, that the relative

absolute phase information is contained inside of a cosine which can cause problems, because cosines are even functions and they are insensitive to the sign of their arguments. As illustrated in Fig. 4.3a, if the spectral phases of E_x and E_y are the same, then the error curve will have two minima and is will not be possible to determine the sign of the φ_{rel}. But, as long as $E_x(\omega)$ and $E_y(\omega)$ have different spectral phases,

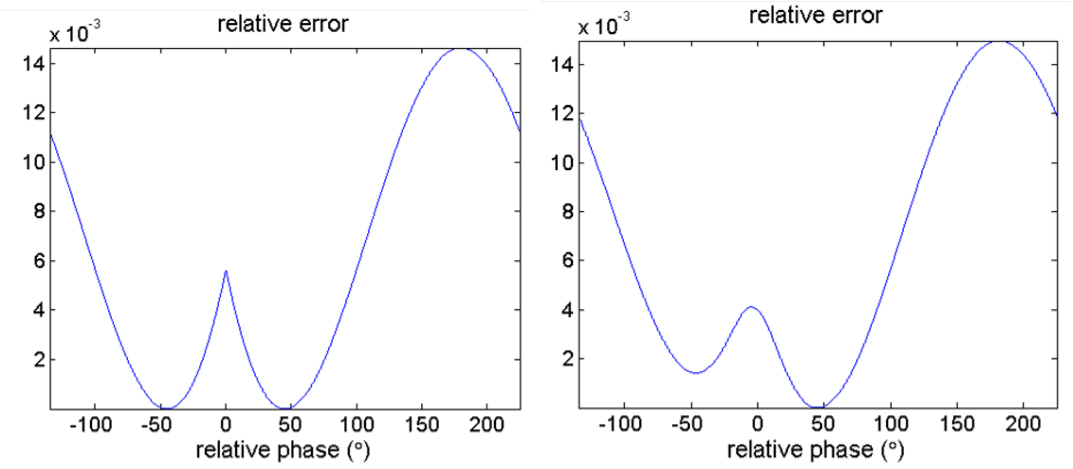

(a) $\varphi_x(\omega) - \varphi_y(\omega) = 0$ (b) $\varphi_x(\omega) - \varphi_y(\omega) = \omega\tau$ where τ is the delay

Figure 4.3: Error plots for determining the relative phase absolute phase have two minima when the spectral phases of $E_x(\omega)$ and $E_y(\omega)$ are the same.

as shown in Fig. 4.3b, there is no ambiguity because the sign of φ_{rel} will change the value of the argument of the cosine. And if this is the case, $I_{xy}(\omega)$ will be different for φ_{rel} and minus $-\varphi_{rel}$ and the error curve will have a minimum at only one of these values.

Fortunately, this should not be a problem for us, because we want to measure polarization shaped pulses which will be complicated so that $E_x(\omega)$ and $E_y(\omega)$ will not have the same spectral phases most of the time. But, if it is necessary to remove this ambiguity, it can be done my making a fourth SEA TADPOLE measurement of the field $E_x(\omega) + iE_y(\omega)$ by replacing the half wave plate with a quarter wave plate. This measurement will yield an intensity like that shown in Eq. 4.8, except that there is a sine in place of the cosine. This intensity alone would still not allow us

to always determine the sign of φ_{rel}. But using this intensity in the minimization along with $I_{xy}(\omega)$ yields the absolute phase including its sign even when two field components have the same spectral phases. This is because the sine and the cosine can be combined together to make an exponential which does not have a sign ambiguity (it is neither a purely even or a purely odd function).

If we were to encounter a case where the spectra of the $E_x(\omega)$ and $E_y(\omega)$ do not overlap, then the field $E_{xy}(\omega)$ would not contain the absolute relative phase information because the cross term shown in Eq. 4.8 would be 0, and the minimization would not yield φ_{rel}. We can still retrieve φ_{rel} using $E_{xy}(t)$, by taking a Fourier transform of the field, and doing the minimization with the temporal intensities using $E_x(t)$ and $E_y(t)$ as long as the fields overlap in time. If the x and y components of the field neither overlap in time nor frequency, then the retrieval algorithm descried here will not work, though we do not expect to encounter this case very often. In most cases, considering that spectral domain shaping is usually used, the spectra of $E_y(\omega)$ and $E_x(\omega)$ will overlap, though the temporal fields may not overlap and this is why we have chosen to do the minimization with the spectral intensities.

4.3 Simulations

Before experimentally testing this method, we tested it out with simulations. In the first simulation, we used a Gaussain pulse for E_x and E_y where both had flat spectral phases, but with E_x ahead in time. We added 5% Gaussian noise to this simulation and $\varphi_{rel} = 45°$. The results are shown in Fig. 4.4. Figure 4.4a, shows the error curve and there is a minimum at 45.9° which is close to the expected value. Figure 4.4b compares $I_{x+y}(\omega)$ and $I_{xy}(\omega)$ before and after the minimization and they overlap well once we have found the correct value for φ_{rel} giving an error of 0.002% at this value. Figure 4.4b shows the retrieved temporal intensities and the spectra compared to the correct answers, and you can see that the two are in good agreement except for a

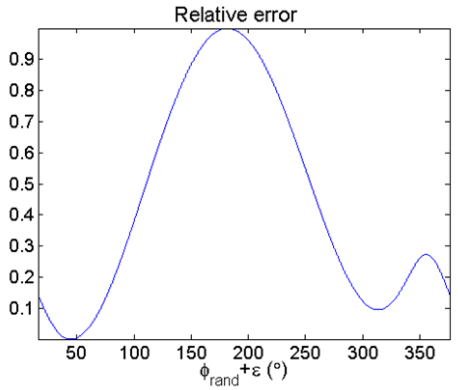

(a) error curve

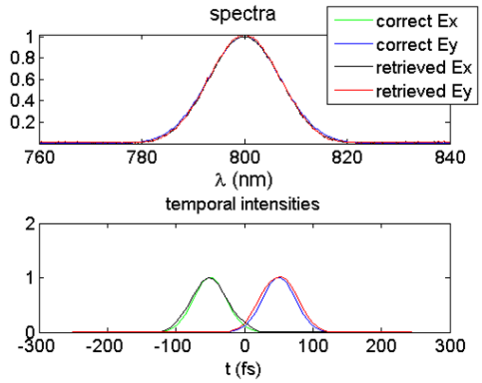

(b) Spectra and temporal intensities

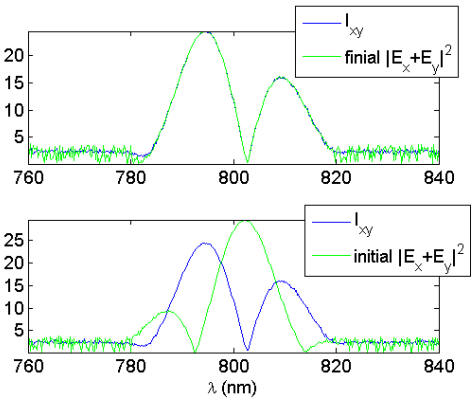

(c) Spectra before and after the minimization

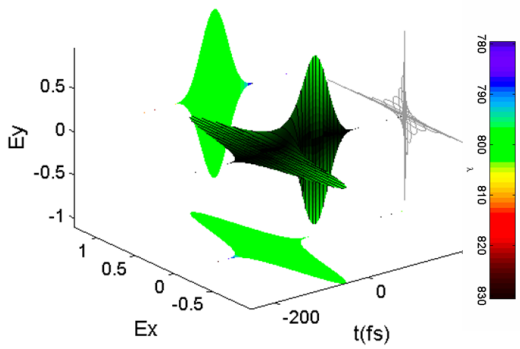

(d) Reconstructed polarization state

Figure 4.4: Simulation of reconstructing the polarization state of a Gaussian pulse with $\varphi_{rel} = 45°$ and a delay between E_x and E_y.

small discrepancy due to the noise that we added.

The final figure shown at the bottom right is a plot of the reconstructed polarization state plotted in the usual way [6]. To make this plot we Fourier transform the retrieved fields to the time domain and at every value of t, we plot the polarization ellipse for that value of t, which is given by the equations below

$$E_x(t) = |E_x(t)| \cos(\phi_{rel} + \phi_x(t) + l) \tag{4.9}$$

$$E_y(t) = |E_y(t)| \cos(\phi_y(t) + l) \tag{4.10}$$

where l is an angle between 0 and 2π that is use to parameterize the ellipses. Ellipses are commonly used to plot polarization states and a few examples of these for monochromatic light are shown in Appendix C. In this plot, at points in time where the pulses do not overlap, the pulse has a linear polarization state and when they do overlap, the polarization angle is given by $\varphi_{rel} + \varphi_x(t) - \varphi_y(t)$, so it varies with time due to the time dependence of pulse's phase. The gray lines in this figure are the projection of the polarization ellipses at every time onto this plane. Also in Fig. 4.4d the color represents the instantaneous center frequency which we calculate by averaging together the colors of the x and y components (calculated from ($\omega_0 = \frac{d\phi(t)}{dt}$)) of the field weighted by their intensities at a given point in time and space. and both components of the pulse are green at every point in time for this pulse because both E_x and E_y have flat spectral phases. This figure also shows the projections of the pulse onto the x and the y axes so that you can see both the shape and the color of the x and y components of the pulse as a function of time.

In the next simulation we used a very similar pulse, but this time both E_x and E_y were chirped (by the same amounts) and φ_{rel} was equal to 90°. These results are shown in Fig. 4.5. Again, Figs. 4.5a through 4.5c illustrate that our retrieval worked well and the minimum occurred at 89.7° which is close to the expected value. I_{xy} overlaps well with I_{x+y} at this value for φ_{rel} and the error is 0.12%. Also, the

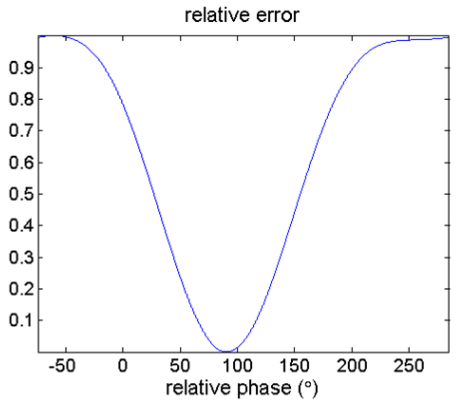

(a) error curve

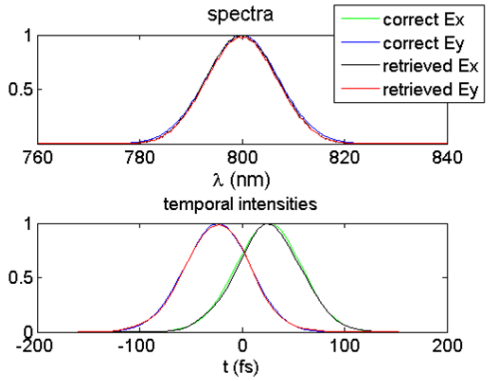

(b) Spectra and temporal intensities

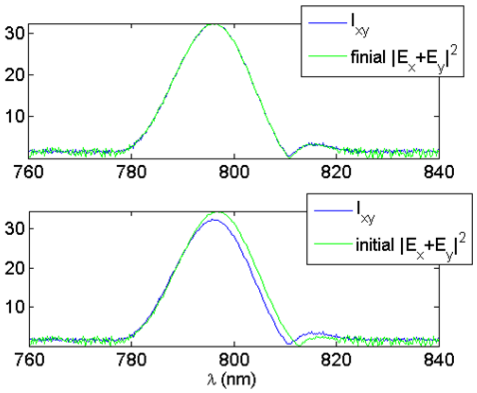

(c) Spectra before and after the minimization

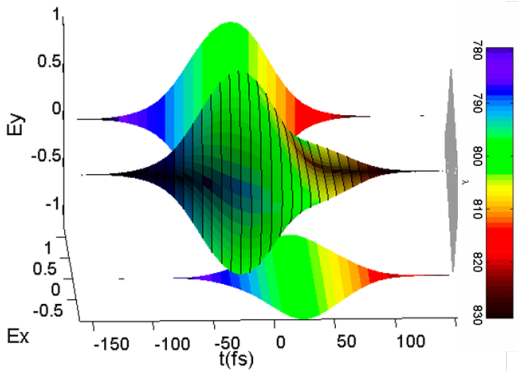

(d) Reconstructed polarization state

Figure 4.5: Simulation of reconstructing the polarization state of a Gaussian pulse with $\varphi_{rel} = 90°$ and a delay between E_x and E_y, and chirp.

retrieved spectra and temporal intensities agree with one another. Figure 4.5a shows the reconstructed polarization ellipses at every time, and for this pulse, due to the temporal chirp, you can see that the pulse's color changes with both time and direction. As in the previous example, the pulse starts off with a vertical polarization and then while, E_x and E_y overlap, the pulse is elliptically, and the circularly polarized and then elliptically again. And then for later times when $E_y = 0$ the pulse is horizontally polarized. When the pulses overlap in time you can see that the color is like that of E_x along the x axis and like that of E_y along the y axis.

To make sure that our algorithm would work for more complex pulses such as those that are produced by a polarization pulse shaper, we tested our method out on a complex pulse that is shown in Fig. 4.6b (correct E_x and E_y). This pulse consisted of a linear 45° pulse at t=-500fs, followed by a right circular pulse at t=-250fs, then a left circular pulse at t=250fs and then finally another 45° pulse at t=500fs. The outer pulses had an intensity of 36% of the inner pulses, and there was no chirp on any of the pulses. The results of the retrieval are shown in Fig. 4.6 and you can see that they are in good agreement with the expected answer. The color changes seen in Fig. 4.6d close to where the field changes sign are due to difficulties unwrapping the temporal phase which we use to calculate the instantenous center frequency in the plots. Because the higher order spectral phases of E_x and E_y were the same, you can see that there are two minima in the error curve or there is a overall minus sign ambiguity in our determination of the relative phase. This means that we could retrieve this pulse train to be composed of a 180° pulse then a left circular then a right circular followed by a 180° pulse, as opposed to the correct answer. Note that this sign of the relative phase cannot be seen using our plotting style for the polarization state.

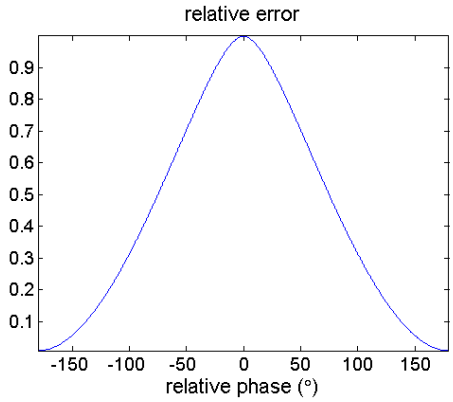

(a) error curve

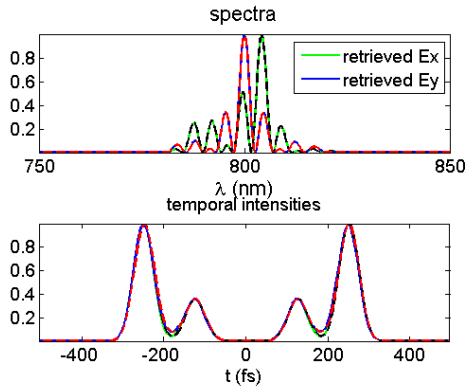

(b) Spectra and temporal intensities

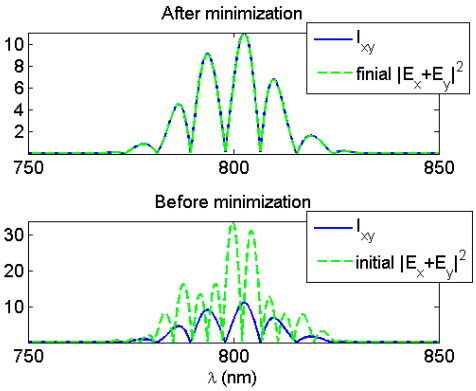

(c) Spectra before and after the minimization

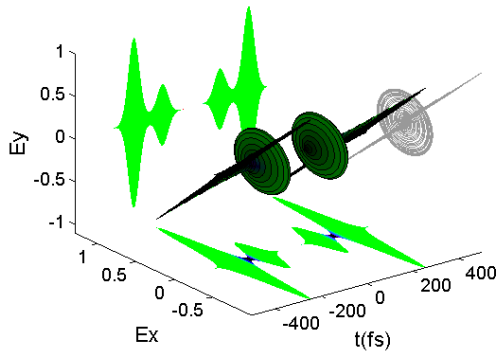

(d) Reconstructed polarization state

Figure 4.6: Simulation of reconstructing the polarization state of complex pulse

4.4 Measurements

To further test our algorithm, we produced and measured a few pulses with known absolute relative phases to verify that we could retrieve the correct answer. For this experiment, we used an 85MHz repetition rate KM labs Ti:Sapphire oscillator, which had approximately 30nm of bandwidth. For the reference pulse, we the used oscillator pulse by putting a beam splitter before the polarization state was generated. In all of the measurements shown in this section, the x and y components of the field had the same spectral phases and therefore we were only able to determine the absolute value of φ_{rel} and not its sign. Though in the data in this section it many appear that one of the two minima in the error curves is slightly less than the other, this is only due to the noise that was present in the measurements.

In the first experimental test we rotated the polarization state of the Gaussian pulse from the oscillator using a quarter wave plate at the appropriate angle to make the light circularly polarized. Then we sent this beam through the analyzer shown in Fig. 4.2, and then to SEA TADPOLE so that the three projections needed for the reconstruction were measured. The results of this measurements are shown in Fig. 4.7. Figure 4.7a shows the error curve which has two minima near $\pm 94^\circ$ which is close to the value that we expect(For circularly polarized light,$\varphi_{rel} = 90^\circ$). The polarizations ellipses shown in 4.7d, are circles at every point in time which we also expect, because every frequency component of the pulse should have the same polarization (or very close to it) because we used a zeroth order quarter wave plate. Also, the relative amplitude of E_x and E_y should be 1, as it is, and the error in the reconstruction (the minimum value in Fig. 4.7c) was 0.06%.

In the next measurement, we used the same setup described above, but we rotated the polarizer to make an elliptical polarization with $\varphi_{rel} = 54^\circ$ and a relative amplitude of 3.5. Figure 4.8 shows these results. From Fig. 4.8a we found that the minimum happened at a value of $\varphi_{rel} \pm 52.7^\circ$) and that the relative amplitude was

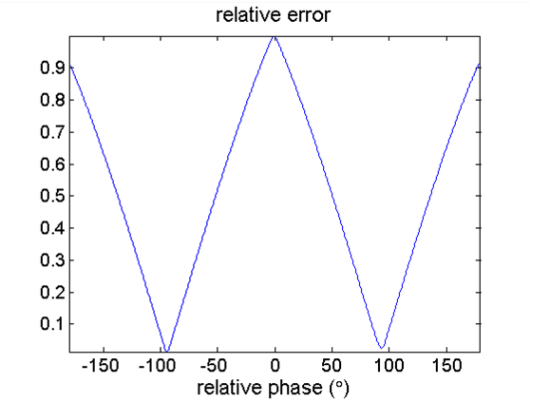

(a) error curve

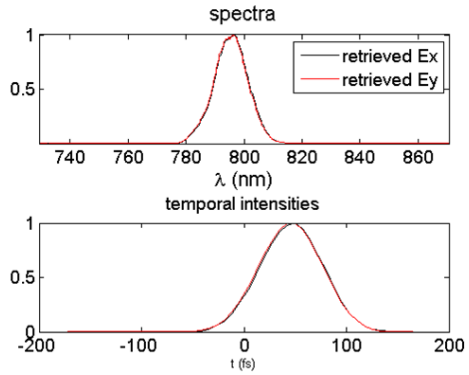

(b) Spectra and temporal intensities

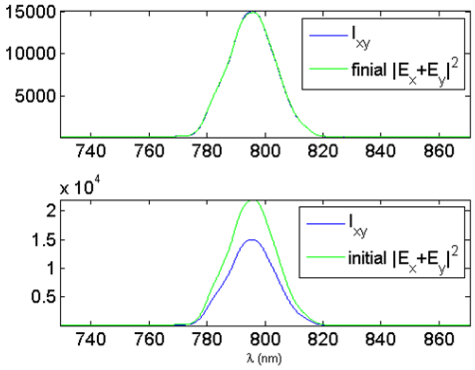

(c) Spectra before and after the minimization

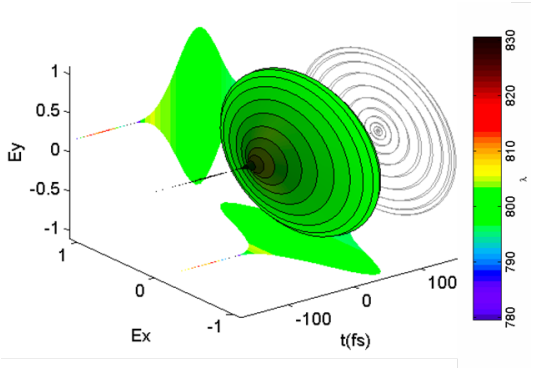

(d) Reconstructed polarization state

Figure 4.7: Experimental reconstruction of an circularly polarized pulse.

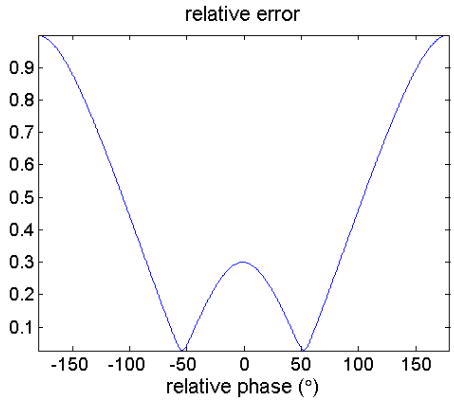

(a) error curve

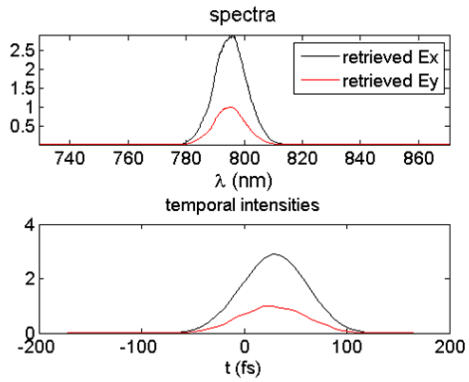

(b) Spectra and temporal intensities

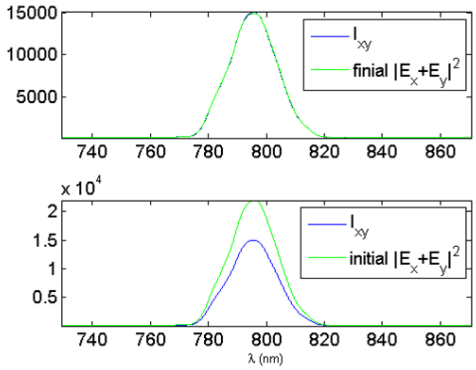

(c) Spectra before and after the minimization

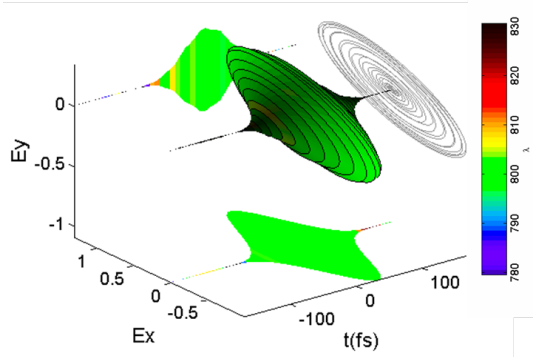

(d) Reconstructed polarization state

Figure 4.8: Experimental reconstruction of an elliptically polarized pulse.

2.9, which are both close the answer that we expected. Figure 4.8d shows the retrieved polarization state and at every time you can see that this it is the same ellipse with the color varying a little in time, due to a small difference in chirp between the reference and unknown pulses.

In the final experimental test we used a slightly more complicated pulse though the spectral phase of the x and y components were still the same (meaning that we still could only determine the magnitude of φ_{rel}). To make this pulse we passed the beam through a 256-element liquid crystal display (LCD) pulse shaper and we applied a voltage to it to make the pulse into a double pulse (a sinusoidal phase). Then we propagated the double pulse through a polarizer to ensure that it was still P polarized and then a quarter wave plate to make it a circularly polarized double pulse and then we sent this pulse to the polarization analyzer and then to SEA TADPOLE to measure the three cuts needed to reconstruct its polarization state. Again, we used the pulse directly out of the oscillator as the reference pulse.

Figure 4.9 shows the results of this measurement. The minimum of our error curve is close to the expected value (it was at $\pm 91°$) and the relative amplitude is close to 1.2 which is close to the expected value of 1. Even though the spectra in the minimization were more complicated this time, you can see from Fig. 4.9c that they overlap well after the minimization. The polarization state is plotted in Fig. 4.9d, and it shows one circularly polarized pulse followed by an very similar circularly polarized pulse, just as we expect considering the wave plate and the phase mask on the pulse shaper that were used.

In these measurements, we found it advantageous to also measure $i\frac{\sqrt{2}}{2}(E_x(\omega) - E_y(\omega))$ by making a SEA TADPOLE measurement with the half wave plate's angle at 67.5°. Though this did not give us any additional information, or remove the sign ambiguity, it did allow us to simultaneously minimize the difference between this measured spectrum and $|(E_{unkx}(\omega) - E_{yunk}(\omega))|^2$ as well as the minimization that was

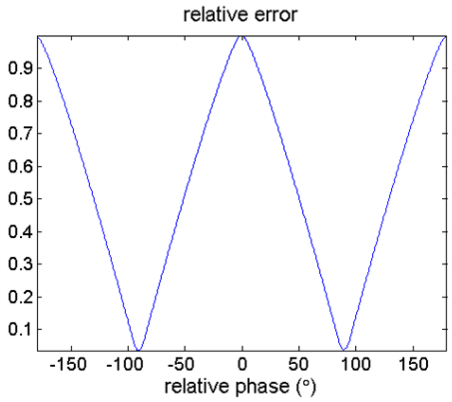

(a) error curve

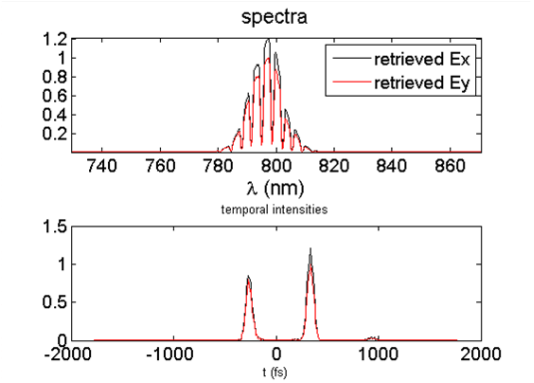

(b) Spectra and temporal intensities

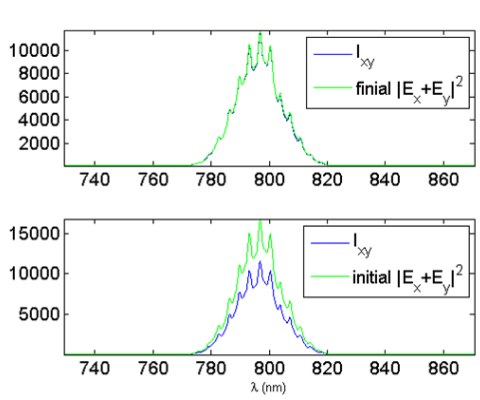

(c) Spectra before and after the minimization

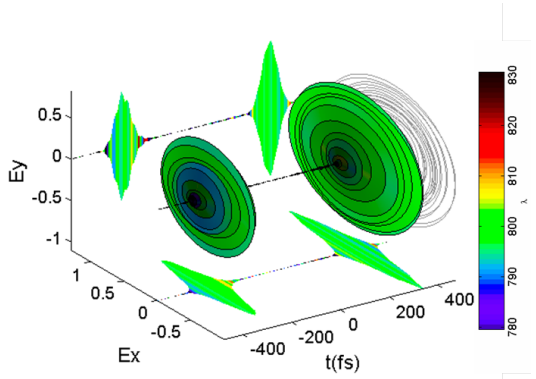

(d) Reconstructed polarization state

Figure 4.9: Experimental reconstruction of a circularly polarized double pulse.

discussed in above, which makes the algorithm less sensitive to noise and intensity fluctuations. This was convenient to do because we had the half wave plate mounted to a rotation stage, though in general only the 3 measurements discussed in section 4.2.1 are necessary.

4.5 Conclusions and future outlook

In this chapter an extension of SEA TADPOLE for measuring polarization shaped pulses was discussed. In this method we add an analyzer to SEA TADPOLE so that interferograms of the fields $E_x(\omega)$, $E_y(\omega)$, and $E_x(\omega) + E_y(\omega)$ can be measured and retrieved. These three interferograms combined with a simple minimization procedure can then be used to determine the intensity and the phase of the x and y components of the field including the relative spectral phase and the relative absolute phase of the pulse. We verified that this procedure works well by doing several simulations that included some very complicated pulses and three examples of these were shown. We tested this method out in the lab on a few simple pulses and achieved accurate results for the relative absolute phase. In the future we would like to test SEA TADPOLE out on real polarization shaped pulses in which the higher order spectral phases of the two field components are different (and then we can retrieve the sign of the relative absolute phase), though from our simulations and preliminary experimental tests we have no reason to believe that this should not work. SEA TADPOLE, can measure polarization shaped pulses, with a simple experimental setup, with high spectral resolution, and relatively quickly (in 3 shots) and therefore it should be a very useful device for measuring and optimizing polarization shaped pulses.

CHAPTER V

MEASURING THE SPATIOTEMPORAL ELECTRIC FIELD OF FOCUSING ULTRASHORT PULSES

5.1 Introduction and background

In this chapter a version of SEA TADPOLE for measuring the spatiotemporal electric field $E(x, y, z, t)$ of ultrashort pulses at and around the focus is described which we call scanning SEA TADPOLE [55]. Before describing and demonstrating scanning SEA TADPOLE, we show how focusing pulses with common lens aberrations can be modeled so that we will have a way to test our initial measurements to verify that scanning SEA TADPOLE works. Also we will use this model to show how common lens aberrations distort ultrashort pulses.

5.1.1 Motivation

In nearly all applications of ultrashort pulses such as plasma generation, coherent control of chemical reactions, micro machining, nonlinear microscopy or high harmonic generation, the pulse is used at a focus. In general, the highest possible intensity is desired, and this is achieved when the pulse is undistorted in both space and time, so that it has a transform limited time duration and a diffraction limited focused spot size. Unfortunately, lenses and lens systems suffer from a wide variety of aberrations, and theoretical studies have shown that very complex spatiotemporal distortions can occur at a focus, due to, for example, spherical and chromatic aberrations [15, 66–68].

If no aberrations or material dispersion were present (the ideal case), then the spatiotemporal field of the pulse at the focus would look like that shown in the figure below. Figure 5.1 shows snap shots of the pulse at different z's or positions around

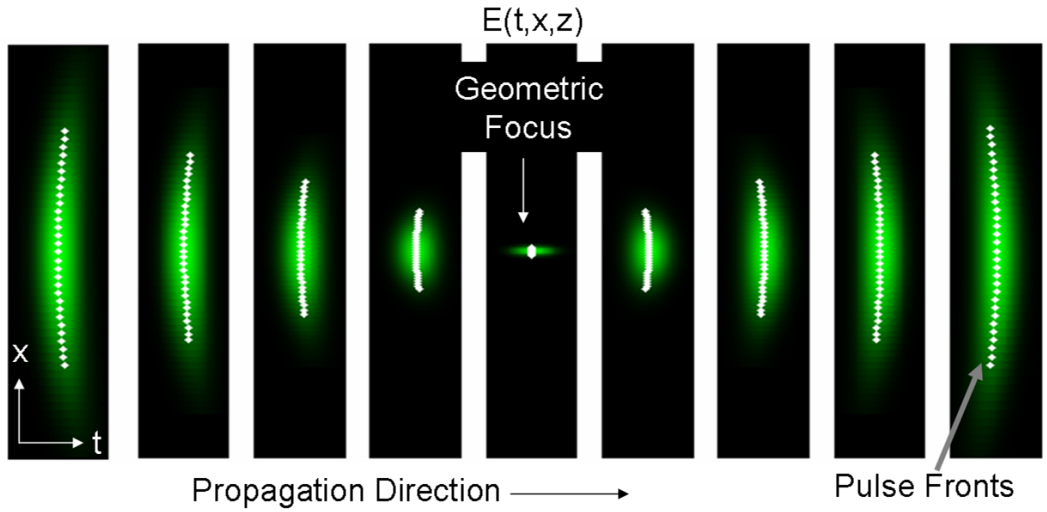

Figure 5.1: Simulation of the focus of an ideal lens

the focus. In these plots, the color represents the instantaneous center frequency of the pulse which is the same everywhere in space and time because no distortions are present. The white dots show the pulse front or the arrival time of the pulse at every x. When no distortions are present the pulse fronts are flat at the focus and symmetric about the focus. The next figure shows a simulation of the focus of a lens with chromatic aberration and a little spherical aberration. This figure illustrates

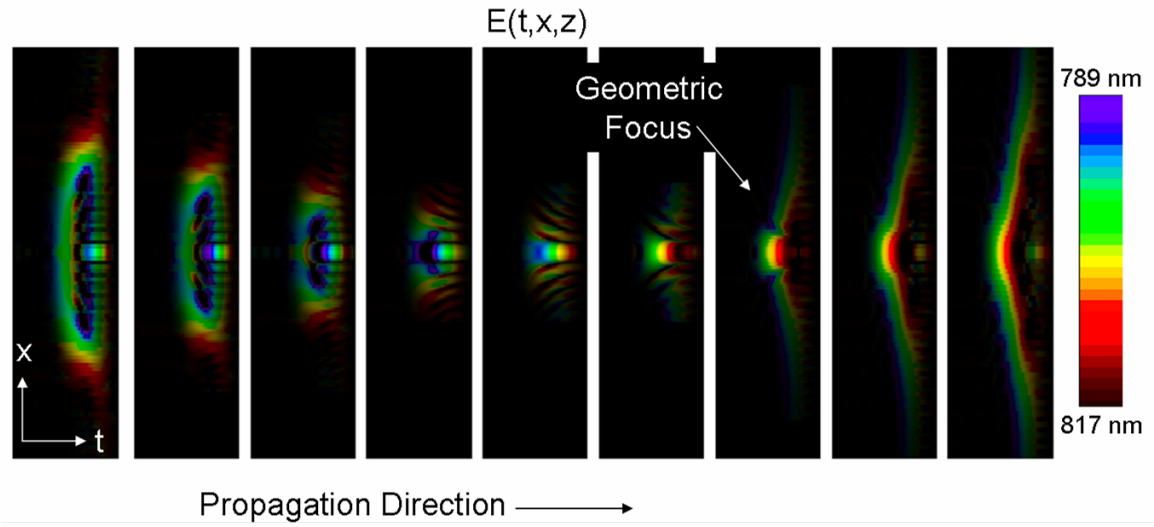

Figure 5.2: Simulation of the focus of a lens with a lot of chromatic aberrations

that the pulse can take on a very complex spatiotemporal shape when common lens aberrations are present. Due to chromatic aberration the pulse's color varies in x, t and z which makes the local bandwidth smaller, or it make the pulse duration longer. Also due to the aberrations, the spot size is far from being a nice round point as need for most applications. Even with perfect material dispersion compensation (such as the example shown in Fig. 5.2), when chromatic aberrations are present, the pulse can still be distorted and far from transform and diffraction limited at the focus.

The simulations shown in Fig. 5.2 illustrate that measuring only $E(t)$ or $E(\omega)$ averaged over x and y of a focused pulse is far from sufficient. For the same reason, measuring only $E(x, y)$ averaged over ω, or just making a spatial measurement is also far from sufficient. To characterize a focused ultrashort pulse, a spatiotemporal measurement of $E(x, y, z, t)$ must be made so that all of the cross terms (the $x - t$ couplings) are measured.

To further complicate the problem, in addition to focusing, pulse shaping is often used in applications such as nonlinear microscopy and coherent control and these pulses have complex temporal shapes [10, 39]. And even without pulse shaping, diffraction effects at the lens' aperture and lens aberrations alone can make the pulse as long as picosecond [15]. Therefore, a technique that can measure the spatiotemporal electric field with high spatial and spectral resolution is need for characterizing focused pulses. Additionally, this technique needs to be very sensitive (or linear-optical) to be able to measure $E(t)$ at values of x that are away from the center of beam which can be very weak.

Although techniques are available for measuring focused pulses in space or time separately, none of these can measure the spatiotemporal electric field. Autocorrelators are available for determining the rough pulse duration at the focus [69, 70] with no phase or spatial information. With some nonlinear-optical pulse measurement techniques, the lens in question can be used as the focusing lens in the pulse-measurement

device, so that the temporal electric field after the lens is the measured field [12, 71–73]. Unfortunately, all such measurements average over all spatial dimensions at the focus, so that no spatial information is obtained (there is one exception in which minimal, qualitative spatial information was obtained [74]). Linear interferometric techniques for measuring spatial and temporal information have been introduced, but these only measure collimated pulses [68, 75, 76]. Therefore, if a focused pulse is to be characterized using these techniques, it must first be recollimated and this is usually done with the same lens that was used to focus it. In this case, the electric field of the focused pulse can only be inferred indirectly from the measurement of the recollimated beam by assuming that the phase of the lens is half of the phase obtained by double-passing the lens (which is only true if the alignment is perfect).

In this chapter, a simple technique for directly measuring the complete spatiotemporal electric field at and near the focus of an ultrashort pulse is described. To our knowledge this is the first technique in which the spatiotemporal field, $E(x, y, z, t)$, is directly measured for a focusing pulse. From a typical measurement using our device, a movie can be made of the pulse focusing, showing its intensity and color vs. space and time. To make these measurements we use SEA TADPOLE, or Spatial Encoded Arrangement for Temporal Analysis by Dispersing a Pair of Light E-fields which was described in detail in chapters 2 and 3 and can be found in these references [50, 51, 55].

Because the entrance to SEA TADPOLE is an optical fiber, it naturally measures pulses with high spatial resolution, and, in particular, it can measure them at a focus.[1] If the fiber for sampling the unknown pulse has a mode size smaller than the smallest spatial structure of the focused spot size of the unknown pulse, then $E_{unk}(\omega)$ can

[1]The spatiotemporal field of collimated pulses can be measured as well as long as the there is enough power in the unknown field. The difficulty is that for collimated beams, they are usually as large as 0.5mm - 1cm and therefore not much light is coupled into the fiber which has a mode size around 5.6μm

be measured at one position (x, y, z) and then the fiber can be scanned in x, y, and z until $E_{unk}(\omega)$ has been measured at all spatial points at and near the focus, so that we have $E(x, y, z, \omega)$. Inverse-Fourier-transforming to the time domain yields $E(x, y, z, t)$. Doing this, it is possible to watch the pulse focusing, or measure it at many positions along the propagation direction before, after and at the focus. We refer to this technique as scanning SEA TADPOLE.

While scanning SEA TADPOLE bears some resemblance to the method of interferometric photon tunneling scanning microscopy (PTSM) there are some key differences between the two methods [45, 64, 77, 78]. Both methods involve sampling or spatially resolving the unknown field with an optical fiber (or an NSOM probe in the case of PTSM) and then interferometrically recombining it with a reference pulse for each position of the sampling fiber. While interferometric PSTM operates in the space and time domains scanning SEA TADPOLE operates in the space and frequency domains. Interferometric PSTM has primarily been used to measure propagating pulses in photonic structures while scanning SEA TADPOLE is intended for measuring focusing pulses. Also, interferometric PSTM requires scanning in 4 dimensions to measure $E(x, y, z, t)$ because scanning is required to measure $E(t)$ unlike SEA TADPOLE which only requires 3 scanning dimensions to make this measurement because $E(t)$ is measured in a single shot.

5.1.2 Numerically modeling focusing ultrashort pulses with low NA's

In order to test scanning SEA TADPOLE we measured $E(x, \omega)$ at several different z's (the propagation direction) at and around the focus. We also calculated the expected spatiotemporal fields given the experimental beam, pulse and lens parameters in order to make sure that our measurements were correct. Later in this chapter we will show these results and in this section we show how these simulations were done.

As we will explain later in section 6.3, scanning SEA TADPOLE (with fiber as

described in this chapter) is limited to measuring foci with numerical apertures less than 0.12[2]. Because of this restriction, we can model these foci using the Fresnel integral which is a small angle approximation of the Kirchhoff Integral (also called the Fresnel-Huygen's integral) and is therefore only valid up to numerical apertures of 0.4 [15, 79].[3] Here we will only consider the cylindrically symmetric aberrations chromatic and spherical aberrations, because these are the aberrations that most commonly distort ultrashort pulses. Off axis aberrations such as astigmatism or coma can usually be removed or greatly minimized just by properly aligning the lens.

Given the electric field $E(x_1, y_1, \omega, z = 0)$ at an initial plane $z = 0$, the Fresnel integral can be used to calculate $E(x, y, \omega, z)$, or the field after the light has propagated a distance z from the lens which is at $z = 0$. See Eq. 5.1.

$$E(x, y, \omega, z) \propto \int_{-\infty}^{\infty} dx_1 \int_{-\infty}^{\infty} dy_1 E(x_1, y_1, \omega, 0)\Theta(x_1, y_1, \omega) \exp\Big[-\frac{ik}{2z_2}[(x - x_1)^2 + (y - y_1)^2]\Big] \tag{5.1}$$

For our case, $E(x_1, y_1, \omega, z = 0)$ is the electric field of the pulse just before the lens, $\Theta(x_1, y_1, \omega)$ is the phase and amplitude introduced by the lens, and z is the propagation distance from the lens and the observation plane where the field is given by $E(x, y, \omega, z)$. This geometry is illustrated in Fig. 5.3. This version of the diffraction integral can be found in many references such as [79] and specifically for modeling focusing pulses in [66, 67, 81].

The intensity and phase introduced by the lens is given by,

$$\Theta(x_1, y_1, \omega) = P(x_1, y_1) \exp\Big[i\frac{k}{2f_0}(x_1^2 + y_1^2)\Big] \times \exp\Big[i\varphi(x_1, y_1, \omega)\Big] \tag{5.2}$$

where $P(x_1, y_1)$ is the aperture function of the lens (most likely just a circular aperture that can be bigger or smaller than the beam), and $\varphi(x_1, y_1, \omega)$ is the phase due to

[2]The numerical aperture or the NA of a focus is defined as the sine of the half divergence angle.

[3]Note that the Fresnel approximation is equivalent to a paraxial approximation, and therefore this integral is also referred to as the paraxial diffraction integral [80].

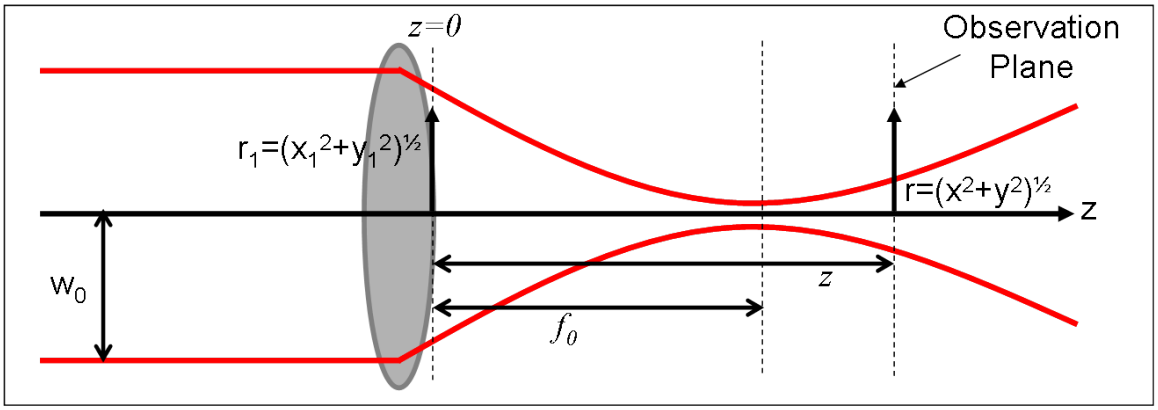

Figure 5.3: Schematic of the Fresnel integral for modeling a focusing pulse

aberrations and group delay dispersion of the lens (GDD). The other phase term is the quadratic spatial phase introduced by the lens and for an ideal lens this would be the only non-zero phase term. All of the subscript 0's indicate that the value is taken at the center frequency where f is the focal length of the lens which is a frequency dependent quantity.

In all of our measurements, we used lenses and beams with cylindrical symmetry and therefore it is convenient to write $E(x_1, y_1, \omega, z = 0)$ and $\varphi(x_1, y_1, \omega)$ as $E(r_1, \omega, z = 0)$ and $\varphi(r_1, \omega)$ where r_1 and θ are the radius and polar angle for the cylindrical coordinate system. As discussed above, in our experiments we should be able to minimize off-axis aberrations so that there will no θ dependence in Θ. After changing the integral to polar coordinates, and integrating out the θ dependence, Eq. 5.1 becomes

$$E(r, \omega, z) \propto exp\left[\frac{ikr^2}{2f_0}\right] \times \int_0^R dr_1 r_1 J_0(r_1 r k_0/f_0) E(r_1, \omega, 0) P(r_1) \exp\left[\varphi(r_1, \omega) - i\frac{kr_1^2}{2}(1/f_0 - 1/z)\right]. \tag{5.3}$$

In Eq. 5.3 J_0 is a Bessel function of the first kind of order 0 that comes from the integration over θ after changing from rectangular to cylindrical coordinates. Also, in the above equation we assumed that the lens had a finite aperture with a radius of R and therefore we have changed the integration limits because $P(r_1)$ will be zero for

$r_1 > R$. For the initial field $E(r_1, \omega, 0)$ we use a two-dimensional Gaussian with the spot size and the bandwidth of the beam/pulse that was used in the experiments. In our simulations, we use a flat spectral phase for the field before the lens, because this contribution to the spectral phase cancels out in our SEA TADPOLE measurements as we will explain further in section 5.2.[4]

The phase due to spherical and chromatic aberrations, and also the GDD (β) introduced by the center thickness of the lens is given by the following equation:

$$\varphi(r_1, \omega) = \exp\left[-ikAr_1^4 - i\beta(\omega - \omega_0)^2 - i(\omega - \omega_0)(\alpha r_1^2 + \gamma(\omega - \omega_0)r_1^2)\right]. \tag{5.4}$$

The first term in Eq. 5.4 is due to spherical aberrations. The coefficient A can easily be calculated using the formula show below which comes from [82].

$$A = \frac{n_0^2(n_0^2 - 4) + 2n_0 + 4}{8n_0(n_0 - 1)^2(n_0 + 2)f_0^3} \tag{5.5}$$

To model lenses that are not plano-convex a ray tracing program is needed to determine A and we use the program OSLO. The next terms are due to the radially varying group delay and radially varying group delay dispersion that result due to the lenses varying thickness with r_1. These terms are easily calculated by Taylor expanding the focal length which is given by $1/f = n(\omega)(1/R_1 - 1/R_2)$ where R_1 and R_2 are the radii of curvature of the first and second surfaces of the lens and $n(\omega)$ is the refractive index of the material that the lens is made of [67]. Formulas for these coefficients are given below.

$$\alpha = \frac{k_0}{2f_0(n_0 - 1)} \frac{dn}{dw}\Big|_{\omega=\omega_0} \tag{5.6}$$

$$\gamma = \frac{1}{2n_0 - 1)} \frac{d^2n}{dw^2}\Big|_{\omega=\omega_0} + \frac{1}{\omega_0(n_0 - 1)} \frac{dn}{dw}\Big|_{\omega=\omega_0} \tag{5.7}$$

[4]SEA TADPOLE only measures the spectral phase difference between the two arms of the interferometer which in our measurements is the spectral phase introduced by the lens. At the front surface of the lens, the reference and unknown pulses will have the same spectral phase and therefore this will cancel out in the measurements

To model the foci in our measurements we used Eq. 5.3 and the formulas above for the aberrations as well as some ray tracing. For all of the lenses that we used in our measurements, the refractive index (including the dispersion formula or Sellmeier equation for this material), the radius of curvature for each surface, and the aperture diameters were provided by the manufactures. Once we have calculated $E(r, \omega, z)$ using the above integral, this can be Fourier transformed to obtain $E(r, t, z)$.

Note that Eq. 5.3 does assume that the lens is a singlet lens (or that it only contains 2 surfaces), but as long as the lens can be broken down into a cascade of thin single-element lenses so that $\Theta(r_1, \omega) = \Theta_1(r_1, \omega) \times \Theta_2(r_1, \omega) \times \ldots$, this integral can still be used with little error. We have used this approach to model doublets (lenses with three surfaces) but most of our experimental tests were done using singlet refractive lenses.

5.1.3 Radially varying group delay

A simple and informative expression for the group delay as a function of r and ω can be derived from Eq. 5.3 without numerically solving the integral. This expression, which was taken from reference [81], is shown below.

$$\tau(r, \omega, z) = \frac{3Ar^4}{c} + \frac{1}{2c}\Big(\frac{1}{z} - \frac{1}{f_0}\Big)r^2 - \alpha r^2 - \gamma(\omega - \omega_0)r^2 \tag{5.8}$$

Keep in mind, that $k = \omega/c$ and therefore all of the terms containing k's contribute to the group delay which is where the first two terms in Eq. 5.8 come from.

The first term in Eq. 5.8 is due to spherical aberrations which result in a quartic pulse front. The second term is known as the "defocus" term and this would be the only term present if there were no aberrations. You can see that at $z = f$ this term goes to zero, meaning that the pulse front would be flat at the focus of an ideal lens as shown in Fig. 5.1. The third term, which is also an r^2 term like the defocus term, is due to chromatic aberrations, but this term does not change as the pulse propagates (it has no z dependence). Interestingly, chromatic aberrations have the

effect of shifting the flat pulse front away from the focus. From Eq. 5.8 combined with Eq. 5.6 (assuming that $\gamma = 0$) you can see that if chromatic aberrations can cause the flat pulse front to be at a distance $L = \frac{f}{n-1}\Big(- \lambda \frac{dn}{d\lambda}\Big)$ after the focus (this equation, without the spherical aberration term was first derived in [68, 83]). If the pulse front is curved at the focus, its pulse duration becomes larger because it center of the beam will be ahead or behind in time of the edges of the beam. In the next section will show our measurements of this effect.

The final term, which is often very small and negligible, is the radially varying group delay dispersion. This term comes about because the varying thickness of the lens chirps different parts of the beam by different amounts(more at the center of the beam than on the edges for a convex lens). This distortion is usually negligible unless the numerical aperture of the lens is very high (greater than 0.4) because tighter foci involve using lenses with rounder surfaces. In chapter 6 when measure high NA foci, we will discuss this effect in more detail.

5.2 Details of the method scanning SEA TADPOLE

To use SEA TADPOLE to measure $E_{unk}(\omega)$ at one point in space, we temporally overlap and couple the reference and signal pulses separately into short single-mode fibers, as shown in Fig. 5.4. One focal length after the fibers, we place a spherical lens (of focal length f) to collimate the light diverging from the fibers. Because each of the fibers is slightly displaced from the optic axis (each by a distance $\pm d$), the collimated beams cross, yielding horizontal interference fringes that are recorded with a digital camera. The beams also pass through a diffraction grating and a lens, so that wavelength is mapped to the horizontal position of the camera to yield the two-dimensional SEA TADPOLE trace $S_{ST}(\omega, x)$.

To reconstruct $E_{unk}(\omega)$ from this trace, we Fourier filter the interferogram along the x axis and then divide out the reference field yielding the unknown pulse field

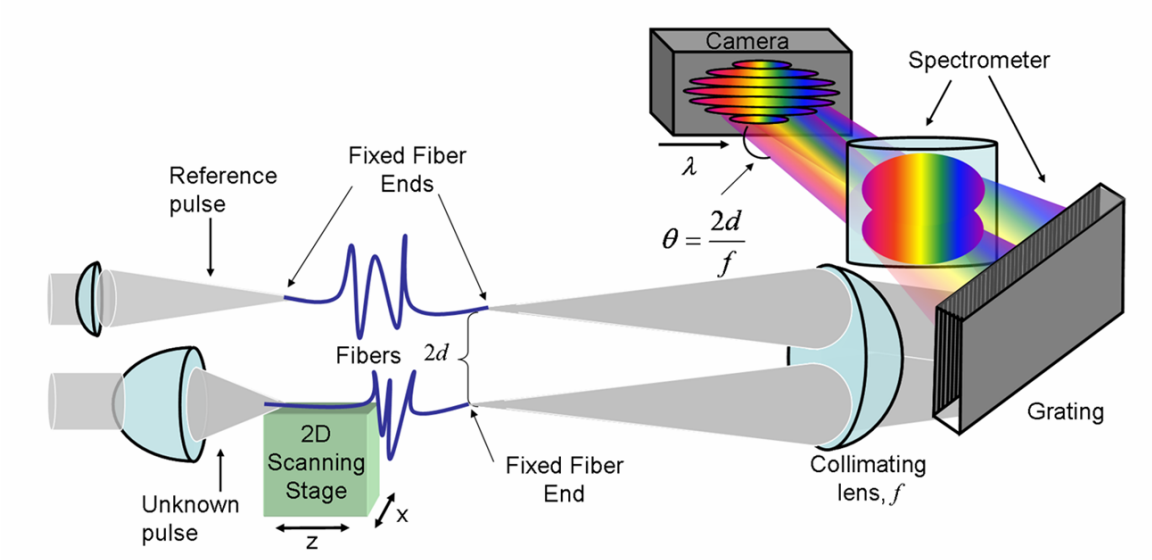

Figure 5.4: Experimental setup for scanning SEA TADPOLE

$E_{unk}(\omega)$. Because the Fourier filtering is done with respect to x and k_x, rather than ω and t, no spectral resolution is lost in this reconstruction. On the other hand, even though the SEA TADPOLE trace is two-dimensional, all of the unknown beam's spatial information is lost in the fiber, so that only $E_{unk}(\omega)$(of the sampled spatial region of the beam) is constructed from a single SEA TADPOLE trace. For more details about SEA TADPOLE see 2.

To measure the unknown pulse as a function of both time and space, we simply scan the position of the unknown-pulse input fiber in x, y, and z and measure many traces, assuming that the input pulse train remains stable throughout the measurement, resulting in $E_{unk}(x, y, z, \omega)$. See Fig. 5.4.

When the unknown fiber is moved to different longitudinal positions z, we must readjust the delay stage so that the pulses again temporally overlap (this is done by our data acquisition computer program).

5.2.1 Loss of the spatial phase in scanning SEA TADPOLE

As discussed previously [51, 64], the use of optical fibers in an interferometer can cause a slow drift in time in the measured absolute phase of a pulse due to small changes in the optical path lengths due to temperature fluctuations. In our measurements, the absolute spectral phase as a function of x, y, and z is the spatial phase of the pulse, so, if the absolute phase drifts faster than our scanning time, as it does here, then we are unable to measure the spatial phase. With our current setup, however, we can measure every other aspect about a focusing pulse. In particular, we are able to measure all other phase terms, including the spectral phase and the phase terms that depend on both x or y and ω such as the radially dependent group delay and the radially dependent group-delay dispersion. Additionally we can measure the amplitude of the electric field versus x, y, z and ω. In other interferometric techniques in which fibers are used, it has been reported that simply enclosing the interferometer in a plastic box largely eliminates the phase drift [64]. Therefore, in principle SEA TADPOLE could also easily measure the spatial phase of the pulse. In this study we are primarily interested in knowing the spatiotemporal couplings of a focusing pulse, such as the pulse fronts and the position dependent spectrum, which can be measured by scanning SEA TADPOLE without stabilizing the interferometer, so we have not done this.

Appendix B shows a measurement of the drift in our interferometer as well as some examples of how this drift distorts the measured spatial phase.

5.3 Measurements of focusing pulses

To test scanning SEA TADPOLE, we measured ultrashort pulses focused by various lenses. We measured $E_{unk}(\omega)$ for numerous values of x and z at $y = 0$, and then Fourier transformed the measured data to the time domain to obtain $E_{unk}(x, z, t)$ (with interpolation to increase the number of data points on the time axis from 10 to

90). While we could have scanned in y as well, scanning in only one transverse dimension was sufficient to measure a pulse front with spherical and chromatic aberrations for the purpose of testing our technique.

Although we know the intensity and phase of our reference pulses (we routinely monitor the output of our laser with a Swamp Optics GRENOUILLE), in these experiments the interesting quantity for scanning SEA TADPOLE was the phase introduced by the lens. So in all of our measurements we measured the phase difference in the two arms of SEA TADPOLE with the lens in the unknown arm. Therefore the following measurements show only the effects of the various lenses for a given pulse input spot size and bandwidth.

In all of our measurements, our laser source was a KM Labs mode-locked Ti:Sapphire oscillator emitting pulses with rms bandwidths of 18 nm and centered at 800 nm. The rms spot size of the beam before each lens was 2.12 mm and all of the lenses used had diamters of 24.5 mm. Because the beam was sufficiently smaller than the lens' apertures, it was not clipped by the lenses and we did not observe any effects due to the beam diffracting off of the edge of the lens. All of the lenses studied were oriented so that collimated beam entered through the curved surface, which is the orientation that minimizes spherical aberration. Our optical fibers had a 5.6μm mode field diameter. Each measurement of $E_{unk}(x,t)$ took 2-3 minutes, and the measurements at different z's were all made continuously. The remainder of the details of our set up are described in chapter 2 or can be found in the following references [50, 51, 55].

To confirm our measurements, we also performed simulations of pulses propagating through the various lenses used in our experiments as described in the previous section.

The first lens that we considered was an 50 mm focal length aspheric lens made of molded PMMA, which is designed to have minimal spherical aberration, but which exhibits chromatic aberration and, group-delay dispersion (GDD). We measured and

simulated $E(x,t)$ at nine different longitudinal positions, z, around the focus, where $z = 0$ corresponds to the geometric focus. See Fig. 5.5. The experimental results are

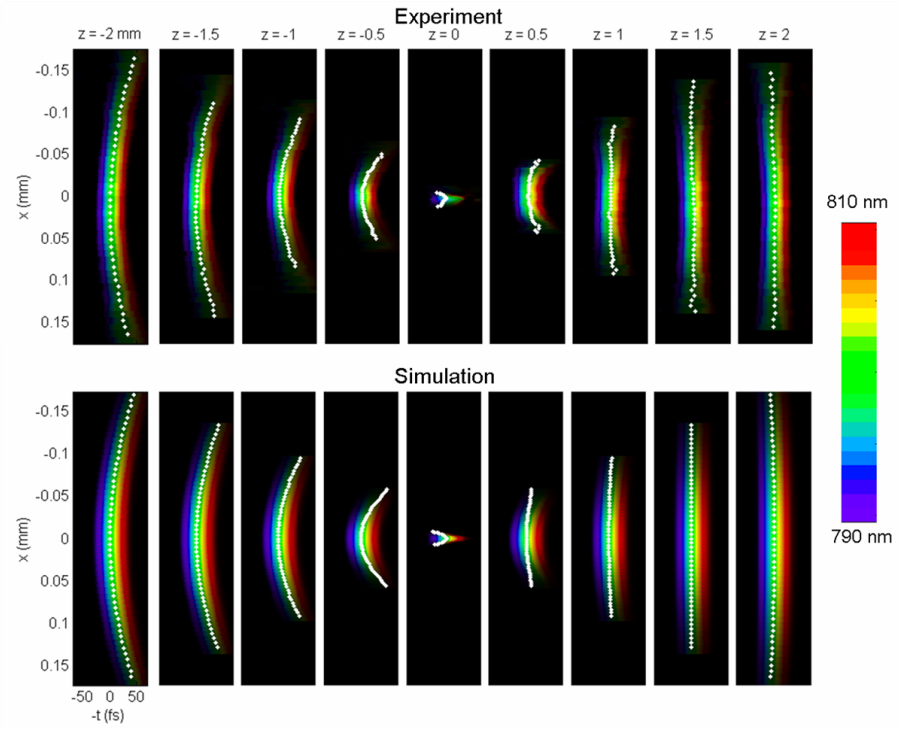

Figure 5.5: Measured and theoretical spatiotemporal field of a pulse focused with an aspheric lens

displayed in the top plots, and the simulations are in the bottom plots. Each box displays the amplitude of the electric field versus x and t at a distance z from the geometric focus. The color represents the instantaneous wavelength as designated by the color bar on the right. Each set of plots displays the amplitude of the electric field versus $-t$ (so that the leading edge of the pulse appears on the right) and x at a particular longitudinal distance away from the focus. The white dots display the pulse front (defined as the maximum temporal intensity at each x).

In the absence of dispersion and aberrations, the instantaneous wavelength would be the same everywhere in space and time as shown in Fig. 5.1. GDD and aberrations, on the other hand, cause color variations. For the aspheric lens, we expect color variations due to both GDD and chromatic aberration, but, for this particular lens,

the effects of chromatic aberration are small compared to those due to GDD, so in all of the plots in Fig. 5.5, the redder colors precede the bluer colors, as expected when material dispersion is present.

While chromatic aberration plays only a small role in the pulse temporal phase, it does become evident, however, in the pulse's temporal intensity and its distortions. For a lens free of aberrations, the pulse fronts are curved and perfectly symmetrical about the focus, and flat at the focus (see Fig. 5.1). Chromatic aberration shifts the position of the flat pulse front to a a position of $L = \frac{f}{n-1}\Big(- \lambda\frac{dn}{d\lambda}\Big)$ after the focus, resulting in pulse fronts that are not symmetric about the focus [68] and as described in section 5.1.3. In Fig. 5.5, it is clear that the pulse fronts are, in fact, not symmetric about the focus, and the pulse front is flat at z = 1.5 mm in both the simulation and experimental data.

The second lens we considered was an $f_0 = 50$ mm achromatic doublet in the form of a meniscus lens consisting of a biconvex BAFN10 lens cemented to a concave-convex SF10 lens. This lens was designed to be free of chromatic aberrations for visible light. The measurements and simulations of the focusing pulses are shown in Fig. 3.

In Fig. 5.6, most of the color variation is again due to the GDD of the lens. Because the doublet is very thick (9.8 mm) and, made of very dispersive glass, it introduces significant GDD, and this lengthens the pulse by about three times more than the aspheric lens does (using rms temporal width of the pulse averaged over x). Also, the pulse fronts are not symmetric about the focus, revealing the presence of chromatic aberration.

We included both spherical and chromatic aberrations in the simulations of this lens. While the two lenses in the doublet do not manage to cancel out the chromatic aberration, they also greatly reduce the spherical aberration, and no noticeable effects of it can be seen in data shown in Fig. 5.6.

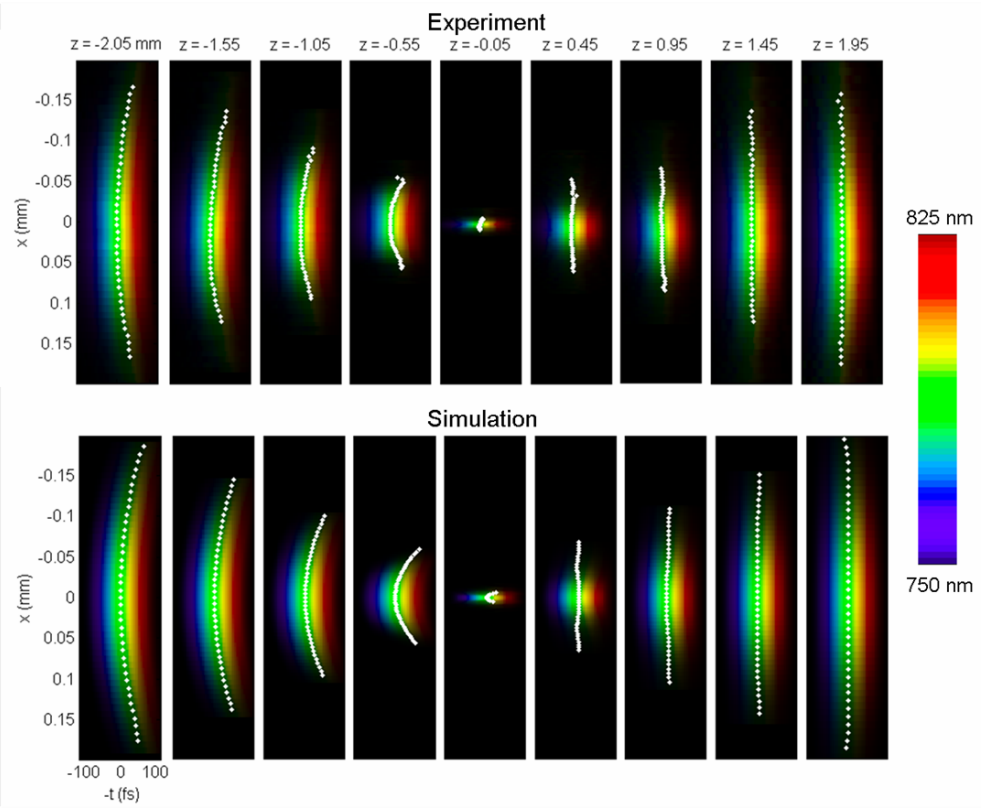

Figure 5.6: Measured and theoretical spatiotemporal field of a pulse focused with an achromatic doublet

In the next set of measurements, we measured the focus using a BK7 plano-convex lens with a focal length of 50 mm. The results for this lens are shown in Fig.

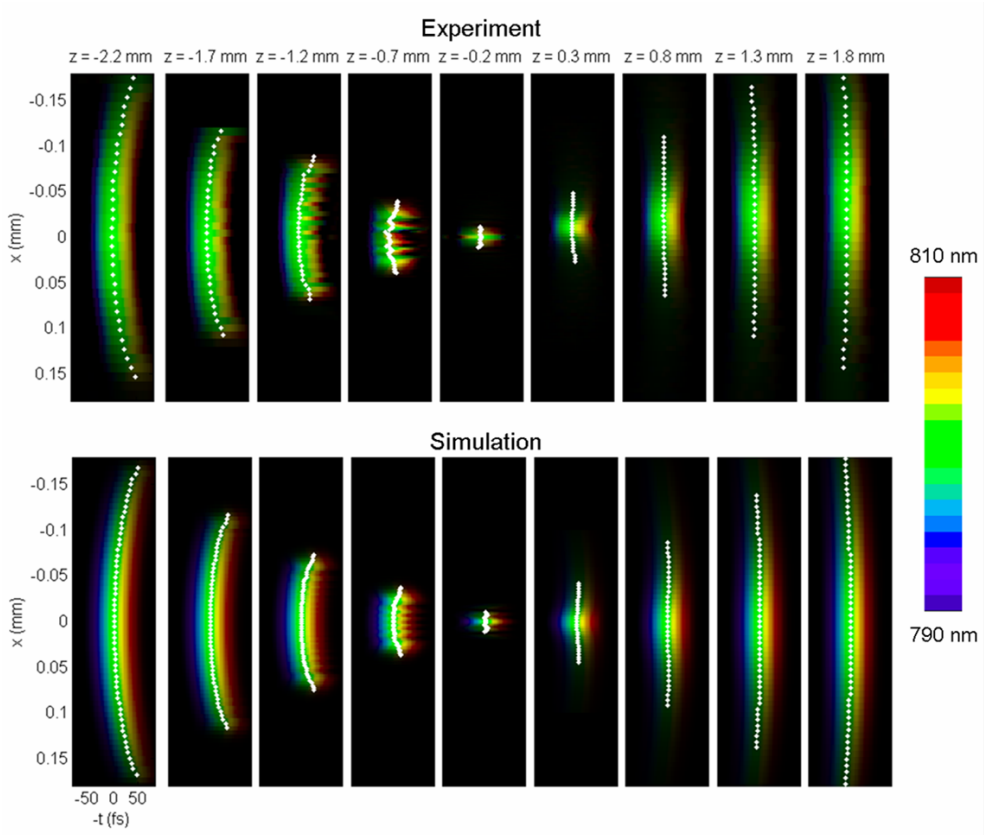

Figure 5.7: Measured and theoretical spatiotemporal field of a pulse focused with a plano-convex lens

This lens contains noticeable amounts of both chromatic and spherical aberration. The most striking feature is the ripples in the spatial profile before the focus mainly at z = -0.7 mm. According to our simulations, the spherical aberration introduced by this lens increases the focused rms spot size by almost a factor of two. Just as with the two previous lenses, the asymmetrical pulse fronts with respect to the focus are a result of chromatic aberration. The pulse front term introduced by spherical aberration has the opposite sign of that due to chromatic aberration as shown in Eq. 5.8. As a result, the flat pulse front occurs closer to the focus than it does for the aspheric lens, when no spherical aberration is present. Just as with the two previous

lenses, most of the color variation in this data is due to the GDD introduced by the BK7 glass.

In the case of spherical aberration, the focus is not well defined in position z. To determine the actual value of z for the focus in the measurements, we picked the value that resulted in the best match between the simulations and the experiments. Here, as in all of the measurements, z = 0 refers to the location of the geometric focus.

There is a small discrepancy between the simulations and experimental data, in the color, or chirp. In our simulations, we used the center thickness of the lens in the spectral phase. It is possible that we made the measurement slightly off axis (so y was not exactly equal to 0), so that the part of the beam that we were measuring did not pass through quite as much glass. Other than this minor discrepancy, the measurements are in good agreement with the simulations

Next we investigated the focal region of a higher NA BK7 lens which had a focal length of 25 mm. The NA of the focus was 0.085 (using the $1/e^2$ full width of the beam before the lens). The simulations and experiments shown in Fig.5.8 are in good agreement. These results look very similar to those shown in Fig.5.7 except that the ripples are more apparent due to the increase in the focal length of the lens and the pulse is more chirped because this lens was thicker(12.8 mm center thickness instead of 6.3mm). This lens also has chromatic aberrations present which cause the pulse fronts to be asymmetric about the focus. The aberrations in this lens increase the focused spot size by a factor of 3.

In our final experiment, we measured the focal region of a plano-convex ZnSe lens. In this measurement, we felt that it would be helpful if we canceled out most of the material dispersion so that the effects of the lens aberrations would appear more clearly. Because SEA TADPOLE measures only the spectral phase difference between its two arms, we were able to cancel out the dispersion of the lens by placing a ZnSe plate whose thickness was equal to the center thickness of the lens into the

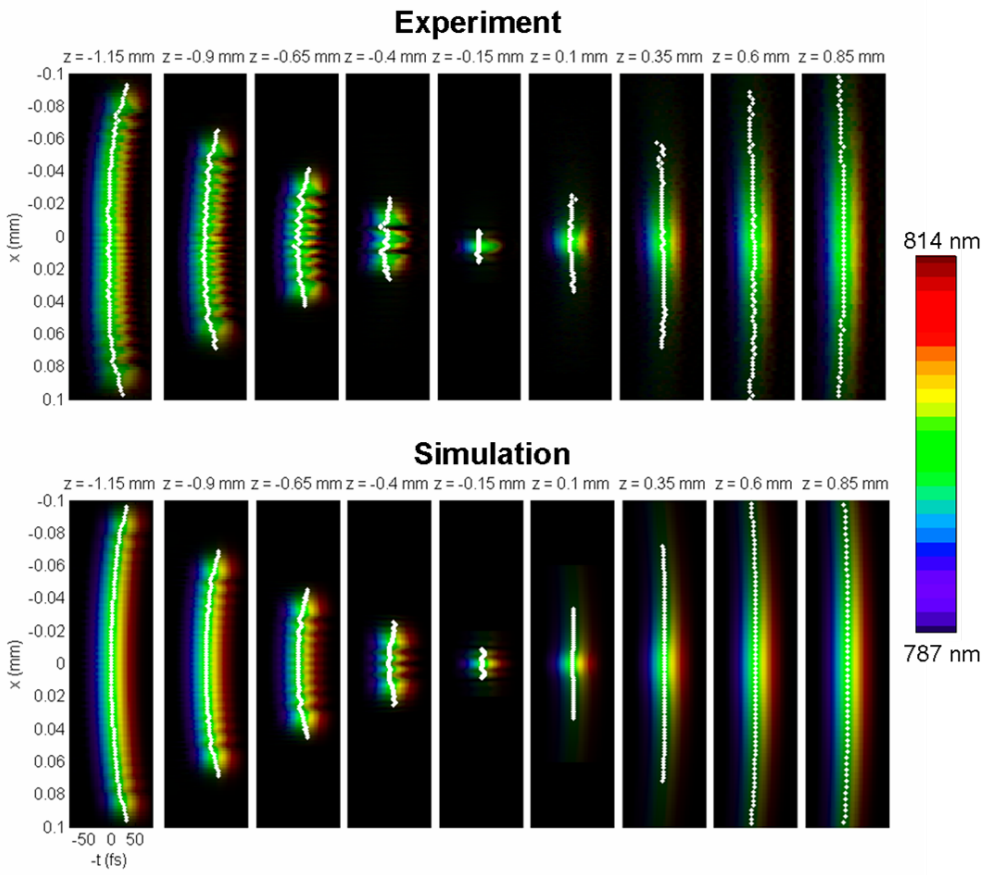

Figure 5.8: Measured and theoretical spatiotemporal field of a pulse focused with a higher NA plano-convex lens

reference arm. Because the radius of curvature of this lens is so large (71.46 mm), this flat plate accurately canceled out the lens material dispersion. As a result, this set of measurements shows what distortions would remain at the focus after perfect material dispersion compensation using, for example, an ideal pulse compressor or a one-dimensional pulse shaper before the lens. And to fully compress this pulse, or to remove these distortions, a two-dimensional pulse shaper, such as the one in this reference would be needed [84] (A different delay has to be introduced at each r to compensate for radially varying group delay).

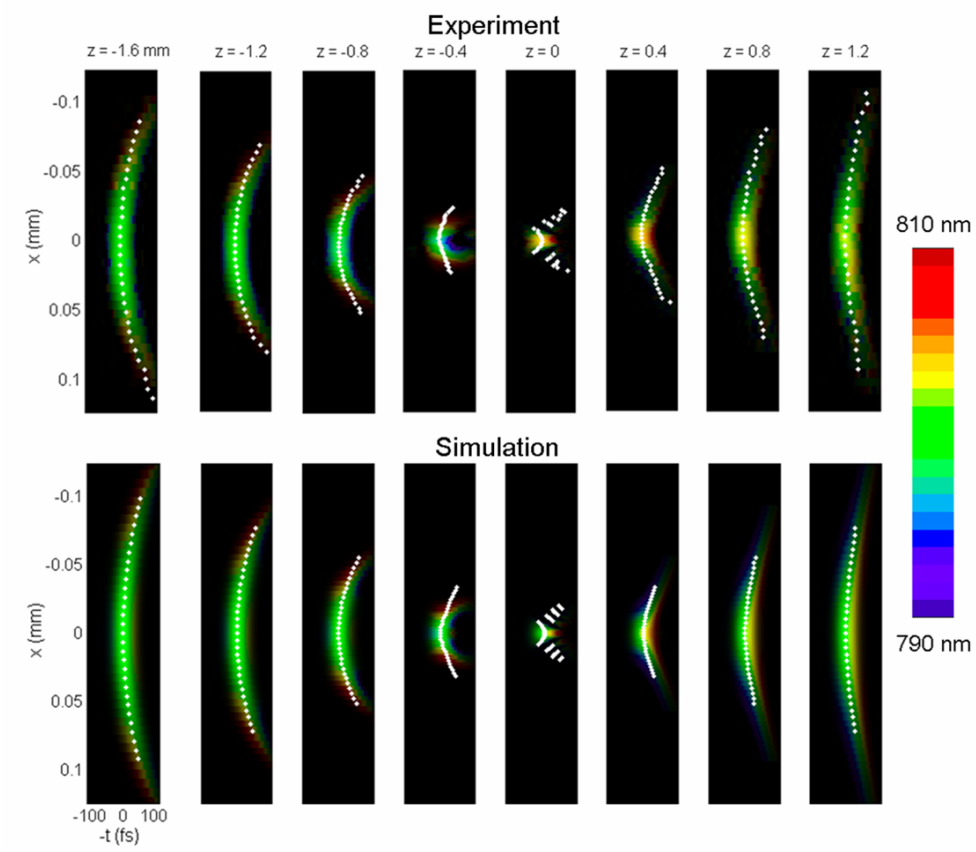

Figure 5.9: Measured and theoretical spatiotemporal field of a pulse focused with a znse lens

The results are shown in Fig. 5.9. While the ZnSe lens has much more chromatic aberration than the other lenses (5 times that for PMMA and BK7 using the chromatic aberration coefficient as derived in reference [68]), it actually has less spherical

aberration than the BK7 lens (by a factor of about 2.5 using the spherical aberration coefficient from reference [81]). Therefore, essentially all of the distortions and color variations seen in the data are due to chromatic aberration. For this lens, even if the spectral phase of the pulse at the focus is constant, the pulse duration is still 29% longer at the focus (with a bandwidth of 25 nm) than the transform-limited pulse duration-due to the chromatic aberration.

As with the previous lenses, the pulse fronts are asymmetric about the focus due to the chromatic aberration. For this lens, the flat pulse front occurs 6.5 mm after the focus, which is out of the range of our data. At the focus, the chromatic aberration results in some ripples, which are marked with the white dots. Note that, before the focus, the redder colors have a larger spot size, and they are ahead in time. Similarly, the pulse is bluer closer to x = 0. Both of these effects occur because chromatic aberration causes the bluer colors to focus before the redder colors.

To better show the distortions present in this pulse, we have produced a movie of it. See Fig. 5.10. The movie consists of 16 measurements of $E(x,t)$ at different values of z, which we interpolated along the z axis to yield 114 frames. These images range from z = -1.4 mm to z = +1.6 mm. Observe the color of the pulse close to z =0 (where the spot size is minimal), and note that it changes from blue, to green, to yellow, and finally to red, which is due to chromatic aberration.

The input beam that we used was the pulse directly out of our oscillator without spatial filtering in order to avoid seeing any aberrations from the lenses in the spatial filter in our measurements. We assumed that the input beam was relatively free of aberrations, and, because the agreement between our simulations and experiments is generally good, it is evident that this assumption is largely correct. For example, if the input beam had had chromatic aberrations that were comparable in size to those introduced by the lenses, then the flat pulse front in Fig. 5.5 would not have occurred close to the $z = 1.5$ mm plane. It is also obvious that very little spherical aberration

(movies/znse.avi)

Figure 5.10: (Click on the above picture to start the movie) $E(x,t)$ where each frame is a different z.

is present in the input beam because signs of spherical aberrations (ripples in the intensity versus x) are not present in all of our data. By the same logic it is clear that the lens was well aligned, meaning that the beam passed through the center of the lens and that the lens was not tilted with respect to the beam's path. If this had not been the case, then aberrations such as coma and astigmatism would be present in the measurements, and the measured data would not have agreed with the simulations (in which we only included chromatic and spherical aberrations). It is possible that the small discrepancies between our measurements and simulations can be attributed to the input beam or the alignment of the lens.

5.4 Measuring focusing pulses in the presence of linear spatiotemporal distortions

Linear spatiotemporal distortions refer to $x\omega$, xt, $k_x x$ or $k_x\omega$ cross terms in the electric fields of ultrashort pulses [27, 85]. Examples of these distortions include angular dispersion (where different colors have different k-vectors), spatial chirp (where different positions on the beam have different center frequencies), or pulse front tilt (where the arrival time of the pulse varies linearly from the top of the beam to the bottom of the beam). The distortions due to the radially varying group delay (see section 5.1.3 that are introduced by lens aberrations are higher order spatiotemporal distortions (they are ωx^2, $\omega^2 x$, or ωx^4 couplings).

Unfortunately linear spatiotemporal distortions are difficult to avoid because they are produced by diffraction gratings and prisms which are present in nearly every application of ultrashort pulses including the laser's themselves. Just as with lens aberrations, linear spatiotemporal distortions are unwanted because they make the pulse duration longer and therefore the intensity weaker. As we mentioned earlier in this chapter, ultrashort pulses are almost always used at a focus. When linear spatiotemporal distortions are present, these distortions of course remain at the focus and make the pulse duration and the spot size there larger.

Linear spatiotemporal distortions have been measured in collimated beams in the past [29, 86, 87]. Here we measure the focal region of pulses that contain linear spatiotemporal distortions before being focused to study the effects of these distortions on the focus. To test our measurements we modeled these foci using the method described in 5.1.2. To calculate the spatiotemporal field just before the lens and account for the linear spatiotemporal distortions that we introduced, we used a method know as Kostenbauder matrices [27, 88], which is just a matrix method of solving the Huygens-Fresnel integral to second order (see the reference for more information).

In the first measurements we focused a beam which had angular dispersion and then measured the spatiotemporal field in and around the focus. To introduce angular dispersion we used the -1 order of a ruled reflection grating (300 g/mm) which we placed just before (by 17.5 cm) the focusing lens. The results of this experiment are shown in Fig. 5.11.

The experiment and simulation are in good agreement. Because a lens is a Fourier transformer, the angular dispersion introduced by the grating becomes spatial chirp at the focus. As a result, the pulse front becomes flat at the focus, because the pulse front tilt in this case is due to angular dispersion. Because the magnification of the optical system becomes negative after the focus, the order of the colors and the sign of the pulse front tilt change after the focus. This measurement essentially shows the pulse in the focal region of a spectrometer. The lens that we used in this experiment is the aspheric lens from Fig. 5.5, though the distortions due the chromatic aberrations are not noticeable because theses effects are much larger than those due to the chromatic aberrations.

In another similar measurement we added spatial chirp to the pulse before focusing it (also with the 50mm focal length aspheric lens). To do this we propagated the pulse through a pair of parallel transmissive diffracting gratings with grove densities of 700 grooves/mm and a spacing of 25 mm between the two gratings. After the first grating

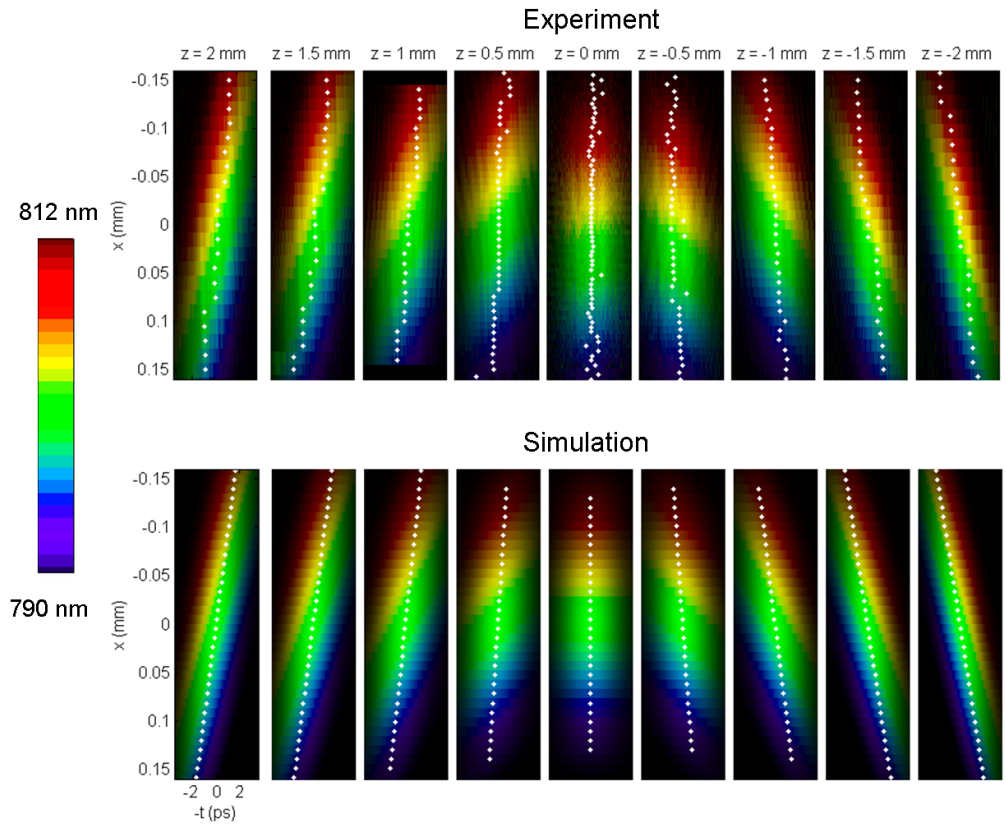

Figure 5.11: $E(x, z, t)$ in the focal region of beam which had angular dispersion

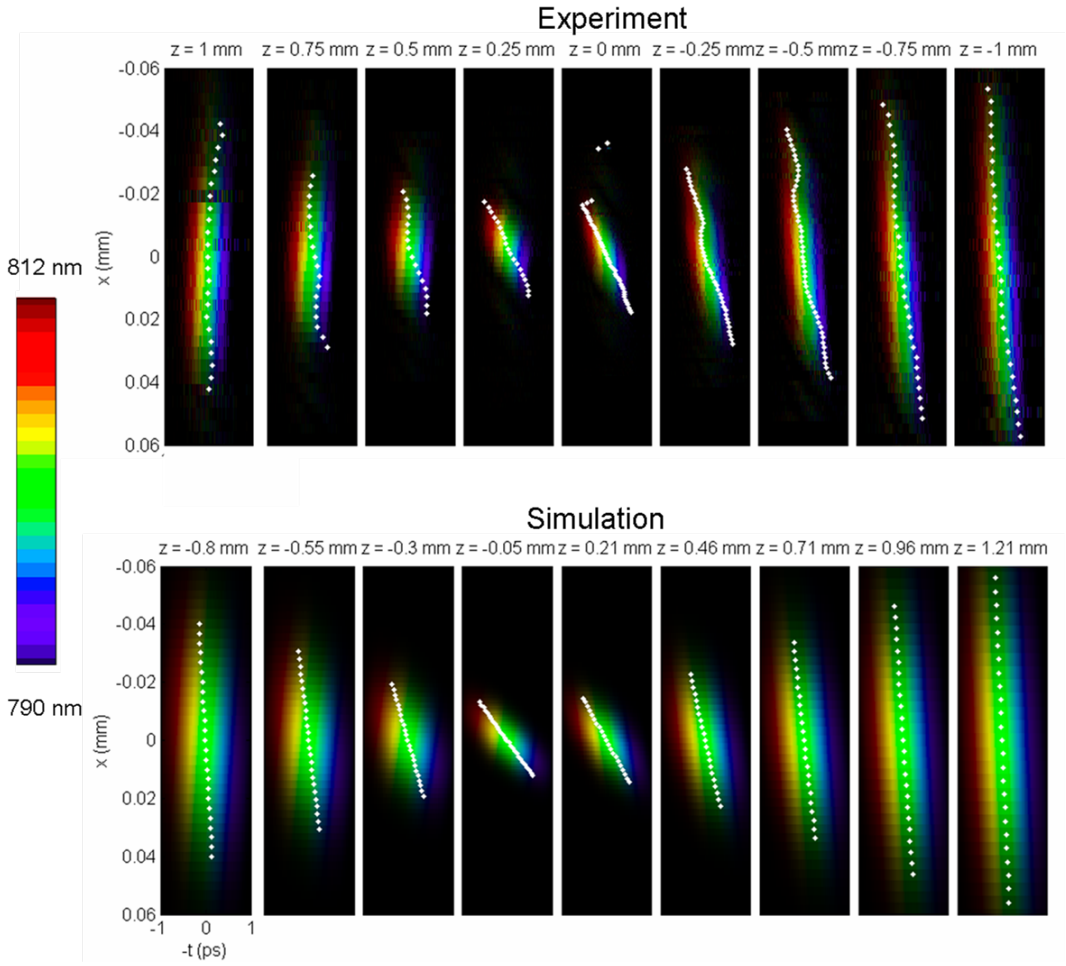

Figure 5.12: $E(x, z, t)$ in the focal region of beam which had spatial chirp

we used only the -1 order and at the second grating we used the +1 order so that the outgoing beam was parallel to the incoming beam and it contained no angular dispersion, only spatial chirp (see reference [23]). Then we focused this beam and made the measurement that is shown in Fig. 5.12.

Again, because a lens is a Fourier transformer, at the focus the spatial chirp should vanish and there should only be angular dispersion present. As you can see at z=0, there is still a little spatial chirp present. This is likely because the two diffraction gratings were not perfectly parallel so that there is a little angular dispersion present in this beam as well (which becomes spatial chirp at the focus). In practice it is difficult to get the gratings to be exactly parallel, and at best we can align them with $\sim 3^\circ$ accuracy. To match our simulations to the measurements we said that the second grating was off by 1° (too small to see in the lab) and you can see that makes the simulations agree reasonable well with the measurements.

Both of the measurements shown in the section show the importance of having a pulse that is free of linear spatiotemporal distortions in order to achieve a small homogenous focused spot size with a short pulse duration.

5.5 Spatial resolution in scanning SEA TADPOLE

When using scanning SEA TADPOLE to collect spatial information about a focusing pulse, a few questions arise. For example, what is the spatial resolution achieved by sampling the beam with a fiber, and what is the acceptance angle of the fiber. In a previous paper [55], we argued that these two questions are equivalent, and so if a SEA TADPOLE device has sufficient spatial resolution to sample a given focus, then it also has sufficient angular acceptance to measure that focus. In this section we consider this issue in more detail, further clarifying this point.

To determine the acceptance angle and spatial resolution of the fiber, we consider the effect of the fiber's finite spatial resolution as a convolution just as we did with

the spectral resolution is chapter 3. For this discussion, we will ignore the effects of the finite spectral resolution and we will assume that the fiber's spatial resolution along the x and y axes is the same so that we can only consider one transverse spatial dimension.

When the fiber spatially samples the field of the focusing pulse $E_{unk}(x,\omega)$, this field is spatially averaged over the fibers mode (or the aperture) so that any spatial features that are as small as the the mode size of the fiber (or the averaging window) get smeared out. Therefore, the spatially sampled field can be written as $E_{unk}(x,\omega) \otimes H(x)$ where $H(x)$ is the point spread function, or the spatial response function that is given by the shape of the fiber's mode.

The sampled field can be Fourier transform to the k domain, where it becomes, $E_{unk}(k_x,\omega) \otimes h(k_x)$. The function $h(k_x)$, which is referred to as the transfer function [89], can be viewed as an angular window, just as the temporal response function $h(t)$ forms a time window. This product of the field with the angular response function is zero anywhere that $h(k_x)$ is zero, so only a certain range of k-vectors will be coupled into the fiber. Therefore, because the fiber has a finite spatial resolution, it will also have a finite acceptance angle where we define the acceptance angle is width of the transfer function. The above Fourier transform relation shows knowledge of the spatial resolution will yield the acceptance angle and visa versa.

To derive an expression for the acceptance angle of a single-mode fiber, the power transmitted into the fiber should be calculated shown as below.

$$T = \Big[\int_{-\infty}^{\infty} dx \int_{-\infty}^{\infty} dy E_{fiber}(x,y) E^*_{unk}(x,y) \Big]^2 \tag{5.9}$$

This integral is a measure of the spatial overlap of the mode of the fiber with the mode of the unknown pulse [90, 91]. $E_{fiber}(x,y)$ is approximately equal to a Gaussian with a width (full width at e^{-1}) equal to the single-mode field diameter d of the fiber. For a Gaussian beam with a waist size (diameter) w (where $w > d$) with an incident angle into the fiber (with respect to the fiber axis) of θ, it has been shown [91] that

the power coupled into the fiber as a function of θ is given by:

$$T = \Big(\frac{2dw}{d^2+w^2}\Big)^2 \exp\Big[-\frac{2(d\pi w\theta)^2}{(w^2+d^2)\lambda}\Big]. \tag{5.10}$$

In order to isolate the effects of transmission loss due to a potentially large incident angle, we consider the power transmitted over the cross sectional area of the incoming beam overlapping with the fiber's core by setting d to w so that Eq. 5.10 becomes,

$$T = \exp\Big[-\frac{(d\pi\theta)^2}{4\lambda^2}\Big]. \tag{5.11}$$

Equation 5.13 shows that the transmission of the unknown pulse into the fiber has a Gaussian dependence on the incident angle. If we take the acceptance angle of the fiber θ_{max} to be the full width of $T(\theta)$ at e^{-2}, then we find that it is given by $\frac{2\lambda}{\pi d}$. The angular window $h(k_x)$ is identical to $T(\theta)$ (where $\theta \approx \frac{k_x\lambda_0}{2\pi}$), and the fiber is Gaussian angular filter. Thus, as long as we measure pulses whose NA's are less than $\frac{2\lambda}{\pi d}$, $E_{unk}(x,\lambda)$ will experience minimal angular filtering and be accurately sampled by the fiber because $T(\theta)$ is relatively flat in this region.

Because we know that the spatial response function is a Fourier transform of $h(k_x)$ we can write it as follows:

$$H(x) = \exp\Big[-\frac{(2x)^2}{d^2}\Big]. \tag{5.12}$$

If we take the spatial resolution of the fiber to be the full width of $H(x)$ at e^{-2} , then we get the expected result that it is equal to the mode diameter of the fiber(d).

Because $H(x)$ and $h(k_x)$ are a Fourier pair, θ_max is related to the mode diameter as shown above, so we can see that the acceptance angle of the fiber is determined by the mode diameter. Therefore, if we require that the focusing pulse to be measured has an NA that is less than the acceptance angle of the fiber, then we get the condition that

$$\frac{2\lambda}{\pi w} < \frac{2\lambda}{\pi d} \tag{5.13}$$

where we have assumed that the focusing pulse is Gaussian with a focused spot diameter of w. From the above equation, we can see that this requirement on the

NA is equivalent to requiring that the mode diameter of the fiber be smaller than the focused spot size of the pulse, which is necessary if we are to spatially resolve the incoming pulse. Therefore, if we use a fiber with sufficient spatial resolution for a given focus, then it will also have a sufficient angular acceptance.

In the above discussion we assumed that the incoming Gaussian beam was free of aberrations. Because aberrations will only increase the size of the focus, requiring that the fiber mode be less than the size of the focus when no aberrations are present will be sufficient. And if aberrations are present, the fiber will still accurately sample the focus.

As we have explained in chapter 3, we find that it can be advantageous to measure the spectrum using the interferogram rather than directly measuring it because the spectral resolution of SEA TADPOLE can be better than that of a spectrometer. Because we also interferometrically measure the spatial intensity of the focusing pulse (we reconstruct $E(x, y, z, \omega)$), we achieve a spatial-resolution improvement in SEA TADPOLE compared to what we would get with direct measurements of the spatial intensity using the same fiber. This is illustrated in the measurement shown in Fig. 5.13 where we measured $E(x, \omega)$ with SEA TADPOLE for a Bessel beam that had very fast oscillations. To make these measurements we used a single mode fiber with a core size around 5 μm. You can see that the fringe spacing is only $3.4\mu m$ in the beam's spatial intensity but it is still clearly resolved in our measurement.

5.5.1 Measuring the transfer function of an optical fiber

Just to confirm our analysis above, we measured $h(k_x)$ for the single mode fibers that we used in our measurements and fourier transformed this to obtain $H(x)$. To measure $h(k_x)$, we measure the coupled power of a large Gaussian beam into the fiber as a function of the angle that the beam's axis makes with the fiber's axis as was done in reference [89]. To vary this angle, we mounted the fiber's end to a rotation stage

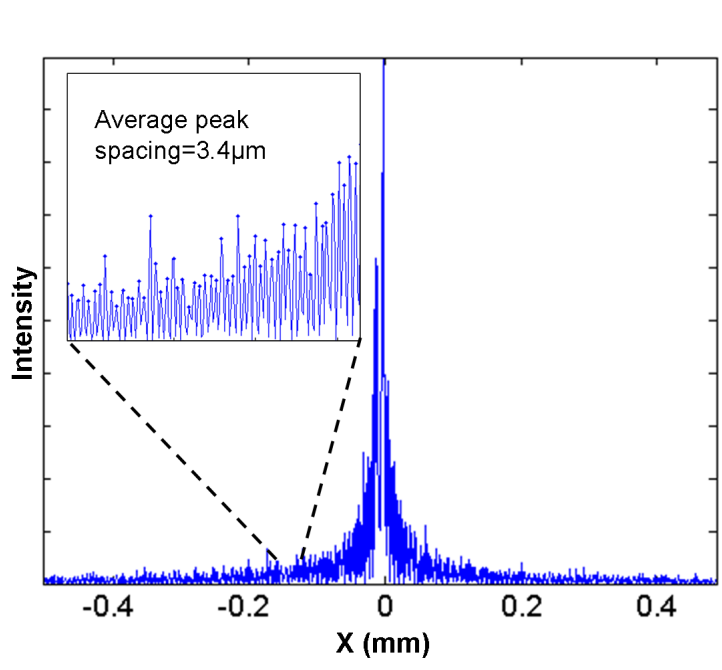

Figure 5.13: Spatial intensity measured with SEA TADPOLE for a Bessel beam

translated the fiber back the center of the beam after each rotation (just by optimizing the power at each angle). Figure 5.14a shows a schematic of the experimental setup for this, and the results of the measurement are shown in Fig. 5.14b. As you can see, the measured transfer function is approximately Gaussian as we expected. The measurement is a little noisy which is due to the fact that very little light was coupled into the fiber because our beams spot's area was about 32,000 times larger than the of the fiber's mode. The acceptance angle of the fiber can be taken as the full width of $T(\theta)$ at e^{-2} which is 21°, giving a numerical aperture of 0.17 which is in close agreement to that specified by the manufacturer which was 0.14.

This verifies that scanning SEA TADPOLE should be able to accurately sample focusing pulses with numerical apertures less than 0.17.

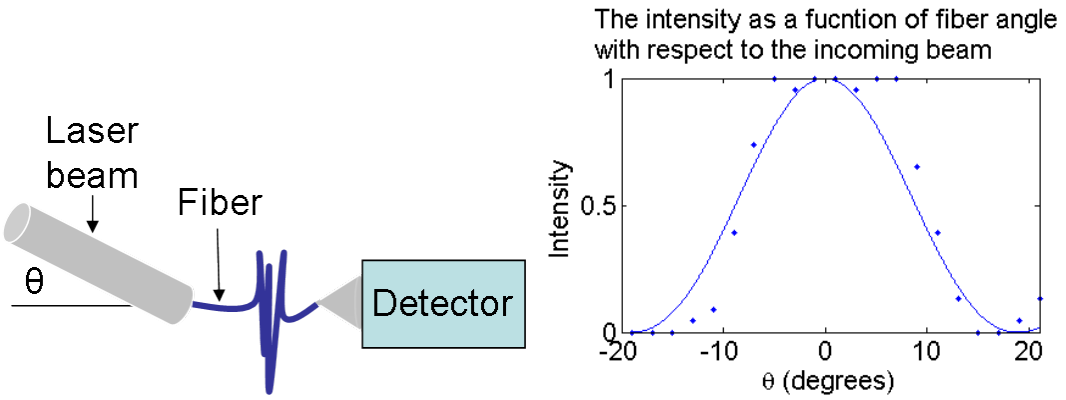

(a) Schematic to measure $h(k_x)$

(b) Measured $h(k_x)$ for a single mode optical fiber

Figure 5.14: Measuring the transfer function of a single mode fiber

5.6 Conclusions

In this chapter a technique for directly measuring the spatiotemporal electric field of a focusing pulse was discussed. To make these measurements, we spatially sample the focusing beam with by scanning the entrance optical fiber of SEA TADPOLE. To illustrate our technique, we measured $E(x, z, t)$ for an aspheric lens, an achromatic doublet, and two plano-convex lens, all having an NA's = 0.04, or 0.09. We also measured the focus of a ZnSe lens with chirp compensation, in order to illustrate the distortions that can remain in focused pulses even after perfectly compensating for the material dispersion introduced by the lens' center thickness. To confirm our measurements, we performed simulations by numerically propagating Gaussian pulses through the lenses used in the experiments. The agreement between the simulations and experiments is good.

CHAPTER VI

MEASURING THE SPATIOTEMPORAL ELECTRIC FIELD OF ULTRASHORT PULSES WITH SUB-MICRON SPATIAL RESOLUTION

6.1 Introduction and background

In the previous chapter a version of SEA TADPOLE for measuring focusing ultrashort pulses was described. As we explained, scanning SEA TADPOLE is limited to measuring foci with numerical apertures less than that of the single mode fiber which is around 0.15. In this chapter we discuss a version of scanning SEA TADPOLE that uses near field scanning optical microscopy NSOM fibers probes to achieve sub-μm spatial resolution so that tightly focused ultrashort pulses and the interesting distortions that they experience can be measured [92].

6.1.1 Motivation

In Fig. 5.2 in Chapter 5 we showed a simulation to illustrate that very complicated distortions can occur when ultrashort pulses are focused due to commonly occurring, and difficult-to-avoid lens aberrations, and this is also shown in many publications [15, 66, 68, 81, 93–96]. For example, the so called "fore-runner pulse" which is an additional pulse well ahead of the main pulse, has been predicted to occur at and near the focus when chromatic aberrations are present and the lens is overfilled [68, 97] (This is the case that we simulated in Fig. 5.2). Calculations have also shown that severe spherical aberrations produce Bessel-like pulses (meaning that they have similar properties to "X-pulses" such as those described in [16]), which have spatiotemporal

intensities shaped like an "X" [15, 81]. Other effects such as radially varying group-delay dispersion (see section 5.1.3), or a pulse that is more chirped at its center than on its sides, are expected to occur at the foci of some lenses. Because focused-pulse distortions are usually spatiotemporal and require a spatiotemporal measurement technique simultaneously having sub-micron spatial resolution, femtosecond temporal resolution, and high spectral resolution, many of these distortions have never been directly observed.

Indeed, the focus is a very important place to measure a pulse because this is where most experiments take place, so the quality of experiments often greatly depends on the pulse's properties there. For example, in multi-photon microscopy, the resolution of the microscope depends on the spot size of the focus, and the two-photon excitation efficiency (and hence the microscope sensitivity) depends on the pulse duration. As a result, a transform-limited pulse and diffraction limited spot size are usually desired. Ultrafast micro-machining has similar requirements. When spatiotemporal distortions are present, such as those that can result from lens aberrations, it is difficult to compress the pulse, and a two-dimensional, or a spatiotemporal pulse compressor is needed.

In Chapter 2 we described SEA TADPOLE which can measure very long pulses using a simple experimental setup and we demonstrated that this technique can accurately measure complex shaped pulses with time bandwidth products as high as 400. And as explained in chapter 5, because the entrance to SEA TADPOLE is a single-mode optical fiber, it also has spatial resolution, which is limited only by the fiber mode diameter (in our initial work, we used a fiber with a 5.4 μm diameter). By scanning the fiber in space and making many measurements of $E_{unk}(\omega)$ at different positions all along the focusing beam's cross section, we have used this device to measure the spatiotemporal electric field of pulses [55]. As long as the focus to be measured has a numerical aperture (NA) less than that of the fiber, SEA TADPOLE

has sufficient spatial resolution and acceptance angle to measure the spatiotemporal electric field of a focusing pulse. This has allowed us to measure the spatiotemporal field of focused pulses with NA's of up the 0.12 or with focused spot sizes larger than 5.4μm.

In this chapter another new version of SEA TADPOLE is described, which uses an NSOM (Near Field Scanning Optical Microscopy) fiber probe in place of the single mode optical fiber to extend our spatial resolution to be < 1 μm [98, 99]. NSOM has been used in the past to measure the spatial intensity distribution of tightly focused continuous-wave lasers [100]. Using an NSOM probe with an aperture diameter of 500 nm, we have measured $E_{unk}(x, y, z, t)$ (where the unknown pulse is the focusing pulse under investigation) for focused pulses with NAs as high as 0.44 and features in their intensity $< 1\mu$m. Using this device we observe some of the severe focused-pulse distortions previously predicted, but never directly observed, such as radially varying group-delay dispersion, an "X-shaped pulse", and the "forerunner pulse".

6.1.2 Numerically modeling focusing ultrashort pulses with high NA's

In section 5.1.2 we showed how to calculate the spatiotemporal field for focused pulses using the Fresnel integral, but this approach is only valid for numerical apertures is less than 0.4 (even less according to this reference [101]). Now that we are using NSOM fibers in SEA TADPOLE, we have no restrictions on the NA of the pulse that we can measure (NSOM probes with apertures as small as 10nm are available) and therefore we need a simulation that does not have this restriction.

There are several approaches to modeling high numerical aperture pulses, and here we choose to use the approach described in [15]. The Fresnel integral is an approximation of the Kirchhoff integral which is shown below.

$$E(x, y, \omega, z) \propto \int_{-\infty}^{\infty} dx_1 \int_{-\infty}^{\infty} dy_1 E(x_1, y_1, \omega, 0)\Theta(x_1, y_1, \omega)\frac{\exp(ik\rho)}{\rho^2}z \tag{6.1}$$

$$\rho = \sqrt{z^2 + (x_1 - x)^2 + (y_1 - y)^2} \tag{6.2}$$

In Eq. 7.2, $E(x_1, y_1, \omega, 0)$ is the field just before the lens and $\Theta(x_1, y_1, \omega)$ is the intensity and phase introduced by the lens (So $E(x_1, y_1, \omega, 0) \times \Theta(x_1, y_1, \omega)$ is the field just after the lens). This integral takes the beam just after the lens, and says that each point on the beam emits spherical waves that have an intensity and phase of the field just after the lens at that specific point. Then the spherical waves after propagating a distance z are summed together to give the field $E(x, y, \omega, z)$ which is the field after the beam has propagated a distance z from the lens. This is illustrated in Fig. 6.1a.

It might seem that we should just tell our computer to evaluate Eq. 7.2 and then be done. But unfortunately the phase introduced by the lens (the phase of $\Theta(x_1, y_1, \omega)$) oscillates very quickly for high NA lenes and it often takes 20,000 or more sampling points to model Eq. 7.2 [101] which will take all day to run in MATLAB. So we would like to use a different approach.

One trick involves parameterizing the field just after the lens using a reference sphere rather than a reference plane. The reference sphere is centered on the focus and its radius is equal to the focal length of the lenses [102]. This geometry is shown in Fig. 6.1b. We will refer to the coordinates on the reference sphere as p_x and p_y.

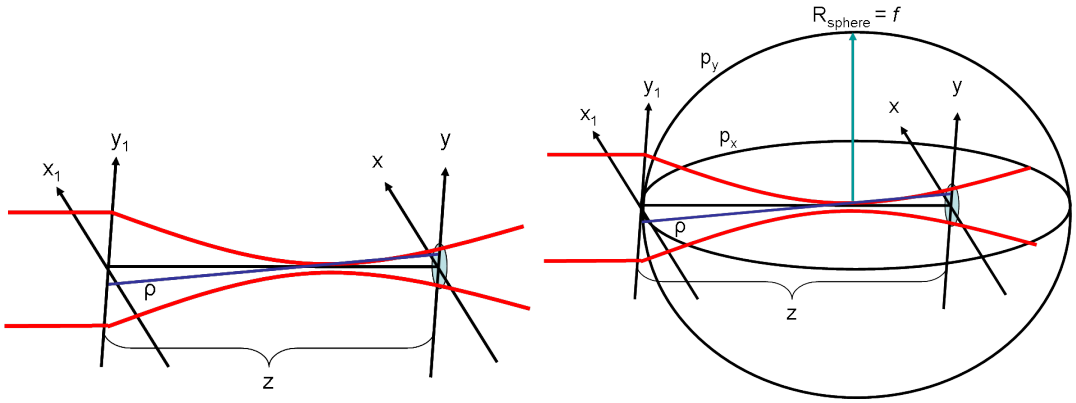

(a) Reference plane (b) Reference sphere

Figure 6.1: Two different approaches to solving Kirchhoff's integral for a focusing beam

The next step is to the write an expression for the field at the focus ($z = r$), where ρ and $E(x, y, \omega, z)$, and $\Theta(x, y, \omega, z)$ are written in terms of p_x and p_y. Equation 6.3 shows the new expression for ρ.

$$\rho = f\Big[1 + \frac{x^2 - 2p_x x}{f^2} + \frac{y^2 - 2p_y y}{f^2}\Big]^{1/2} \approx f\Big[1 + \frac{2p_x x}{f^2} + \frac{p_y y}{f^2}\Big] \tag{6.3}$$

The approximation used for ρ above assumes that the angle between the radius of the sphere and ρ is small, which is the case regardless of the NA.[1] Using this value of expression of ρ, the field of the pulse at the focus reduces to the Fourier transform shown below which was taken from [101].

$$\begin{aligned} &E(x, y, \omega, f) \propto \\ &\exp\Big[\frac{ik(x^2 + y^2)^{1/2}}{2f}\Big] \times \mathscr{F}(E(p_x, p_y, \omega, z = 0) \times \Theta(p_x, p_y, \omega, z = 0)) \end{aligned} \tag{6.4}$$

To find the field of the pulse near the focus, Eq. 6.4, can be propagated to another plane using what is know as the "angular spectrum of plane waves" and is described in detail in [80]. This approach uses the fact that Kirchhoff's integral can be expressed as a convolution and therefore if it is fourier transformed it becomes a product of the initial field with a kernel given by the following equation.

$$P_s(k_x, k_y) = \exp\Big[ikz\sqrt{1 - \Big(\frac{2\pi c}{\omega}\Big)(k_x^2 + k_y^2)}\Big]^2 \tag{6.5}$$

where $k_{x,y} = -\frac{\omega}{2\pi f} p_{x,y}$. Then the field at some distance from the focus δz reduces to a very simple Fourier transform which is show below.

$$E(x, y, \omega, f) \propto \mathscr{F}\Big[(E(p_x, p_y, \omega, z = 0) \times P_s)\Big] \tag{6.6}$$

The final step is to change from rectangular to cylindrical coordinates because we will continue to use lenses and beams with cylindrical symmetry and this will allow us to reduce the number of variables in the integral by 2. Note that, a cylindrically

[1]The approximation that is used in the Fresnel integral assumes that the angle between the z axis and ρ is small, and this is only true for lower NA foci

symmetric two-dimensional Fourier transform reduces to a Hankel transform [103], so the Fourier transform in 6.6 becomes a Hankel transform after changing it to cylindrical coordinates and integrating out θ (the polar angle). The final expression that we will evaluate is shown below.

$$E(r,\omega,z) \propto \int_0^\infty dp_r p_r J_0(p_r r k_0/f_0) E(p_r,\omega,0) P_s(k_r) P(p_r) \exp\Big(i\varphi(p_r,\omega)\Big). \quad (6.7)$$

In the above equation $p_r = \sqrt{p_x^2 + p_y^2}$, $k_r = \sqrt{k_x^2 + k_y^2}$, J_0 a bessel function of the first kind of order 0, P_s is the lens's aperture function and $\varphi(p_r,\omega)$ is the phase due to the lens' aberrations. The expression for $\varphi(p_r,\omega)$ is given by 5.4 from chapter 5 (just substitute p_r for r).

The advantage to using the reference sphere is that the spherical part of the phase introduced by the lens can be left out when writing the initial field as $E(p_x,p_y,\omega,z)$ so that it requires a lot less sampling points [2]. Using the spherical coordinate system the field just after the lens will only have a phase which is that due to the aberrations shown in Eq. 5.4. The quadratic term ($r^2k/2f$) due to focusing can be left out, because with respect to the spherical reference frame, this term is a constant. To write the spatial amplitude of $E(p_x,p_y,\omega,z)$, we just have to coordinates from r to p_r which can be done using $p_r = fo(tan(\frac{r}{fo}))$ where $r = \sqrt{x_1^2 + y_1^2}$. Just as we did for all of our simulations in chapter 5, for the simulations in this chapter we take the pulse just before the lens to have Gaussian spectrum and spatial intensity and use the experimental parameters for the bandwidth and the spot size. To calculate the phase due to aberrations (φ) we use the formulas in Eqs. 5.4, 5.6, and 5.7.

Note that the Kirchhoff integral is still a scalar approximation to Maxwell's Equations, and therefore it does break down at some point because it ignores the fact that there are many different polarizations (or k-vectors) present in a tightly focusing

[2] If you compare the paraxial diffraction integral that we used in chapter 5 to the non-paraxial one derived above you will see that this there is the difference

beam. In reference [100], it was experimentally demonstrated that polarization effects become important (meaning that Kirchhoff's integral breaks down) at numerical apertures that are around 0.8 and higher.

Appendix D shows a comparison of the paraxial (Eq. 6.7) to the non-paraxial diffractions integrals at several different numerical apertures to illustrate when they give the same results and when they give different results.

6.2 Experimental setup

The experimental setup that we use for the measurements shown in this chapter, is the same as what we used in for scanning SEA TADPOLE before (show in 5.4) except that we have replaced the single mode optical fiber with an NSOM fiber probe as shown in the figure below. The NSOM fiber probe for sampling the focusing pulse

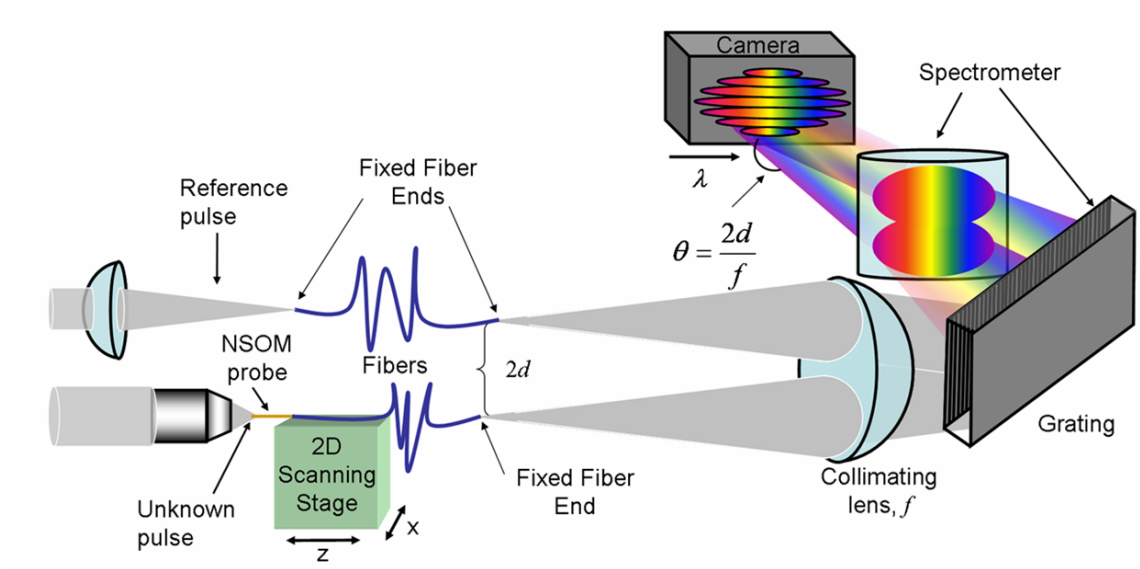

Figure 6.2: Experimental set for scanning SEA TADPOLE with an NSOM fiber probe

is a single mode fiber that is identical (it is the same type of fiber and it has the same length) to the fiber that is used for sampling the reference pulse except that it has an NSOM probe at its sampling end. And everything else, including the measured interferogram and the method of reconstructing $E_{unk}(\omega)$ is identical to what we used

before for scanning SEA TADPOLE as you can see from 6.2. And also, as we did in before, to measure the spatiotemporal electric field of the focusing ultrashort pulse $E_{unk}(x, y, z, \omega)$, we mount the NSOM probe end of the fiber to an x-y-z scanning stage as illustrated in Fig.6.2. To determine $E_{unk}(x, y, z, t)$, we just Fourier transform $E_{unk}(x, y, z, \omega)$.

The NSOM fiber probes that we use were purchased from Nanonics. These are made by tapering one end of a single mode fiber (the fiber is the same kind of fiber that we use in the reference arm). The end of the taper is coated using chromium and gold and a small aperture or hole is left uncoated. In our experiments so far, we have used probes with aperture diameters of 500 nm and 1 μm because these were sufficient to measure the pulses that we were interested in. Though in principle, even the smallest aperture NSOM probes could be used in SEA TADPOLE to achieve even higher spatial resolution.

Recall that SEA TADPOLE, like all linear interferometers, measures the spectral phase difference between the two arms of the interferometer. The phase of the reference pulse can be removed from this difference to isolate the phase of the unknown pulse. Or if one is interested in the phase introduced by some element that is in the unknown arm of the interferometer, then the phase difference will provide this. In this chapter, just as in chapters 2 and 5, we desire the spectral phase introduced by a lens (at every position within the focus), so, from each interferogram, we retrieve the spectral-phase difference between the two arms of the interferometer.

6.3 Measuring the transfer function of NSOM probes

As discussed previously in section, when sampling a focusing beam, the aperture diameter must be smaller than the focused spot size. This simultaneously provides sufficient spatial resolution and acceptance angle. Thus, a small enough NSOM probe will accurately spatially resolve the focusing pulse and collect all of the k-vectors from

the focus.

Because NSOM fiber probes are difficult to manufacture and easy to damage, it is important to characterize the probe (that is, measure its transfer function) before making any measurements to assure that the probe will not introduce artifacts in the measurement, and this characterization can be done is several different ways (for example see [98, 99]).

Here we make the measurement (just as we did in section 6.3 for the single mode fibers) by sending a collimated Gaussian beam into the small probe end and measuring the transmitted intensity as a function of the angle that the probe's axis makes with the beam's axis [89]. Because the Gaussian beam is 1000 times or more larger than the probe diameter, it is essentially a plane wave and, therefore, any change in intensity with angle, is due to the NSOM tip transfer function. We only measured the one-dimensional transfer function and so only rotated the probe in the plane of the table. This was sufficient for our measurements (see section 6.4) of focusing pulses due to the rotational symmetry present

Figure 6.3 shows the results of this measurement for two different NSOM fiber probes. The image on the right shows the transfer function for a 1μm probe that has

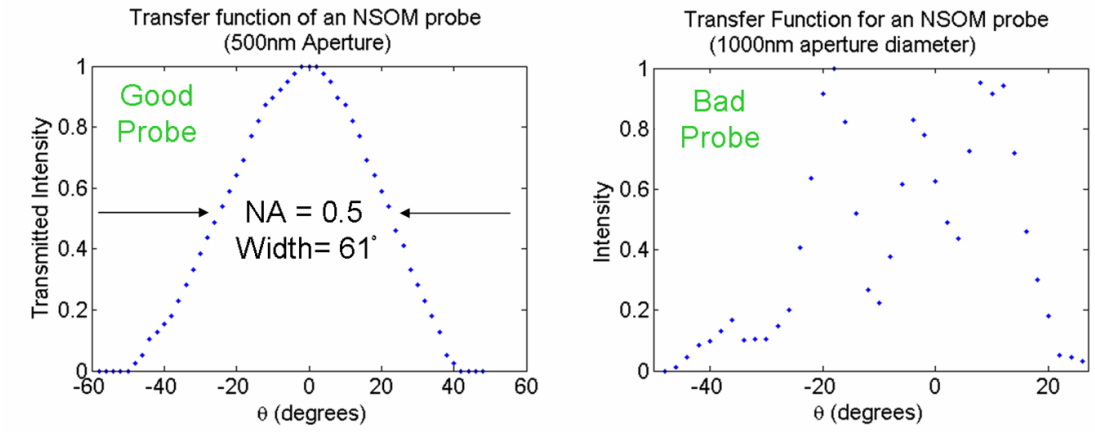

Figure 6.3: Measurement of the transfer function of two NSOM probes

a very complicated transfer function. This probe would angularly filter the focusing

pulse in a complicated way and is therefore not suitable for our measurements. This probe was likely bumped and damaged. The measurement on the left shows a much smoother and broader transfer function. As we have discussed in section 6.3, provided that the NA of the focused beam is less than the NA of the sampling NSOM fiber probe (which we took to be the sine of the half width at e^{-2} of the maximum of the transfer function), the probe will collect essentially all of the k-vectors of the light at the given point in space and therefore will sample the beam reasonably well. Therefore, using this probe we can measure foci with numerical apertures less than 0.5. The transfer function shown on the left was smoothed using a window size of 3 points to remove measurement noise.

Because this is an intensity measurement, it will not tell us if the transfer function is complex (has variations in its imaginary component), which would correspond to a variation in the phase of the light collected as a function of angle. A badly distorted probe (such as the one shown on the right of Fig, 6.3), which is not perfectly opaque outside of the aperture, could have a complex-valued transfer function. But as long as the NSOM probe really is an aperture, then its transfer function should be purely real. The measured transfer function for the 500-nm aperture indicates that this NSOM probe is not distorted, and therefore it is safe to assume that its transfer function is, not only smooth and broad, but also real. Our results corroborate this conclusion (see section 6.4).

Another potential source of error in our measurements is spectral filtering of the collected light by the NSOM probe (the probe could, in principle, collect some colors more efficiently than others), but we made spectral transmission measurements, as well, and confirmed that ours did not. Previous papers have also reported that NSOM probes do not change the spectrum as long as the power is low enough to avoid nonlinear effects, which it is here [104, 105].

6.4 Experimental results

Using the 500-nm-aperture diameter NSOM fiber probe that we characterized (shown on the left in Fig.6.3) above, we measured the spatiotemporal field of foci from several different lenses in order to test our method.

In all of these measurements, we used our KM Labs Ti:Sa oscillator, which had a bandwidth of 20 nm (FWHM) or 50 nm for the X-pulse measurement, and we never introduced more than 10 mW into the NSOM probe (as suggested by Nanonics) to avoid damaging it. As explained in section 2.3.1, because we measure the phase introduced by the lens, any spectral phase that the input pulse has, cancels in the measurement and the pulse that we measure is effectively transform limited before the lens (47fs, or 19fs). The temporal resolution in our measurement is given by the inverse of the spectral range of the spectrometer and this was 12fs, though we generally zero fill the spectral electric field before Fourier transforming to the time domain using around 1000 zeros to smooth out the measured temporal intensities. The beam and all of the lenses that we used had rotational symmetry, so measuring $E(x, z, t)$ was sufficient to test our method, and we only measured $E(x, z, t)$, although we can also easily scan in y in the future if necessary. To scan the NSOM probe, we used motorized actuators, which had a minimum step size of 200 nm or better. All other experimental details for SEA TADPOLE can be found in sections 2.3.1 or 5.2.

6.4.1 Microscope objectives

As our first experimental test, we focused the beam using two different aberration corrected microscope objectives and measured $E(x, z, t)$ at and around the focus (or the point where the beam had its smallest spot size). Because the parameters for these objectives are proprietary, we could not perform simulations to verify these results. But, even though these objectives are designed for the visible, they have significantly less aberrations than singlet lenses and instead have significant group delay dispersion

(GDD) due to the large amount of glass in their multiple elements [15]. Therefore we made these measurements to verify that the focus from the microscope objectives that we measured showed a relatively smooth, small, and flat pulse front (as determined by previous simulation [15]), which would indicate that the NSOM probe was accurately sampling the focusing beam. The pulse fronts for this measurement (and for the 20x objective) are flat because the measurements were made so close to the focus.

The first objective that we used was a 10x (f = 16.5 mm, clear aperture diameter = 7.5 mm, and NA=0.25) microscope objective, and Fig. 6.4 shows the results of this measurement. Each box in Fig. 6.4 shows the pulse's amplitude as function of t and

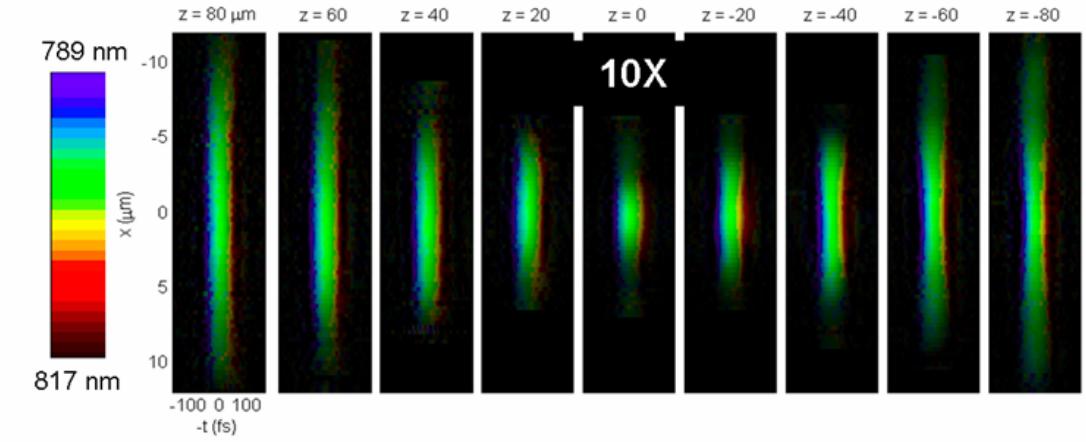

Figure 6.4: Measured spatiotemporal field of a pulse focused with a 10X microscope objective

x (the transverse position) at a certain distance from the focus (or the point where then beams spot size was the smallest). The color in the plot shows the instantaneous frequency of the pulse as indicated by the color bar.

The main distortion seen in the focus is that the redder colors precede the bluer colors, or that the pulse is chirped, as expected from the GDD introduced by the multi-element, aberration-corrected refractive lens. Interestingly, the center part of the beam is more chirped than the sides-due to the radially varying GDD-which is also expected considering that the center of the objective contains more glass than

the sides (especially apparent at z = -40 and -20). Other than these two distortions, the pulse front is fairly smooth, as expected. The spot size of the intensity averaged over time at the focus of this objective has a FWHM of 3μm.

We measured the focus of a similar, but higher NA, objective (20x, f = 9 mm, clear aperture diameter = 6 mm, and NA=0.4), and the results of this measurements are shown in Fig. 6.5. As with the 10x objective, the main distortion seen in the

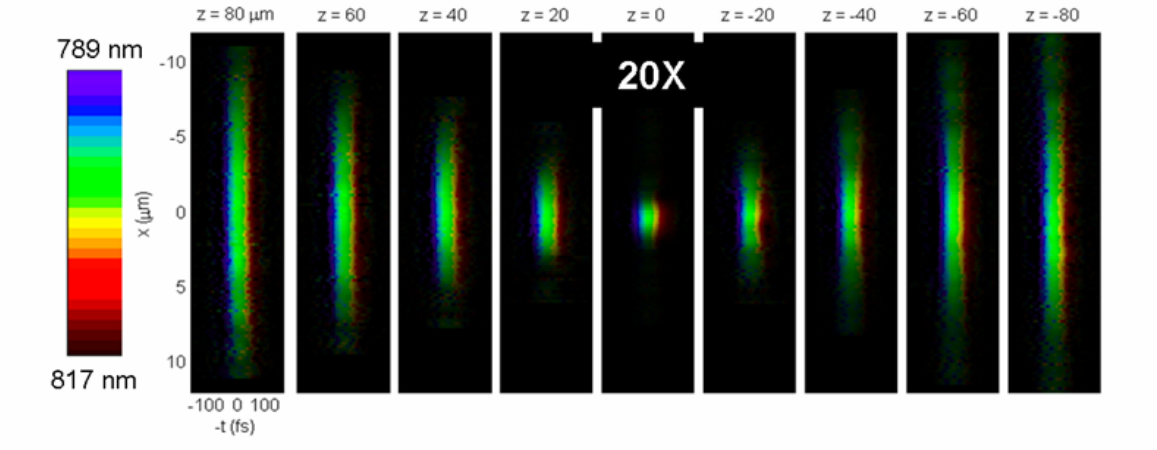

Figure 6.5: Measured spatiotemporal field of a pulse focused with a 20X microscope objective

focused pulse is chirp. The pulse from this objective looks more chirped than that from the 10x objective which is expected considering that a higher NA objective probably contains more glass. Also, the focused spot of the intensity averaged over t had a FWHM of 1.8 μm.

In both of the above measurements, we focused the 1mm beam directly out of the oscillator, which we routinely monitor using a Swamp Optics GRENOUILLE, which shows it to be free of pulse-front tilt and spatial chirp. As in previous chapters (chapters 5 and 2) and publications [51, 55], our measurements confirm that this beam was also free of other spatiotemporal distortions. Were this not the case, then our SEA TADPOLE measurements would show these distortions as well as those introduced by the lens.

Finally, because the beam was much smaller than the clear aperture of the objectives, no edge diffraction effects are seen in these measurements.

6.4.2 Singlet lenses

For the next two measurements, we used a telescope to increase the beam's spot size by a factor of four, yielding a FWHM of 4 mm at the focusing lens. To ensure that minimal aberrations were introduced by the telescope we put a 25 μm pinhole at the focus of the telescope to spatially filter the beam. This filter also removed any spatiotemporal distortions that may have been present before the telescope. The telescope consisted of two plano-convex lenses with focal lengths of 100 mm (25 mm diameter) and 400 mm (50 mm diameter). The spatial filter did not remove any aberrations introduced by the second lens (the 400 mm focal length lens), but because this lens has such a low NA, its aberrations are negligible.

To test our measurements, we also numerically propagated the fields through these lenses using all of the experimental parameters and the method that is described in section 6.1.2.

We measured $E_{unk}(x, z, t)$ for a pulse focused using an SF11 plano-convex lens, with a diameter of 12 mm and a focal length of 12 mm. The NA of this focus was 0.28 (using the standard definition for Gaussian beams, which is the radius of beam at e^{-2} of its peak intensity, divided by the focal length). Figure 6.6 shows the results of this measurement at the top, and the results of the simulations are shown at the bottom. The results shown in Fig. 6.6 show good agreement between the simulation and the experiment. In these plots, $z = 0$ is defined as the geometric focus, which we find using the simulations. Because of the material dispersion introduced by the lens, the redder colors precede bluer colors. The ripples that are seen before the focus are due to the large spherical aberrations. The smallest of these ripples has a width of 1μm (looking at the FWHM of a ripple in the intensity versus x at one t), which

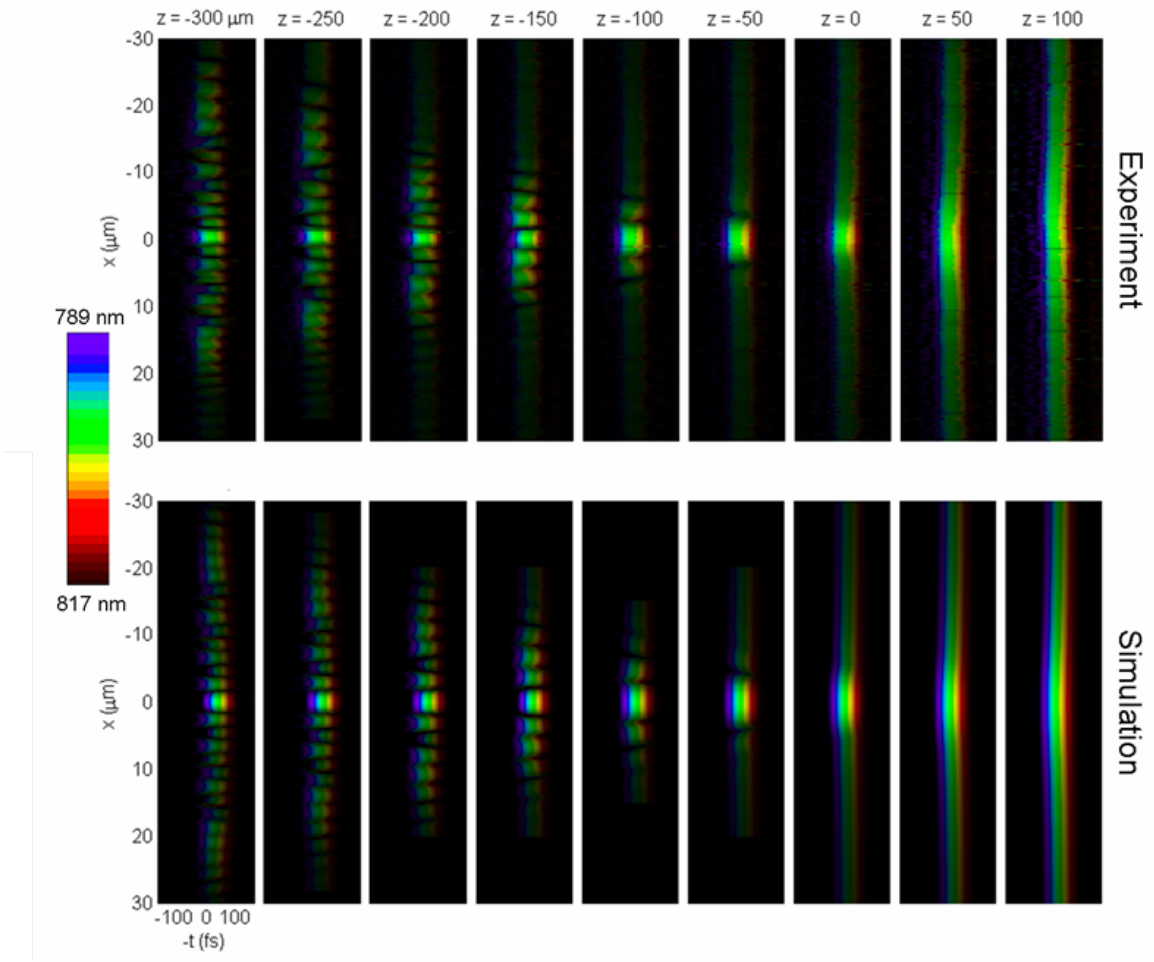

Figure 6.6: Measured spatiotemporal field of a pulse focused with a 0.28 NA SF11 lens

illustrates our high spatial resolution.

We also made two measurements of a pulse focused with similar plano-convex lenses for the purpose of observing the Bessel-like X-shaped pulse that occurs before the geometric focus due to spherical aberrations [81]. In the first of these measurements we used a lens made of BK7 with a focal length of 15 mm and a diameter of 12 mm. This BK7 lens has about the same amount of spherical aberration as the SF11 lens shown above, but much less GDD (by a factor of ~ 3), which makes it easier to observe this distortion. We also increased the bandwidth of our laser to 50 nm (FWHM) when making this measurement.

Figure 6.7 shows the results of the simulation and the measurement for this focus. For these results we plotted $|E(x, z, t)|$ (the amplitude as opposed to the intensity)

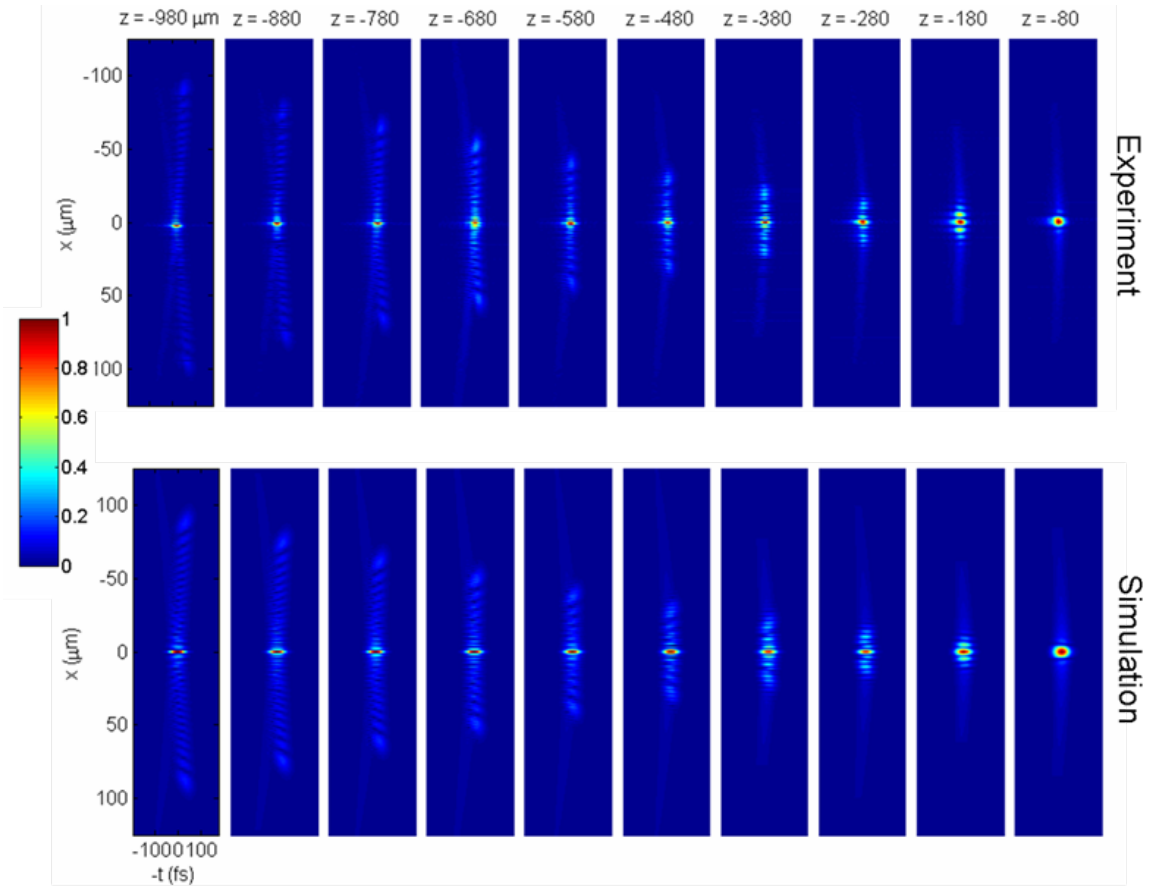

Figure 6.7: Measured spatiotemporal field of a bessel-like pulse

of the focusing pulse and not the phase so that the shape of the pulse could be more easily seen. The color in these plots represents the normalized intensity as indicated by the color bar. The phase of this pulse simply showed that there was positive GDD and we found good agreement between the simulations and the measurements for this.

The measurements and the simulations shown in Fig. 6.7 for the intensity are in good agreement; both show the presence of a Bessel-like pulse between 0.9 and 0.5 mm before the geometric focus. As reported in a previous theoretical paper, extreme spherical aberrations result in a Bessel-like pulse (characterized by the "X-shape") between the marginal (z=-3mm) and the paraxial focus (z = 0) [15, 81]. As far as 0.9mm away (and all the way to the marginal focus) from the geometric focus, most of the pulse's energy is confined within a 1μm spot size. It is also interesting to note that the "X-shaped" part of the pulse travels faster than the main pulse front and therefore faster than the speed of light which is allowed because this intensity pattern is due to interference and does not carry any energy [15]. The difference between this pulse and a real Bessel pulse is that its spatiotemporal shape and its speed of propagation do change as it propagates and in this case, the Bessel-like pulse only exists between the paraxial and the marginal foci [15].

The next set of measurements shows an even better measurement of the bessel-like "X pulse" (see Fig. 6.8). For these measurements we used a BK7 plano-convex lens with a focal length of 6mm and an aperture diameter of about 6mm. Again, considering the beam's spot size just before the lens, this focus had a numerical aperture around 0.25. Much like the the data shown in Fig. 6.7, as far as 1.3mm away (and all the way to the marginal focus) from the geometric focus, most of the pulses energy is confined within a 1-μm spot size. In this measurement, we were able to observe the "X pulse" at a point when it does not overlap with the main pulse front, which we could have observed with the in the previous set of measurements if

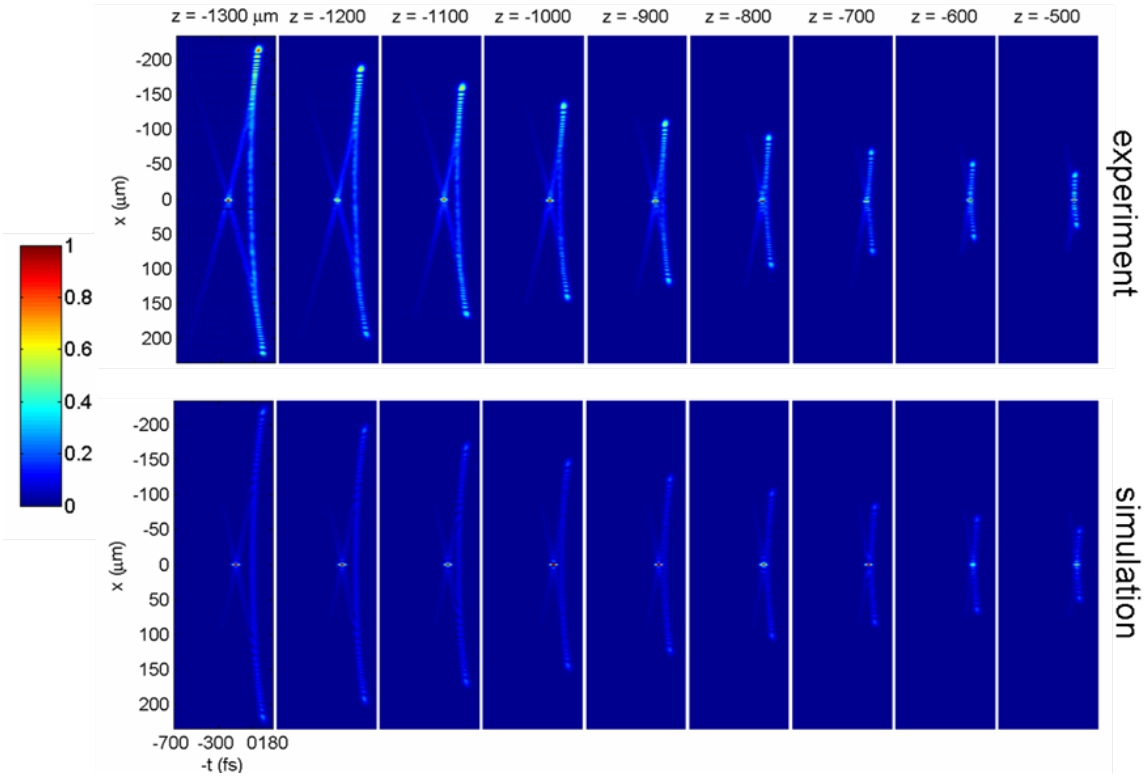

Figure 6.8: Measured spatiotemporal field of a bessel-like pulse

we had looked made measurements at larger z's. And, again, it is apparent that the "X-shaped" part of the pulse travels faster than the main pulse front and therefore faster than the speed of light.

To better observe this pulse as it propagates, we made a movie out of the data shown above by streaming together the 30 measurements, and interpolating so that there are around 200 frames. This movie is shown from the prospective of walking along with the pulse at the speed of light as it focuses.

(movies/xpulse-lens.avi)

Figure 6.9: (Click on the above picture to start the movie) $|E(x,t)|$ where each frame is a different z.

The final measurement that we made was of the focus produced by a New Focus aspheric lens made of CO550 glass with a focal length of 8 mm, an aperture diameter of 8 mm; the focus had an NA of 0.44. To determine the aberrations in this lens for the simulations, we performed ray tracing using OSLO [106] and used the lens parameters provided by New Focus. Because this lens is designed to be used with a

glass cover slip, which we did not use in our experiment, some spherical aberrations are present. Figure 6.10 shows the results of the measurement. Again, the results of

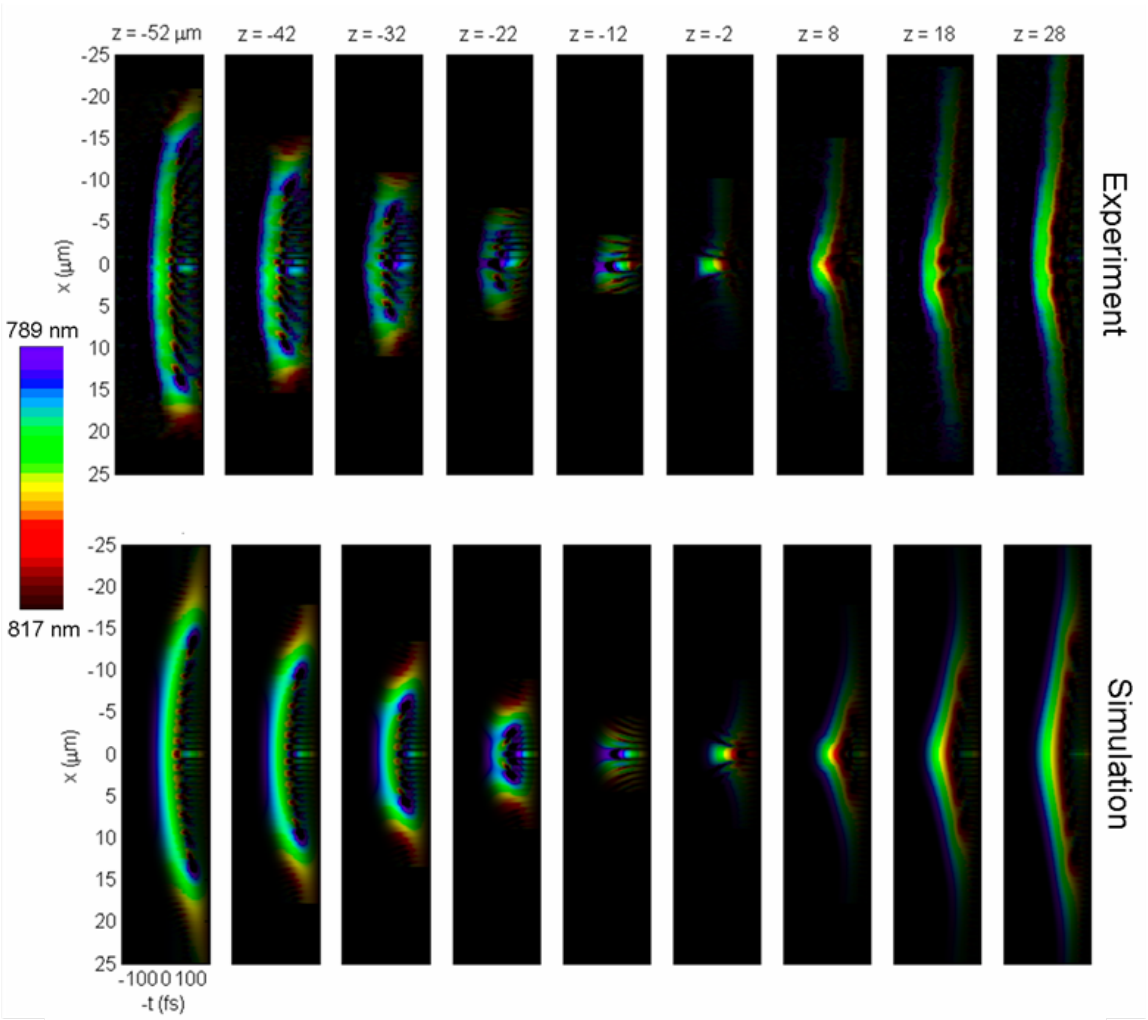

Figure 6.10: Measured spatiotemporal field of a 0.44 NA asphere

the simulation and the experiment are in good agreement. The color varies with time due to GDD and also with the transverse position x due to chromatic aberrations. Also the redder colors focus later than the bluer colors, so before the focus the blue is at the center and the red is on the edges of the pulse.

The most striking feature in this data is the presence of the additional pulse, the so called "fore-runner pulse" than can be seen before the focus. This additional pulse results from the combination of diffraction at the edge of the lens and chromatic

aberration [15, 81]. The "fore-runner pulse", like the "X-shaped" pulse, travels faster than the main pulse front meaning that it is traveling faster than the speed of light. Again, because this additional pulse is the result of interference, it does not carry any energy, so this does not violate the theory of relativity [81]. The FWHM of the intensity of the additional pulse is less than 1μm. The small amount of spherical aberration present in this focus increases the intensity of the additional pulse.

Due to chromatic aberration, the color of the pulse also changes as it propagates. To better visualize this, we made a movie of this pulse focusing by streaming together 21 measurements and using interpolation to generate 150 frames. The movie is shown in Fig. 6.11 Note that the center of the pulse color at its center changes from blue to

(movies/asphere.avi)

Figure 6.11: (Click on the above picture to start the movie) $E(x,t)$ where each frame is a different z.

green and then red as it propagates, because different colors are focusing at different values of z.

6.5 Other issues and comments

Each time that we moved the NSOM probe to a different z, we also adjusted the path length of the reference pulse so that there would always be zero delay between the two pulses. But in our measurements (which are automated), the adjustment did not always work perfectly, and the delay between the focusing pulse and the reference pulse was not zero for every value of z. At most it was off by ∼100 fs. Because of the agreement between the simulations and the measurements, we believe that the location of the NSOM probe with respect to the focus (or the z value) is still correct (or very close), and that the varying delay was due to a drift in the reference arm of the interferometer or the inaccuracy of the stage that moves the reference pulse. Using the simulation as a reference, we recentered each $E(x,t)$ on the time axis to the appropriate place. In the future, using better translation stages or adjusting the delay to be zero within our program, we should be able to fix this problem. We only had to make this adjustment for the aspheric lens data where we used a smaller step size in z than in any of the other measurements. In all of our measurements, measuring $E(x,t)$ at one z typically took about 1 min, so the measurements in Figs. 6.6-6.8 each required $\sim$ 9 minutes, and the data for the movie required $\sim$ 20 minutes to collect. Measuring the X-pulse required taking $\sim$ 10 times as many points due to the small features present in the pulse's large wings, so the data shown in Fig. 6.10 required $\sim$ 2 hours.

Just as in scanning SEA TADPOLE with fibers, as explained in chapter 5, because we have not perfectly stabilized our interferometer, it experiences a slow phase drift that only affects the spatial phase so that we do not measure it well. To illustrate this, appendix B shows the measured spatial phase information from the measurement using the SF11 lens shown in Fig. 6.6.

6.6 Conclusions

We demonstrated a method for measuring the spatiotemporal electric field of focusing ultrashort pulses with sub-micron spatial resolution, femtosecond time resolution, and high spectral resolution. We made these measurements using SEA TADPOLE with an NSOM fiber probe to spatially resolve the focusing pulse. We make multiple measurements of $E(x,t)$ at many positions throughout the focus by scanning the NSOM probe longitudinally and transversely in order to measure $E(x,z,t)$.

Before making any measurements, we measured the transfer function of several NSOM probes in order to find one that had a high enough numerical aperture and a smooth transfer function so that it would accurately indicate the focusing pulse at the point of interest. Then using this NSOM probe (the 500-nm diameter one shown in Fig. 6.3), we tested our technique by measuring the foci produced by two different microscope objectives. The primary distortion we saw in these foci was chirp as expected and we observed some radially varying GDD in these measurements.

We also measured $E(x,t)$ at and near the foci produced by two different plano-convex lenses (NA = 0.28, and 0.23) and an aspheric lens (NA = 0.44). To verify these measurements, we simulated these foci and found good agreement between the simulations and measurements. With the NA = 0.23 plano-convex lens, we observed the X-shaped Bessel-like pulse due to its spherical aberrations. From the measurement of the focus of the aspheric lens, we made a movie of the pulse focusing. In these measurements, we were able to spatially resolve features in the intensity smaller than 1 μm, and we observed the "fore-runner pulse"-the additional pulse that appears ahead of the main pulse before the focus, due to chromatic aberrations and overfilling the lens. To our knowledge, these are the first measurements of the spatiotemporal field of the Bessel-like due to spherical aberrations and the "fore-runner pulse".

The agreement between our measurements and simulations also verifies the validity of the non-paraxial simulations that we use for calculating the spatiotemporal field

of focused ultrashort pulses which can be a very useful tool.

In the future using NSOM probes with even smaller apertures, we hope to measure even more tightly focused pulses such as those from the high NA objectives that are routinely used in microscopy.

CHAPTER VII

MEASURING THE SPATIOTEMPORAL FIELD OF ULTRASHORT BESSEL X PULSES

7.1 Introduction

Due to diffraction, the spot size of a laser beam changes as it propagates, and smaller beams tend to diffract after less propagation than larger beams. The distance over which a Gaussian beam can propagate without significantly changing size, or the so-called "collimated range" is given by $\frac{2\pi w_0^2}{\lambda}$ where w_0 is the waist size of the beam [79].[1] This means that a tightly focused Gaussian beam only stays small over a short propagation distance. For example, a Gaussian beam that has been focused down to a size of 1μm starts to significantly diverge after propagating only 8μm away from the focus. This is unfortunate because high intensities are needed for many applications of lasers, and the focus, or the point with the highest intensity only lasts for a short distance, limiting the interaction lengths in nonlinear optics and lasers for example.

In mathematical terms, given the electric field at an initial plane (y_1, x_1, z_1), the field at another plane (y_2, x_2, z_2) that is some propagation distance away, can be calculated by evaluating the kirchhoff diffraction integral which is shown below.

$$E(x_2, y_2, \omega, z_2) \propto \int_{-\infty}^{\infty} dx_1 \int_{-\infty}^{\infty} dy_1 E(x_1, y_1, \omega, 0) \frac{\exp(ik\rho)}{r^2} z \tag{7.1}$$

$$\rho = \sqrt{z^2 + (x_1 - x)^2 + (y_1 - y)^2} \tag{7.2}$$

To say that a beam diffracts, means that this integral changes the shape of the field. So, if there exists some field that is an Eigenfunction of the diffraction integral, then its shape would be unchanged by this integral and it could propagate for long distances

[1] The collimated rage is two times the Rayliegh range

without diffracting. It turns out that such solutions to the diffraction integral do exist and these are known as "localized" or "non-diffracting" waves [107]. These non-diffracting beams can be made using ultrashort pulses so that the field is localized in both space and time.

In this chapter we show our recent measurements of a specific type of non-diffracting field known as a Bessel beam. We use our ultrafast laser along with the Bessel beam generator to make time-localized Bessel beams which are known as Bessel X pulses. Besides being propagation invariant, Bessel X pulses also have the interesting property that they propagate superluminally along the z axis.

7.2 Bessel pulses

Bessel X pulses are of great interest because they propagate in vacuum or linear media over large distances like an optical bullet—without exhibiting any diffraction or spread in time [108]. Bessel pulses have many applications, such as filament or plasma generation, and they have even been used for cell transfection [109]. Bessel-X pulses are a rotationally symmetric localized wave (see [107, 108, 110, 111]) that is a broad band wave packet of Bessel beams. Their three dimensional intensity profile $I(x, y, z)$ consists of a bright spot in the center surrounded by weaker interference rings whose diameter increases with distance away from $t = 0$, so they look like two cones extending out in time from the origin. An $x - t$ or $x - z$ slice $I(x, t)$ or $I(x, z)$ of the pulse resembles the letter "X". The field of the Bessel X pulse propagates in the axial (z) direction with a superluminal (in vacuum greater than c) which is not in violation of Einstein's causality [111]. It is important to measure these pulses, not only to observe their interesting and useful properties, but also to aid in their generation and application. But Bessel-X pulses have a complex spatiotemporal shape, so a sophisticated spatiotemporal technique with high temporal and spatial resolution is needed to completely and accurately measurement them.

Using bessel pulses generated with a diffractive optical element known as a lensacon, the propagation invariance of the central spot of the beam was observed [108]. The X-like spatiotemporal shape and the superluminal propagation of the Bessel pulse was first demonstrated in [111], by measuring cross correlations. In another study, using an axicon (a conical lens) the propagation speed of a Bessel pulse was determined to be 1.1c. This measurement was made by ionizing argon gas with the X pulse [112]. But, to our knowledge, no one has ever made a direct, complete spatiotemporal measurement of the electric field of a Bessel X pulse.

Here we show direct measurements of "snapshots in flight", or spatiotemporal slices of the X-like profile of a femtosecond Bessel X pulse. Our results show propagation invariance over ≈ 7 cm as well as the superluminal velocity of the Bessel X pulse. To make these measurements we use scanning SEA TADPOLE which was described in detail in chapter 5.

7.3 Experimental results and numerical simulations

To generate the Bessel X pulse we used a fused silica axicon with an apex angle of 176 degrees and a KM Labs Ti:Sa oscillator with 40nm of bandwidth.(FWHM)[2] The spot size of the beam at the front surface of the axicon was 4mm (FWHM). The experimental setup that we used is shown in Fig. 5.4, where the lens in the unknown beam was replaced with the axicon. We placed the fiber at the vertical center of the bessel beam $y = 0$ and scanned in x to measure $E(\lambda, x)$ at several different values of z or propagation distances after the axicon. The fields were Fourier transformed to the time domain to give us $E(t, x, y = 0)$. Note that we could also scan the fiber along the y dimension to measure $E(\lambda, x, y)$, but our Bessel-X pulses were approximately symmetric about the z-axis, so this was not necessary. Our temporal resolution was

[2]An axicon is a rotationally symmetric prism, or it is shaped like a cone. Refraction of the beam at the tilted edge, causes it to cross with itself. This crossing region is where the Bessel beam occurs, and therefore, its speed, spot size and the distance over which it lasts all depend on the apex angle and material that the axicon is made of.

8.9fs, and we used zero-filling to decrease the point spacing to 4.6fs. As explained in sections 2.3.4 and 5.3, SEA TADPOLE measures the spectral phase difference between the unknown and the reference pulse and for these measurements we placed extra glass in the reference arm to cancel out the group delay dispersion (GDD) introduced by the center thickness of the material in the axicon. Therefore the field that we measure reflects the spatiotemporal phase introduced by the axicon if a pulse compressor to compensate for the center thickness of the axicon had been used.

We measured $E(t, x)$ at several different values of z or axial distances from the front surface of the axicon by translating it along the beam's propagation direction, and three of these measurements are shown in Fig. 7.1 [3]. We also performed numerical

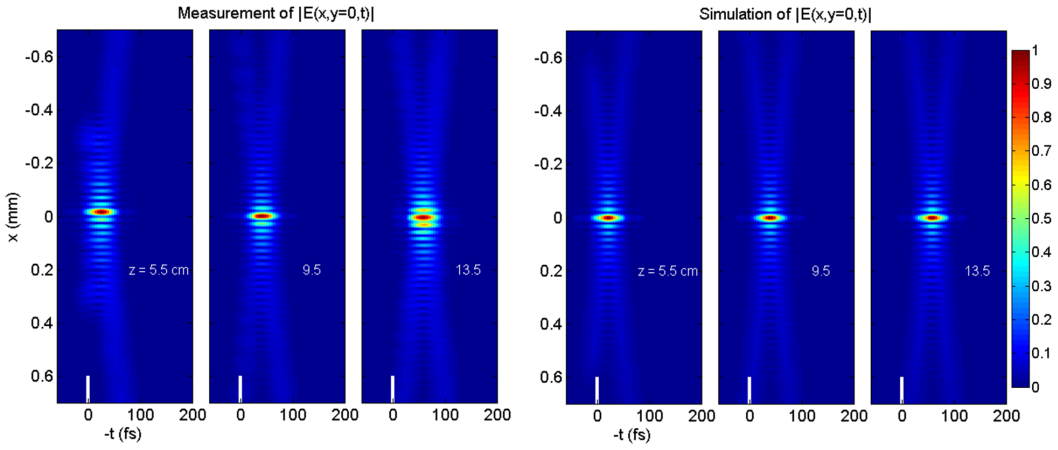

Figure 7.1: Measurement (left) and simulations (right) of a Bessel pulse

simulations of the expected field using all of the experimental parameters, and these results are shown on the right in Fig. 7.1. The two are in good agreement except that the wings in the z=5.5cm image are shorter in the measurement. This is because axicons are difficult to machine perfectly and the tip of the cones are always distorted. Though we have tried to account for this in our simulations, it is difficult to model

[3] In Chapters 5 and 6 we moved the fiber to measure the field at different propagation distances, and then also moved the reference fiber by the same amount to keep the pulses temporally overlapping. But here we instead moved the axicon closer or further away from the fiber so that the reference beam path would not have to be changed.

perfectly, or to know the exact shape of the axicon. SEA TADPOLE also measures the spatiotemporal phase, but because we compensated for the glass in the axicon, this phase is transform limited, or the color of the pulse is the same everywhere in x and t. So here we only show the amplitude.

There are several interesting features in this data. The central maximum of the pulse has a width of ≈ 20 μ m, which remains essentially unchanged in shape from z = 5cm through z = 13.5cm, and in our measurement at z = 13.5, the interference pattern is just beginning to change due to the axicon aberrations/imperfections.

Also, the Bessel X-pulse's superluminal speed is apparent in these plots. SEA TADPOLE measures the pulse's arrival time with respect to the reference pulse which is just a simple Gaussian (it is the pulse directly out of our laser) that travels at the speed of light (c). Therefore if the Bessel X pulse were traveling at the speed of light then at each z its spatiotemporal intensity would be centered at the same time (here t = 0 and emphasized with the white line), but it is easy to see that this is not the case. From our axicon's apex angle and from the simulations, we find that the Bessel X pulse's speed should be 1.00013c. Therefore, over a distance of 8cm, the Bessel X pulse would lead our moving reference frame (the reference pulse) by 35 fs. In our results, the center of the pulse is ahead in time by 32fs after propagating from z = 5.5cm to z = 13.5cm, which is in good agreement with our theoretical prediction. To verify this result, we repeated the experiment several times and consistently measured the time shifts predicted for this axicon. We also realigned the axicon in between these trials to assure that this delay was not due to (or significantly affected by) misalignment of the axicon's scanning stage.

7.4 Conclusions

In conclusion, using SEA TADPOLE, we have made the first (to our knowledge) direct spatiotemporal measurements of Bessel X pulses, and we verified these results

with simulations. We demonstrated both the propagation invariance of the Bessel X pulse and its superluminal axial group velocity which we determined to be around 1.00012c which is within 0.001% error of the expected value.

CHAPTER VIII

DIFFRACTION IN THE TIME DOMAIN

8.1 Introduction

Diffraction—or the change in a light field due to a boundary, or an obstruction—is a very old and well-known topic which dates back at least to Lenardo da Vinci [82]. Though the theory of diffraction has been around for a long time, the traditional methods of solving diffraction problems are still often difficult to use, and give unintuitive results.

In most textbook examples, diffraction is presented as a spatial effect that causes holes created by the obstruction to gradually get filled in as the beam propagates. But in general, diffraction usually happens anytime that a beam propagates and even when the propagates is through free space or in the absence of an obstruction, or optical element. The electric field after different propagation distances can be calculated using an appropriate version of the diffraction integral (see for example sections 6.1.2 and 5.1.2). While diffraction effects are easy to understand in the far field where they can be treated as a Fourier transform of the field just after the boundary, in the near field the diffraction pattern can be quite complicated.[1] Figure 8.1 shows two standard examples of near field diffraction intensity patterns for monochromatic light. Figure 8.1a shows the intensity as a function of x at different propagation distances after a circular aperture. The second example 8.1b, shows the diffraction of a Gaussian beam by a disk which makes a hole in the beam. This results in the exotic "spot of Arago", or the bright spot at the center of the hole that appears after the beam has

[1]Far field diffraction refers the case when the distance from the boundary z is at least several orders of magnitude greater than $\frac{\pi D^2}{\lambda}$ where D is the size of the boundary. Diffraction at distances smaller than this is referred to as near field diffraction

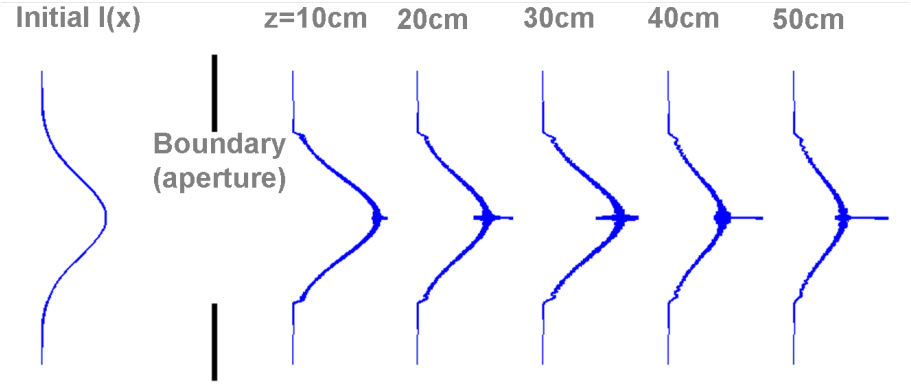

(a) Diffraction of a Gaussian beam off of an aperture

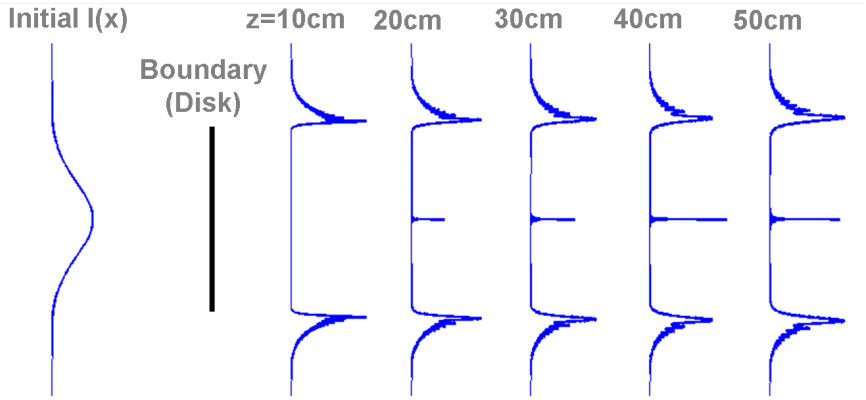

(b) Diffraction of a Gaussian beam off of a disk (the spot of Arago)

Figure 8.1: One-dimensional diffraction examples

propagated a few centimeters [82, 113]. Surprisingly, the hole fills in from the center first. Both of these examples are quite strange and difficult to explain other than by saying that this is what diffraction integral and Maxwell's equations tell us [2]. And of course, these very old results have been verified by many experiments.

In this chapter, we show the first measurements of diffracted light fields in the time domain. We use ultrashort pulses as the light source and SEA TADPOLE to measure the diffraction pattern in both space and time. As we will show, the diffraction effects experienced by ultrashort pulses—due to being well localized in both time and space—are different than those experienced by other light sources [114]. It turns out that for ultrashort pulses, diffraction effects are not just spatial, but spatiotemporal meaning the pulse is changed in both space and time. We will also attempt to explain our results using a simple and elegant, but somewhat forgotten theory of diffraction known as the boundary wave diffraction theory.

8.2 Boundary wave theory of diffraction

The idea of the boundary wave diffraction theory of light was intuitively conceived by Thomas Young, who thought that a diffracted field should be equal to a sum of two contributions: one wave that propagates unobstructed through the boundary and in accordance with geometric optics, and another wave due to the interference of spherical waves that are emitted all along the boundary, or the "boundary wave" [115]. While the more common formulation of diffraction using the Kirchhoff integral involves summing up spherical waves from every point (x, y) on the initial plane (including the area where there is no obstruction), Young's approach is simpler, and it turns out be equivalent. But nevertheless, his theory was temporally forgotten and finally rigorously formulated and proven to be consistent with the Kirchhoff

[2]The diffraction can be understood as summing up spherical waves that are emitted at every point (x, y) on the initial plane. But, even with this qualitative explanation of the integral, it is difficult to guess what the results will be.

diffraction integral over 100 years later by Maggi and Rubinowicz, and Wolf and coworkers [116, 117].

The idea of the boundary wave theory is especially useful for explaining some diffraction effects that have been observed with ultrashort pulses [114, 118]. Figure 8.2, shows the results of a simulation done by Horvath and coworkers that predicts the spatiotemporal field of an ultrashort pulse after propagating through a circular aperture. Figure 8.2a uses plane waves for the initial spatial dependence of the field

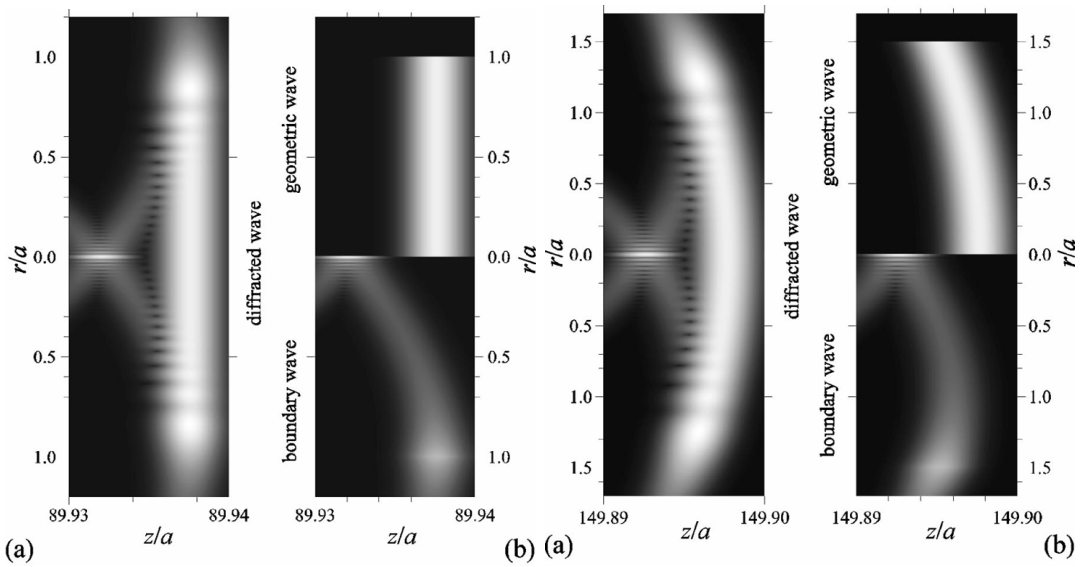

(a) A plane wave pulse (b) A diverging spherical wave pulse

Figure 8.2: Simulation of Diffraction of ultrashort pulses off of a circular aperture using the boundary wave diffraction integral (Image taken from ref [114])

and in Fig. 8.2b a divergent spherical wave is used. This figure illustrates that the resulting diffracted field is the sum of a geometric or an undiffracted wave (also called the main pulse front) and the boundary wave which was calculated by adding up spherical waves that were emitted all along the boundary.

Interestingly, the boundary waves shown in 8.2 are shaped like an "x" in space-time and behind the main pulse front in time with a delay that varies with r. A qualitative explanation of the propagation speed of the boundary wave along the z direction is shown in Fig. 8.3. Because the spherical waves that make up the boundary wave

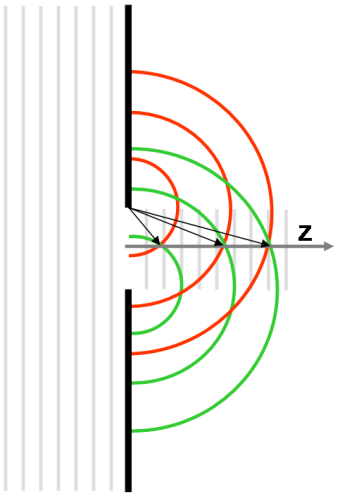

Figure 8.3: Illustration of the propagation speed of the boundary wave along the z axis. The arrows indicate the path length for the spherical waves that add up to make this wave. The Gray lines represent the plane waves that illuminate and propagate through the aperture.

originate at the boundary, the distance that they have to travel to get to a point on the z axis is longer than the distance that the main pulse front must travel to get to this point. Therefore the boundary wave arrives after the main pulse front as seen in Fig. 8.2. The black arrows in Fig. 8.3 show the propagation distance for the spherical waves to get to different points on the z axis, and you can see that this distance decreases with z and eventually becomes equal to the propagation distance of the main pulse front (the plane waves shown in gray). For values of r not equal to 0, the spherical waves from the same side of the aperture as the r vector, will arrive before the waves at $r = 0$ and the spherical waves from the other side of the aperture will arrive later, resulting in the "x" shape. Therefore we can predict that the bright spot at $r = 0$ will start out behind the main pulse front in time, but it will travel along the z axis with a superluminal speed and eventually catch up with the main pulse front.

8.3 *Measuring the spatiotemporal field of diffracted ultrashort pulses*

Using scanning SEA TADPOLE we measured the spatiotemporal field of ultrashort pulses after they were diffracted by different types of boundaries. The experimental setup that we used is shown in Fig. 8.4 and the SEA TADPOLE device that we used is the same as that described in chapter 5 for measuring lower NA focusing pulses. Note, that for simplicity we translated the boundary rather than scanning the fiber along the z axis.[3] To spatially sample the diffracted field, we used a single mode fiber with a core size around $5\mu m$. Figure 8.5 shows the three different boundaries that we

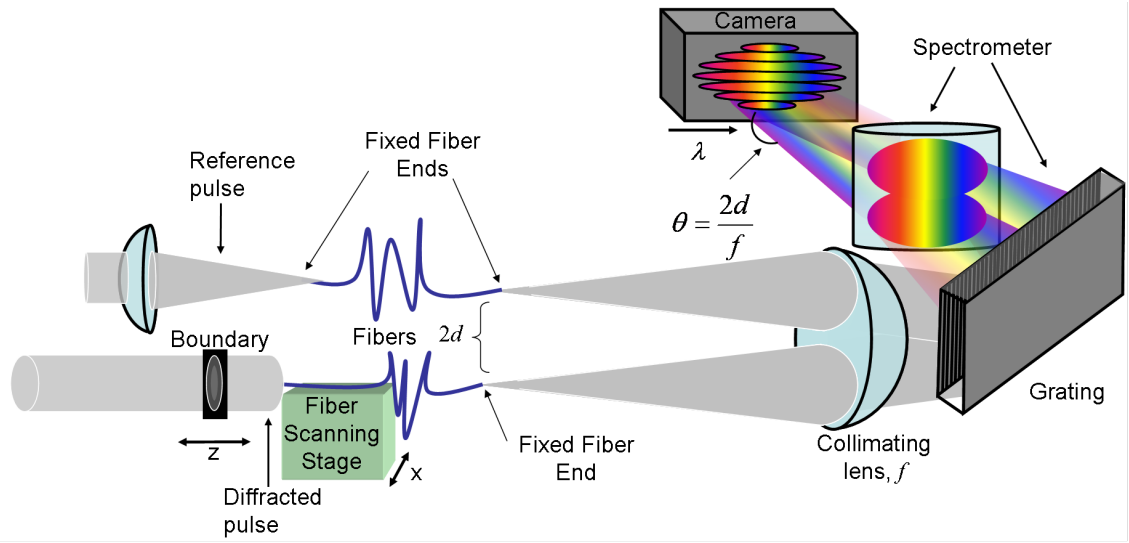

Figure 8.4: Experimental setup for measuring diffracted pulses with SEA TADPOLE

used to generate the diffraction. As the light source we used a mode-locked Ti:Sa laser with a center wavelength of 810nm, a bandwidth around 35nm and a pulse duration around 27fs. In all of the measurements shown here we used a Gaussian beam with a FWHM spot size of 4mm.

We also calculated the expected field after the aperture by numerically solving the

[3]For our measurements in the previous chapters, every time that we moved the reference fiber in the z direction we also adjusted the delay of the reference pulse to maintain temporal overlap.

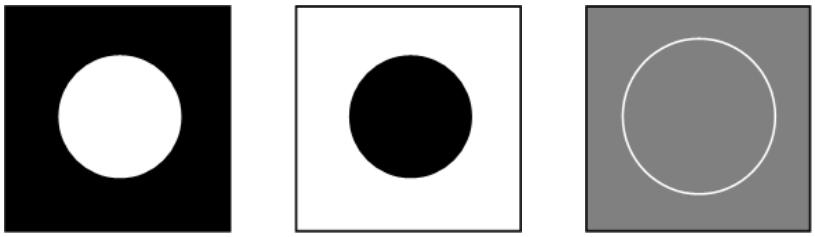

(a) Circular aperture (b) Circular disk (c) Leaky annular slit

Figure 8.5: Diffraction boundaries used for the measurements in this chapter

non-paraxial diffraction integral using the angular spectrum of plane waves approach and fast Hankel transforms as described in the following references [80, 119, 120]. Though we did not use the boundary wave theory for our simulations, this theory is still useful for interpreting our results and the two approaches for doing the calculations should give the same answer [116, 117].

In the first measurement we propagated the beam through a circular aperture (see Fig. 8.5a) with a 4.2mm diameter. Then we put the fiber at the center of the beam vertically (at $y = 0$) and scanned along the x dimension to measure $E(x, \omega)$ at different distances z from the aperture. The amplitude of the measured and simulated fields are shown in Fig. 8.6 where the color represents the intensity (red is 1 and dark blue is 0). As we expected, the boundary wave starts out behind the main pulse front in time but travels superluminally along the z axis and eventually catches up with it. Our measurements and simulations are in reasonable agreement although there is a discrepancy between the two intensities. This is most likely due to difference between the simulations and measurements such as our assumption that the beam before the aperture was a perfect Gaussian in both space and frequency, and that the aperture was a perfect circle.

In our next measurement, we made a hole in the beam by propagating it through a circular metal disk with a diameter of 4mm (see Fig. 8.5b and we measured the spatiotemporal field at different distances after the disk. Because this disk and the

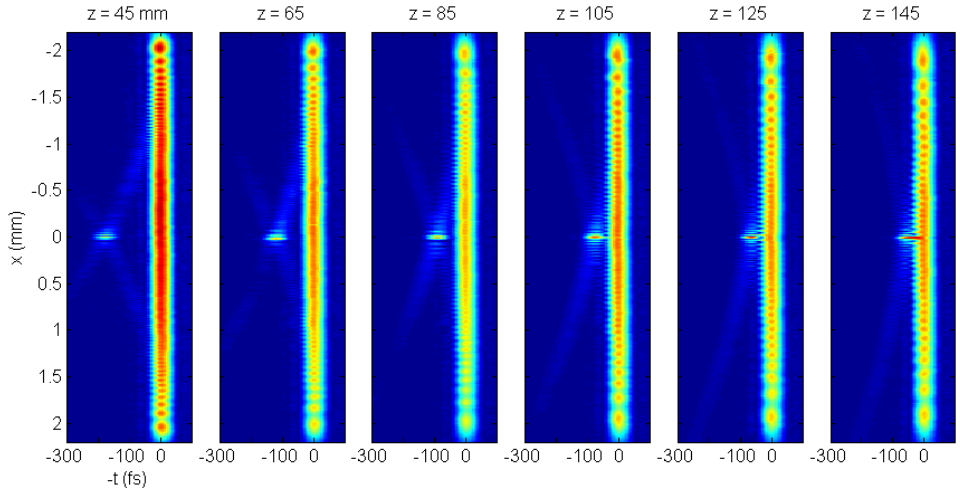

(a) Measurement

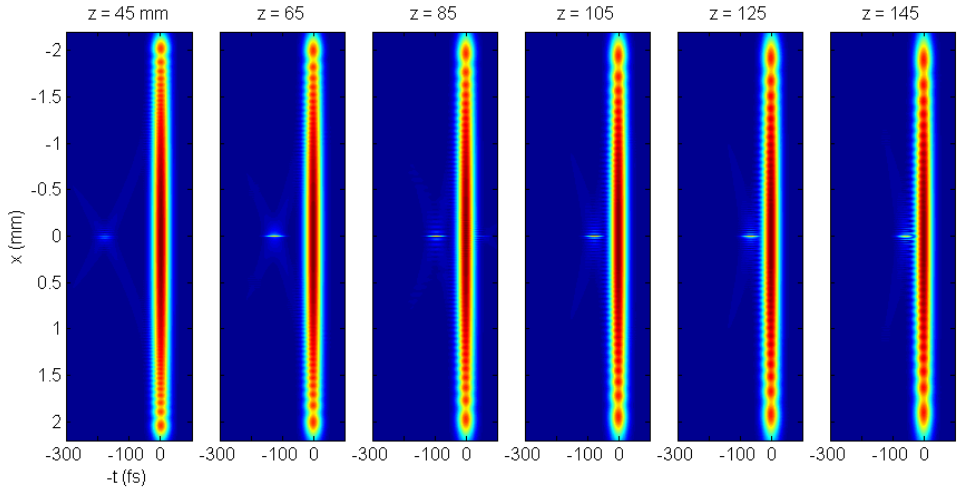

(b) Simulation

Figure 8.6: Measured $|E(x, y = 0, t)|$ after propagating through a circular aperture (Color is intensity).

aperture from the previous measurement have identical boundaries (both are circles with a diameter of 4mm), the boundary waves for these two cases should be identical. Therefore the only difference we expect between these two measurements is the contribution that comes from the main pulse front. The results of the measurements and simulations are shown in Fig. 8.7. This data shows a boundary pulse that is very

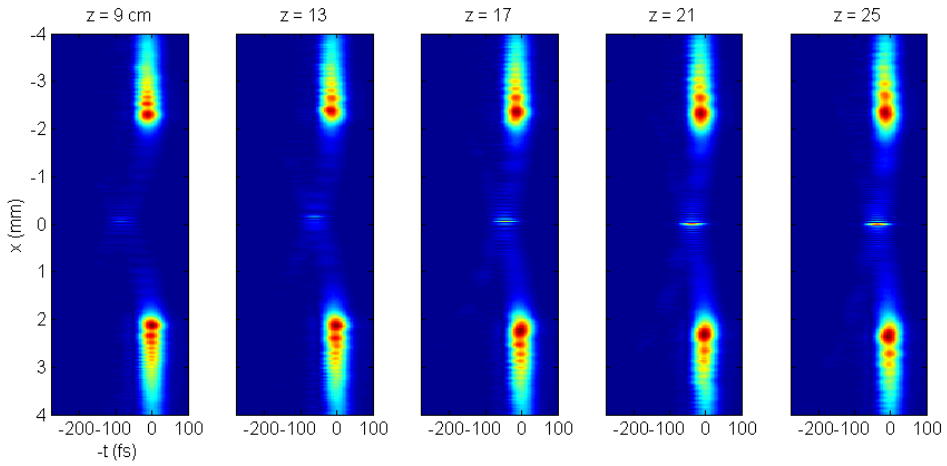

(a) Measurement

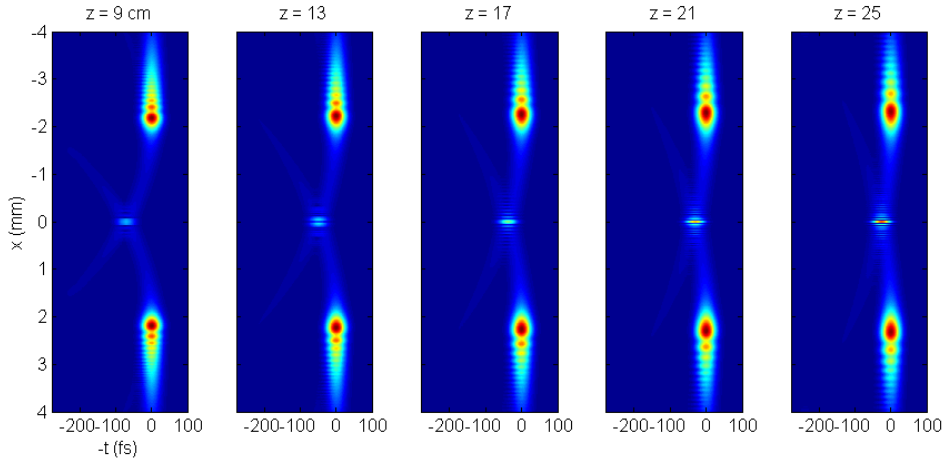

(b) Simulation

Figure 8.7: Measured $|E(x,t)|$ after propagating through a circular aperture (Color is intensity).

similar to that in Fig. 8.6, except that its intensity relative to the main pulse front is different as expected because this part of the pulse is different for the two cases. Note that the boundary wave for this example of diffraction is called the "spot of Arago"

in conventional diffraction theory.

The results shown in Fig. 8.6, show reasonable agreement between the simulations and the measurements, with the main discrepancy being the noise in the measurements. When measuring the field after the circular aperture (shown in Fig. 8.6) the main pulse front overlaps in space with the boundary wave, so these two fields interfere which effectively amplifies the boundary wave making it easier to measure. But with the disk the boundary wave and the main pulse front do not spatially overlap, so more sensitivity is required to measure this field, and it is barely detectable with our setup.

In a final measurement we propagated the pulse through a very thin annular slit with a diameter of 5.64mm and a width of around 10 μm such as that shown in Fig.8.8. If the slit is thin enough, then the non-diffracting contribution of the field is zero and there will only be the boundary wave. Although a slit contains two boundaries, if it is thin enough, then the two resulting boundary pulses will overlap in space and time. Therefore we expect to get results similar to that in the previous two measurements, but without a "main pulse front". Also, because this slit has a larger diameter than the disk or the aperture, its speed along the z axis should be grater than that seen in the two previous measurements.

The slit that we used for this measurement was made by coating a thin piece of glass with metal, but this metal coating was partially transmitting, so that 0.63% of the Gaussian beam illuminating it leaked through (see Fig. 8.5c). This is actually very convenient for two reasons: the Gaussian beam that leaks through travels at the speed of light, so it can be used as a reference to verify the speed of the boundary wave (even though our reference pulse already serves this purpose), and the Gaussian beam will interfere with the boundary wave which will amplify it making it easier to measure. The results of this measurement and our simulations are shown in Fig. 8.8. These results, which have the expected features discussed above, show good

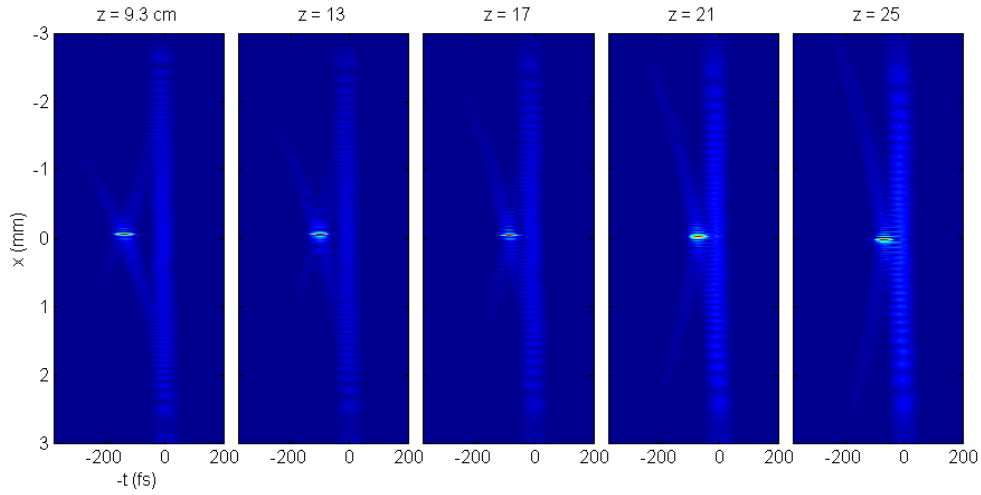

(a) Measurement

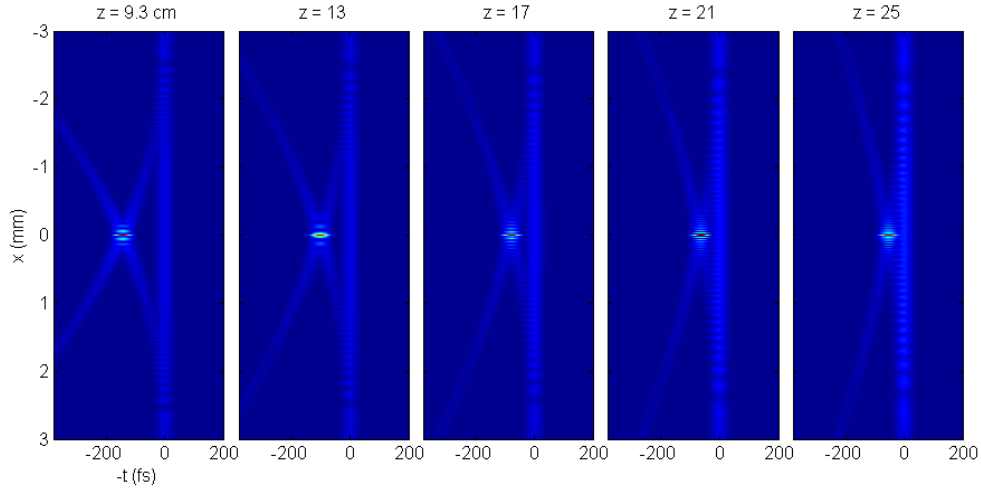

(b) Simulation

Figure 8.8: Measured $|E(x,t)|$ after propagating through a leaky annular slit.

agreement between the simulations and the measurements.

Actually two of the results shown in Chapter 6, contain boundary pulses. Figures 6.10 and 6.8, which show the measured spatiotemporal field after two different overfilled lenses both show an additional pulse which is temporally separated from the main pulse front. As you can see from the discussion in this chapter, these additional pulses are boundary wave pulses that are present because the lens' aperture is smaller than the beam. These measurements are similar to the results shown in Fig. 8.2b which show the diffraction of a pulse off of a circular aperture for a converging beam. But, in Fig. 6.10, the chromatic aberrations present in the lens change the phase of the spherical waves emitted at the boundary which causes it be ahead of the main pulse front rather than behind it as it is in the absence of abberations [15].

Also note that the boundary pulse is an interference effect and therefore it does not carry any information at a superluminal speed, so none of these results violate special relativity.

8.4 Conclusions

To our knowledge, we have made the first time resolved measurements of the diffraction of utlrashort pulses. Using SEA TADPOLE we measured the spatiotemporal field of ultrashort pulses after propagating them through a circular aperture, a circular disk and a leaky annular slit, and we confirmed these measurements with simulations. Our measurements reveal the superluminal propagation speed of the boundary wave pulse.

APPENDIX A

EXAMPLES OF SEA TADPOLE TRACES

As mentioned in chapter 2, the curvature of the interference fringes is the spectral phase difference between the reference and unknown pulses. This is illustrated by the simulations shown below. For these simulations the reference pulse had a flat spectral phase so that the curvature of the fringes (or the phase difference) is the phase of the unknown pulse. The spectra of the pulses has about 20nm of bandwidth. The spectral phase and intensity of the unknown pulses is shown below the interferograms.

Figure D.3a corresponds to an unknown pulse that is delayed with respect to the reference pulse or the spectral phase is linear (as well as the fringe curvature). In Fig. D.3b the unknown pulse was chirped and you can see that the fringes are parabolas.

Figure A.2a shows a pulse with a cubic spectral phase. In Fig. A.2b the unknown pulse with a quartic phase.

Figure A.3a shows a pulse with a sinusoidal phase. In Fig. A.3b the unknown pulse has a more complex spectrum and a quadratic spectral phase.

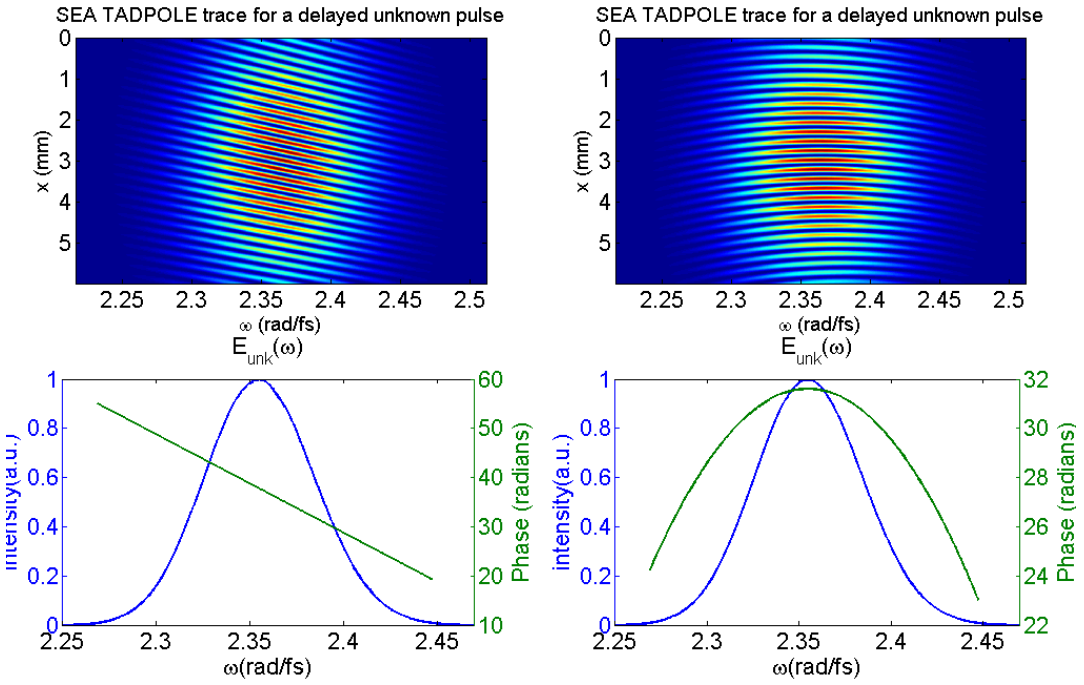

(a) Delay

(b) Chirp

Figure A.1: Example SEA TADPOLE traces (simulations)

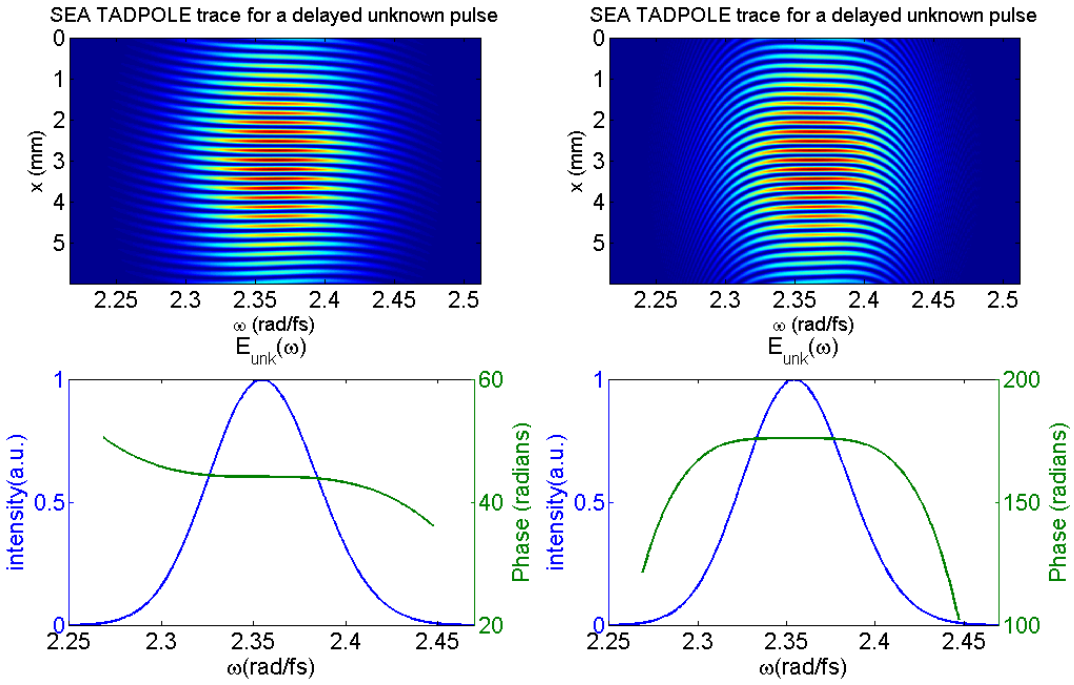

(a) Cubic phase

(b) Quartic phase

Figure A.2: Example SEA TADPOLE traces (simulations)

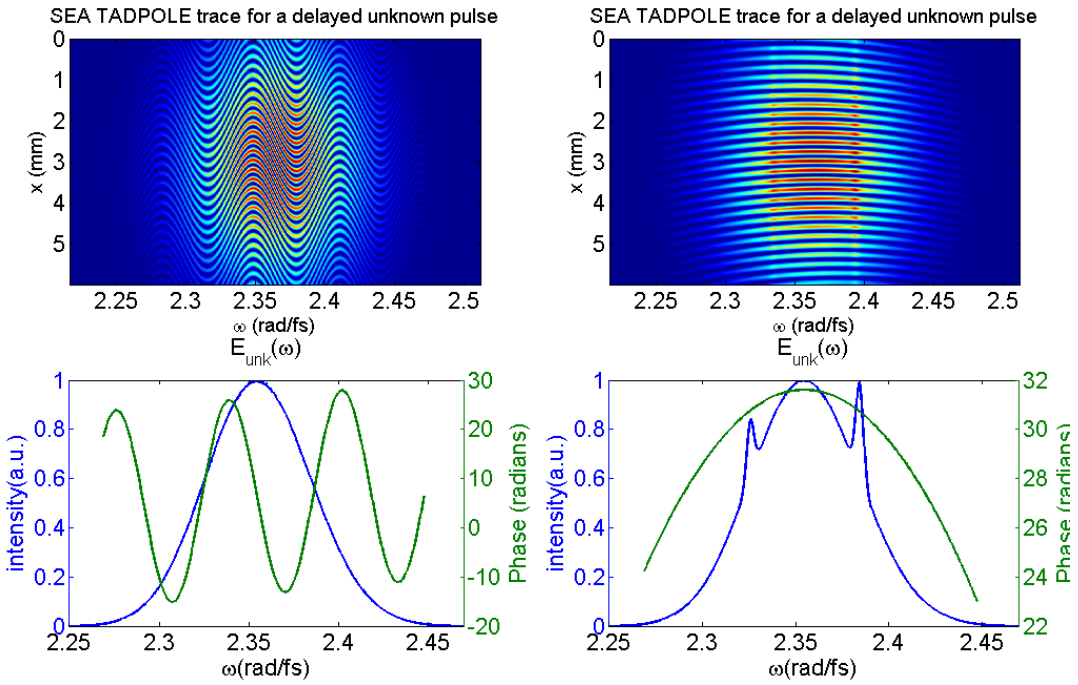

(a) Sinusoidal phase

(b) A more complex spectrum and a quadratic phase

Figure A.3: Example SEA TADPOLE traces (simulations)

APPENDIX B

ABSOLUTE PHASE DRIFT IN SEA TADPOLE

As discussed in chapter 5 and chapter 2, there is a drift in the interferometer due to primarily the fibers reacting to small temperature fluctuations. To better understand this drift and how it effect measurements that we make with SEA TADPOLE we measured this.

To measure the phase drift, we continuously measured the phase (or extracted it from a measured SEA TADPOLE trace) once a second over several minutes. Because we were not making any changes to the unknown pulse during this time, if no fluctuations were present then the measured phase would have been the same for every measurement, but this was of course not the case. To see how the phase drift effected each term in the measured spectral phase, we did a polynomial curve fit to each measured phase. Figure B.1 shows these results for the absolute phase, the delay and the group delay dispersion (GDD). The average value of the fluctuations for each

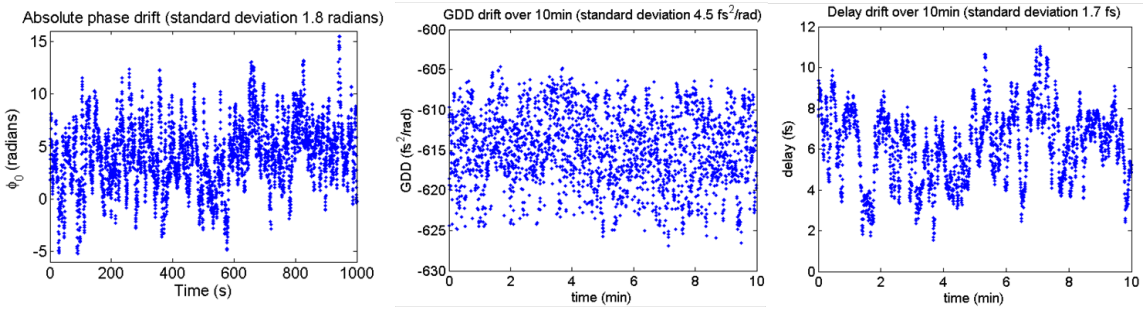

Figure B.1: Measured phase drift in our interferometer

of these phase terms is shown above the plots, and this is the error that we get for each of these terms for a typical measurement using our setup. Note that some of the fluctuation could be do to errors in the curve fit cause by noise, but nevertheless,

this gives an upper bound on the error due to the fluctuations.

The drift in the delay and the GDD were very small over 10min compared to values of GDD and delay that we are usually interested in measuring. And therefore, we can conclude that the phase drift does not effect these (and all higher order) terms.

But the absolute phase varies as much as ± 1.8 radians over 16.7min which is significant enough to effect certain applications of SEA TADPOLE including scanning SEA TADPOLE for measuring the absolute spatial phase (chapter 5) or for measuring the relative phase (chapter 4) of polarization shaped pulses.

In the next set of figures, the effect of the drift on the measured spatial phase in scanning SEA TADPOLE is illustrated. The plots were constructed from the data shown in 6.6 which involved focusing the pulse with an SF11 plano-convex lens having an NA of 0.28. Figure B.2 shows the measured and theoretical spatial phases (the absolute spectral phase at each x) at 0.3mm after the geometric focus. The noise due

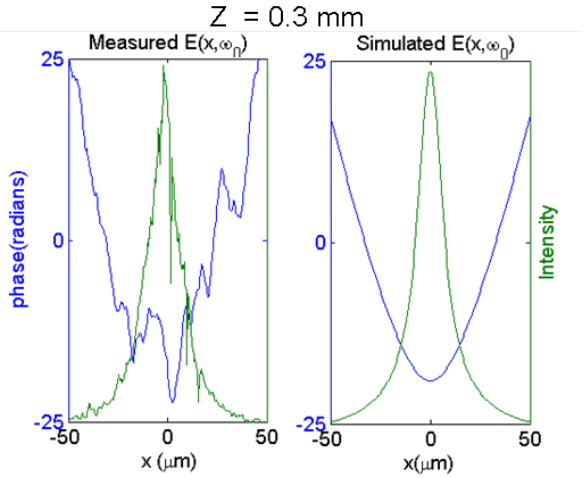

Figure B.2: Effect of the absolute phase drift on the measured spatial phase

to the fluctuations is apparent, but the shape of the measured phase resembles the theoretical phase. The next plot shows the measured and theoretical spatial phases at z=0.3mm, and these results are as accurate as those in B.3. In the final plot, which is closer to the beam's minimal spot size and therefore the point where its

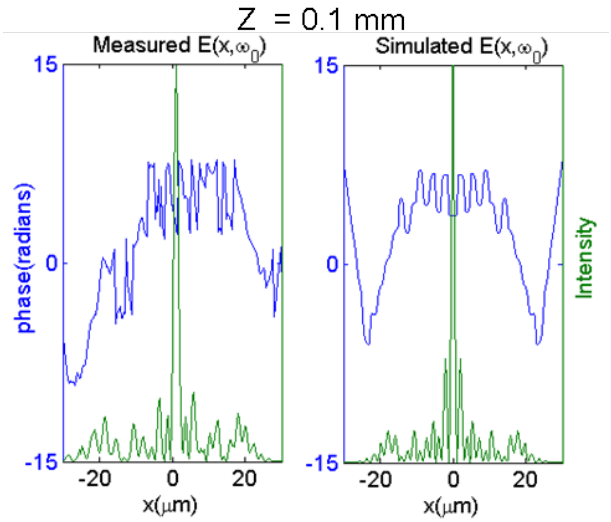

Figure B.3: Effect of the absolute phase drift on the measured spatial phase

spatial phase is the flattest, the results are not as good, and the measured spatial phase barely resembles the theoretical value. As the scale in this plot indicates, the spatial phase at this z only varies over about 6 radians compared to the previous two examples that varied over 50 and 30 radians. And therefore, the absolute phase's drift has more heavily distorted the results shown in Fig. B.4

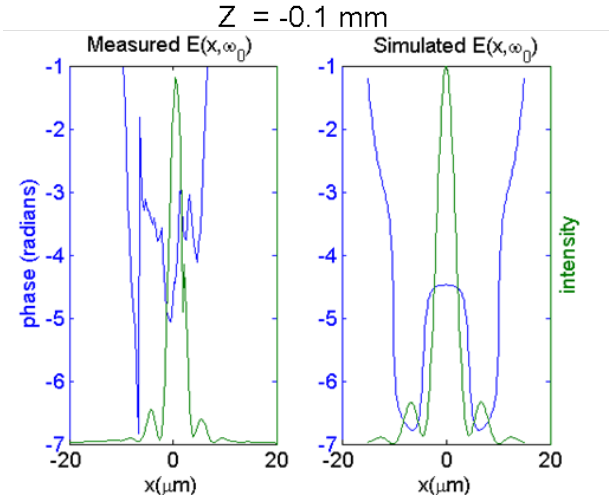

Figure B.4: Effect of the absolute phase drift on the measured spatial phase

While we have demonstrated that some spatial phase information is obtained in

a scanning SEA TADPOLE measurement (especially the spot size as a function of z), the measurements shown in Fig. B.2 and B.3 are still quite noisy. Due the large amounts of information obtained in scanning SEA TADPOLE measurement and the fact that we measure the field at several different z's, we expect that standard phase retrieval algorithms such as the Gerchberg-Saxton algorithm could be adapted and used to better extract the spatial phase from our measurements [121, 122]. In the future we hope to implement this .

APPENDIX C

POLARIZATION ELLIPSES

As mentioned in chapter 4, the polarization state of light can be represented as an ellipse [113]. Some of these ellipses for different polarization states are shown in Fig. C.1 where we have plotted E_x versus E_y from the equations shown below.

$$E_x = E_{x0}\cos(\phi_{rel} + \omega t) \tag{C.1}$$

$$E_y = E_{y0}\cos(\omega t) \tag{C.2}$$

To make plots of the polarization state of a pulse when its polarization state may be time dependent, we plot the ellipse at every time as show in section 4.4.

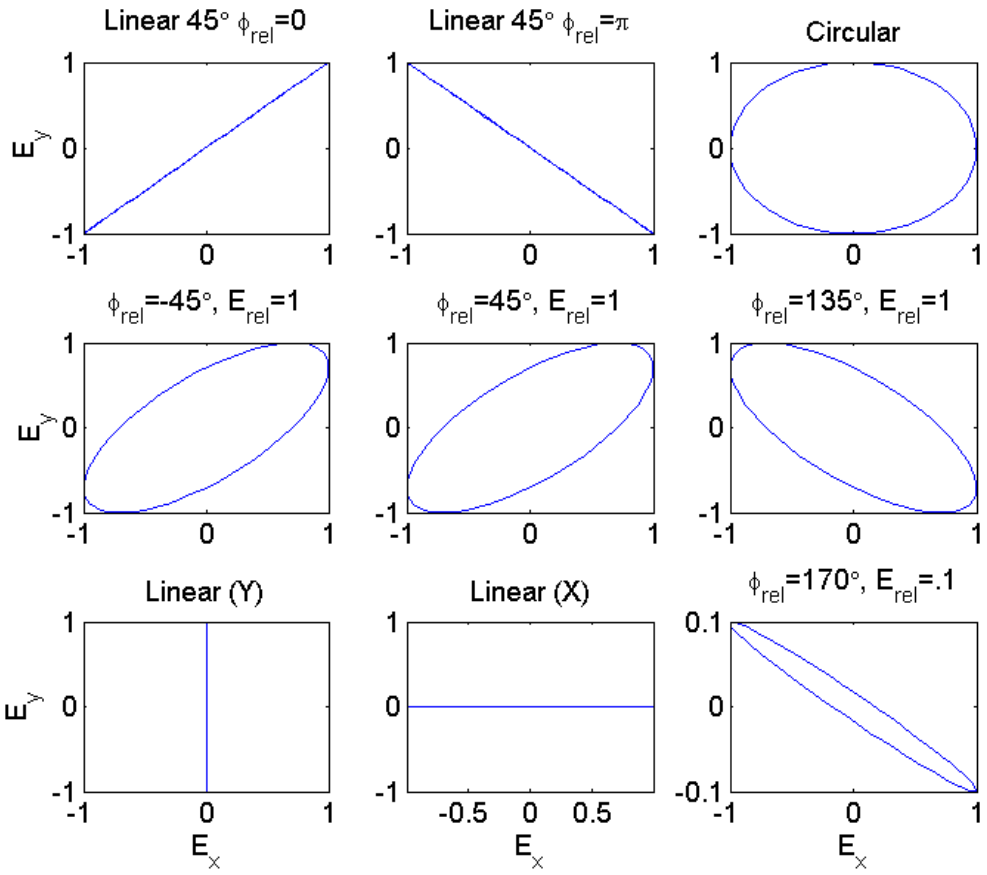

Figure C.1: Polarization eclipses for various polarization states

APPENDIX D

COMPARISON OF THE NON-PARAXIAL AND THE PARAXIAL DIFFRACTION INTEGRALS

We performed simulations to better understand the differences between the paraxial diffraction integral (or the Fresnel integral) described in Eq. 5.1, and the non-paraxial diffraction integral discussed in 6.7. Using the same parameters and the same grid size and spacing in both simulations, we calculated the $E(x,t)$ at several different z's in the focal region of a lens that had no spherical aberration and a little chromatic aberration. The results for a numerical aperture (NA) of 0.2 are shown below and only the amplitude is plotted (red is the most intense and blue is the least intense). The left plot shows the results of the paraxial simulation and the results of the non-

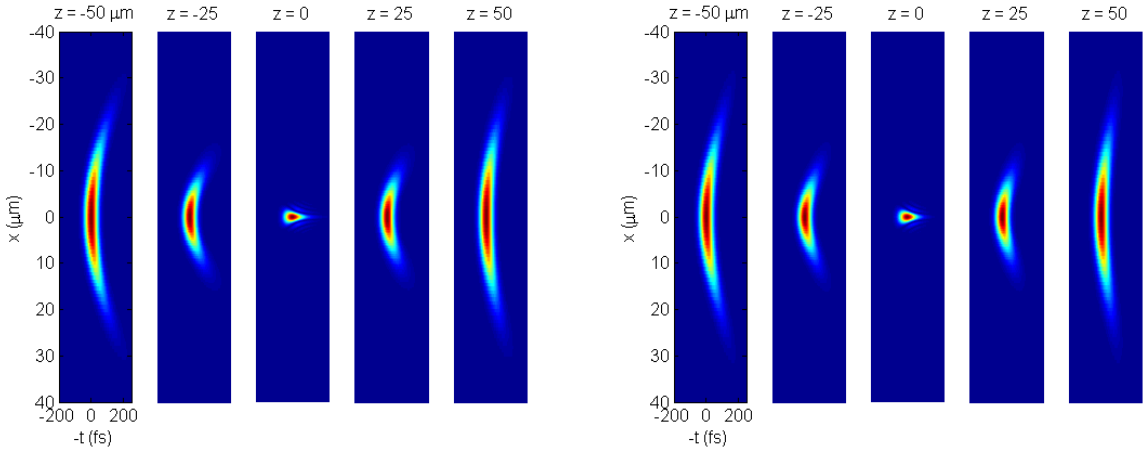

(a) paraxial

(b) Non-paraxial

Figure D.1: Simulations of the focal region of an aspheric lens with NA=0.2

paraxial simulation are on the right. At this NA, as we expect, the two simulations give the same results. The Next set of figures shows similar results except that the

numerical aperture was 0.4. In these plots, some differences are noticeable such as

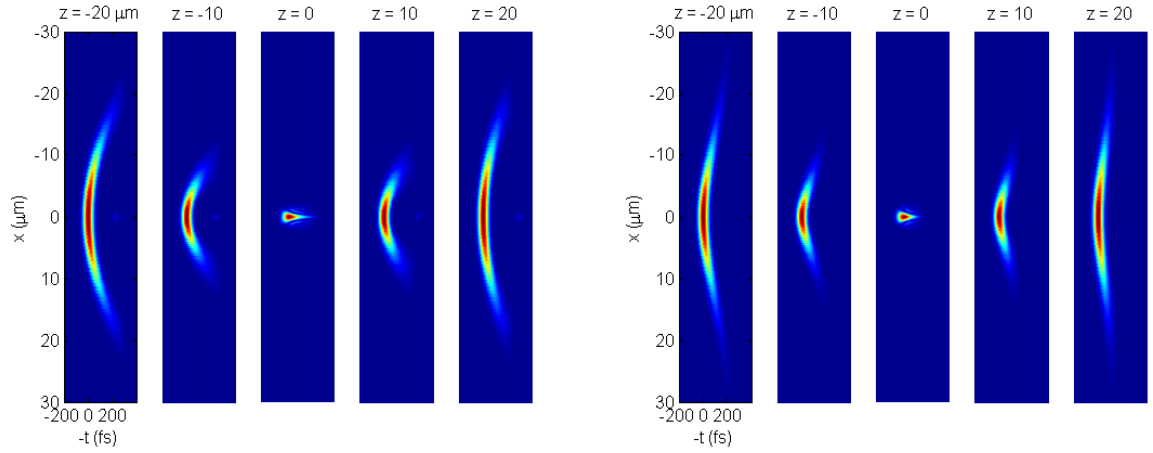

(a) paraxial (b) Non-paraxial

Figure D.2: Simulations of the focal region of an aspheric lens with NA=0.4

more intensity in the wings in the non-paraxial simulation and an additional fore runner (a pre pulse) is apparent in the paraxial simulation. In this simulation the beam's rms spot size was 3mm and the aperture diameter was 10mm, but the edge effects are more apparent in the non-paraxial simulation. To final set of plots shown below, we used an NA of 0.8, and the two simulations give very different results as we expect. The effect of the paraxial simulation is to underestimate the intensity in the wings which is again apparent in the above plot. And as we were beginning to for the NA=0.4 simulation, as the paraxial approximation breaks down, the effects of diffraction off of the lens' aperture become too bright.

In conclusion, for numerical apertures around 0.4 and greater, a non-paraxial simulation should be used.

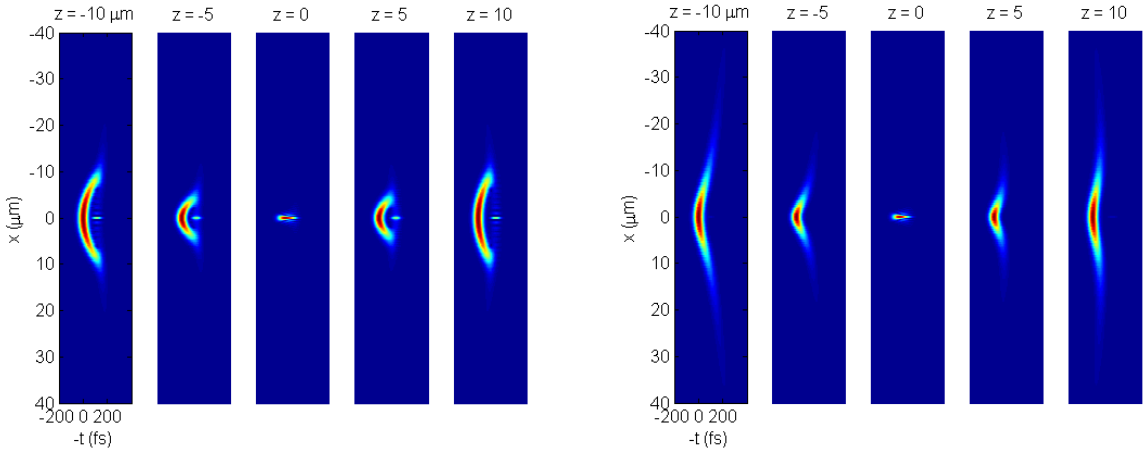

(a) paraxial

(b) Non-paraxial

Figure D.3: Simulations of the focal region of an aspheric lens with NA=0.8

Bibliography

[1] A. Braun, G. Korn, X. Liu, D. Du, J. Squier, and G. Mourou, "Self-channeling of high-peak-power femtosecond laser pulses in air," SPRINGER SERIES IN CHEMICAL PHYSICS **60**, 248–248 (1994).

[2] Z. Chang, A. Rundquist, H. Wang, M. Murnane, and H. Kapteyn, "Generation of Coherent Soft X Rays at 2.7 nm Using High Harmonics," Physical Review Letters **79**, 2967–2970 (1997).

[3] C. Schaffer, A. Brodeur, J. García, and E. Mazur, "Micromachining bulk glass by use of femtosecond laser pulses with nanojoule energy," Optics Letters **26**, 93–95 (2001).

[4] W. Denk, J. Strickler, and W. Webb, "Two-photon laser scanning fluorescence microscopy," Science **248**, 73–76 (1990).

[5] T. Udem, R. Holzwarth, and T. Haensch, "Optical frequency metrology," Nature **416**, 233–237 (2002).

[6] T. Brixner and G. Gerber, "Femtosecond polarization pulse shaping," Optics Letters **26**, 557–559 (2001).

[7] T. Brixner, N. Damrauer, G. Krampert, P. Niklaus, and G. Gerber, "Adaptive shaping of femtosecond polarization profiles," Journal of the Optical Society of America B **20**, 878–881 (2003).

[8] T. Brixner, G. Krampert, T. Pfeifer, R. Selle, G. Gerber, M. Wollenhaupt, O. Graefe, C. Horn, D. Liese, and T. Baumert, "Quantum Control by Ultrafast Polarization Shaping," Physical Review Letters **92**, 208301 (2004).

[9] M. Plewicki, F. Weise, S. Weber, and A. Lindinger, "Phase, amplitude, and polarization shaping with a pulse shaper in a Mach-Zehnder interferometer," Applied Optics **45**, 8354–8359 (2006).

[10] D. Oron and Y. Silberberg, "Spatiotemporal coherent control using shaped, temporally focused pulses," Optics Express **13**, 9903–9908 (2005).

[11] A. Zewail, *Femtochemistry: Ultrafast Dynamics of the Chemical Bond* (World Scientific, 1994).

[12] R. Trebino, *Frequency-Resolved Optical Gating: The Measurement of Ultrashort Laser Pulses* (Kluwer Academic Publishers, 2002).

[13] R. Trebino and D. Kane, "Using phase retrieval to measure the intensity and phase of ultrashort pulses: frequency-resolved optical gating," Journal of the Optical Society of America A **10**, 1101–1101 (1993).

[14] R. Levis, G. Menkir, and H. Rabitz, "Selective bond dissociation and rearrangement with optimally tailored, strong-field laser pulses," Science **292**, 709–713 (2001).

[15] U. Fuchs, U. D. Zeitner, and A. Tuennermann, "Ultra-short pulse propagation in complex optical systems," Optics Express **13**, 3852–3861 (2005).

[16] P. Saari, K. Reivelt, and H. Valta, "Ultralocalized superluminal light pulses," Laser Physics **17**, 297–301 (2007).

[17] R. Paschotta and U. Keller, "Passive mode locking with slow saturable absorbers," Applied Physics B: Lasers and Optics **73**, 653–662 (2001).

[18] K. Sheetz, E. Hoover, R. Carriles, D. Kleinfeld, and J. Squier, "Advancing multifocal nonlinear microscopy: development and application of a novel multibeam Yb: KGd (WO_4) _2 oscillator," Optics Express **16**, 17574–17584 (2008).

[19] J. Kafka, M. Watts, and J. Pieterse, "Picosecond and femtosecond pulse generation in a regeneративelymode-locked Ti: sapphire laser," Quantum Electronics, IEEE Journal of **28**, 2151–2162 (1992).

[20] J. Herrmann, "Theory of Kerr-lens mode locking: role of self-focusing and radially varying gain," laser **1**, 6.

[21] E. Ippen, "Principles of passive mode locking," Applied Physics B: Lasers and Optics **58**, 159–170 (1994).

[22] O. E. Martinez, J. P. Gordon, and R. L. Fork, "Negative group-velocity dispersion using refraction," Journal of the Optical Society of America A **1**, 1003–1006 (1984).

[23] E. Treacy, "Optical pulse compression with diffraction gratings," Quantum Electronics, IEEE Journal of **5**, 454–458 (1969).

[24] A. Baltuska, Z. Wei, M. Pshenichnikov, and D. Wiersma, "Optical pulse compression to 5 fs at a 1-MHz repetition rate," Optics Letters **22**, 102–104 (1997).

[25] M. Pessot, J. Squier, P. Bado, G. Mourou, and D. Harter, "Chirped pulse amplification of 300 fs pulses in an alexandriteregenerative amplifier," Quantum Electronics, IEEE Journal of **25**, 61–66 (1989).

[26] I. Jovanovic, B. Comaskey, C. Ebbers, R. Bonner, D. Pennington, and E. Morse, "Optical parametric chirped-pulse amplifier as an alternative to Ti: sapphire regenerative amplifiers," APPLIED OPTICS **41**, 2923–2929 (2002).

[27] S. Akturk, X. Gu, P. Gabolde, and R. Trebino, "The general theory of first-order spatio-temporal distortions of gaussian pulses and beams," Optics Express **13**, 8642–8661 (2005).

[28] X. Gu, S. Akturk, and R. Trebino, "Spatial chirp in ultrafast optics," Optics Communications **242**, 599–604 (2004).

[29] S. Akturk, X. Gu, E. Zeek, and R. Trebino, "Pulse-front tilt caused by spatial and temporal chirp," Opt. Expr. **12**, 4399 – 4410 (2004).

[30] C. Iaconis and I. Walmsley, "Self-referencing spectral interferometry for measuring ultrashortoptical pulses," Quantum Electronics, IEEE Journal of **35**, 501–509 (1999).

[31] V. Wong and I. Walmsley, "Analysis of ultrashort pulse-shape measurement using linear interferometers," Optics Letters **19**, 287–287 (1994).

[32] L. Xu, E. Zeek, and R. Trebino, "Simulations of frequency-resolved optical gating for measuring very complex pulses," Journal of the Optical Society of America B **25**, A70–A80 (2008).

[33] D. N. Fittinghoff, J. L. Bowie, J. N. Sweetser, R. T. Jennings, M. A. Krumbgel, K. W. DeLong, R. Trebino, and I. A. Walmsley, "Measurement of the intensity and phase of ultraweak, ultrashort laser pulse," Opt. Lett. **21**, 884–886.

[34] P. OShea, M. Kimmel, X. Gu, and R. Trebino, "Highly simplified device for ultrashort-pulse measurement," Optics Letters **26**, 932–934 (2001).

[35] P. OShea, S. Akturk, M. Kimmel, and R. Trebino, "Practical issues in ultrashort-pulse measurements with GRENOUILLE," Applied Physics B: Lasers and Optics **79**, 683–691 (2004).

[36] A. Assion, T. Baumert, M. Bergt, T. Brixner, B. Kiefer, V. Seyfried, M. Strehle, and G. Gerber, "Control of chemical reactions by feedback-optimized phase-shaped femtosecond laser pulses," Science **282**, 919–922 (1998).

[37] W. Warren, H. Rabitz, and M. Dahleh, "Coherent Control of Quantum Dynamics: The Dream Is Alive," Science **259**, 1581–1589 (1993).

[38] R. Judson and H. Rabitz, "Teaching lasers to control molecules," Physical Review Letters **68**, 1500–1503 (1992).

[39] N. Dudovich, D. Oron, and Y. Silberberg, "Single-pulse coherently controlled nonlinear raman spectroscopy and microscopy," Nature **418**, 512–514 (2002).

[40] D. Meshulach and Y. Silberberg, "Coherent quantum control of two-photon transitions by a femtosecond laser pulse," Nature **396**, 239–42 (1998).

[41] X. Gu, L. Xu, M. Kimmel, E. Zeek, P. O'Shea, A. Shreenath, R. Trebino, and R. Windeler, "Frequency-resolved optical gating and single-shot spectral measurements reveal fine structure in microstructure-fiber continuum," Opt. Lett. **27**, 1174–6 (2002).

[42] J. J. Field, T. A. Planchon, W. Amir, C. G. Durfee, and J. A. Squier, "Characterization of a high efficiency, ultrashort pulse shaper incorporating a reflective 4096-element spatial light modulator," Optics Express **287**, 368–376.

[43] T. Ohno, K. Okamoto, T. Yamanaka, M. Kannari, and F. Tanabe, "Feedback control for accurate shaping of ultrashort opticsal pulses prior to chirped pulse amplification," Japanese Journal of Applied Physics **43**, 1366–75 (2004).

[44] J. Geindre, P. Audebert, S. Rebibo, and J. Gauthier, "Frequency-domain interferometer for measuring the phase and amplitude of a femtosecond pulse probing a laser-produced plasma," Optics Letters **19**, 1997–1999 (1994).

[45] H. Gersen, E. van Dijk, J. Korterik, N. van Hulst, and L. Kuipers, "Phase mapping of ultrashort pulses in bimodal photonic structures: A window on local group velocity dispersion," Physical Review E **70**, 066609 (2004).

[46] C. Froehly, A. Lacourt, and J. C. Vienot, "Time impulse responce and time frequency responce of optical pupils," Nouvelle Revue D'Optique **4**, 183–196.

[47] L. Lepetit and M. Joffre, "Two-dimensional nonlinear optics using fourier-transform spectral interferometry," Opts. Lett. **21**, 564–566 (1996).

[48] C. Dorrer, "Influence of the calibration of the detector on spectral inteferometry," Journal of the Optical Society of America B **16**, 1160–1168 (1999).

[49] J. Geindre, P. Audebert, A. Rousse, F. Falliés, J. Gauthier, A. Mysyrowicz, A. Dos Santos, G. Hamoniaux, and A. Antonetti, "Frequency-domain interferometer for measuring the phase of a femtosecond pulse probing a laser-produced plasma," Opt. Lett. **19**, 1997–1999 (1994).

[50] P. Bowlan, P. Gabolde, M. A. Coughlan, R. Trebino, and R. J. Levis, "Measuring the spatiotemporal electric field of ultrashort pulses with high spatial and spectral resolution," Journal of the Optical Society of America B **25**, A81–A92 (2008).

[51] P. Bowlan, P. Gabolde, A. Schreenath, K. McGresham, and R. Trebino, "Crossed-beam spectral interferometry: a simple, high-spectral-resolution method for completely characterizing complex ultrashort pulses in real time," Optics Express **14**, 11892–11900 (2006).

[52] A. Kovaecs, K. Osvay, G. Kurdi, M. Gorbe, J. Klenbniczki, and Z. Bor, "Dispersion control of a pulse stretcher-compressor system with two-dimensional spectral interferometry," Applied Physics B **80**, 165–170 (2005).

[53] A. P. Kovaecs, K. Osvay, and Z. Bor, "Group-delay measurement on laser mirrors by spectrally resolved white-light interferometry," Optics Letters **20**, 788–791.

[54] E. M. Kosik, A. S. Radunsky, I. Walmsley, and C. Dorrer, "Interferometric technique for measuring broadband ultrashort pulses at the sampling limit," Optics Letters **30**, 326–328.

[55] P. Bowlan, P. Gabolde, and R. Trebino, "Directly measuring the spatio-temporal electric field of focusing ultrashort pulses," Optics Express **15**, 10219–30 (2007).

[56] K. Wicker and R. Heintzmann, "Interferometric resolution improvement for confocal microscopes," Opt. Express **15**, 12206–12216.

[57] P. A. Jansson, "Method for determining the response funcion of a high-resolution infrared spectrometer," Journal of the optical Society of America **60**, 184–191 (1970).

[58] P. A. Jansson, *Deconvolution with Applications in Spectroscopy* (Academic Press INC., 1984).

[59] V. J. Coates and H. Hausdorff, "Interferometeric methid of measuring the spectral slit width if spectrometers," Journal of the optical Society of America **45**, 425–430 (1955).

[60] V. N. Kumar and D. N. Rao, "Determiniation of the instrument function of a grating spectrometer by using white-light interferometry," Appl. Opt. **36**, 4535–4539.

[61] Z. Chang, "Single attosecond pulse and xuv supercontinuum in the high-order harmonic plateau," Physical Review A **70**, 43802 (2004).

[62] O. Masihzadeh, P. Schlup, and R. Bartels, "Complete polarization state control of ultrafast laser pulses with a single linear spatial light modulator," Optics Express **15**, 18025–18032 (2007).

[63] P. Schlup, O. Masihzadeh, L. Xu, R. Trebino, and R. Bartels, "Tomographic retrieval of the polarization state of an ultrafast laser pulse," Optics Letters **33**, 267–269 (2008).

[64] H. Gersen, J. Korterik, N. van Hulst, and L. Kuipers, "Tracking ultrashort pulses through dispersive media: Experiement and theory," Physical Review E **68**, 026604 (2003).

[65] M. Plewicki, "Phase, amplitude, and polarization pulse shaping in order to influence molecular processes," Ph.D. thesis, Freien Universitat Berlin, Berlin, Germany (2006).

[66] M. Kempe, U. Stamm, B. Wilhelmi, and W. Rudolph, "Spatial and temporal transformation of femtosecond laser pulses by lenses and lens systems," Journal of the Optical Society of America B **9**, 1158–1165 (1992).

[67] M. Kempe and W. Rudolph, "Impact of chromatic and spherical aberration on the focusing of ultrashort light pulses by lenses," Optics Letters **18**, 137–9 (1993).

[68] Z. Bor, "Distortion of femtosecond laser pulses in lenses," Optics Letters **14**, 119–121 (1989).

[69] F. Quercioli, B. Tiribilli, M. Vassalli, and F. Sbrana, "Autocorrelator designs for nonlinear optical microscopy," Optical Engineering **45** (2006).

[70] M. Mueller, J. Squier, and G. Brakenhoff, "Measurement if femtosecond pulses in the focal point of a high-numerical-aperature lens by two-photon absorption," Optics Letters **20**, 1038–1040 (1995).

[71] V. V. Lozovoy, I. Pastirk, and M. Dantus, "Multiphoton intrepulse interference. iv. ultrashort pulse spectral phase characterization and compensation," Opt. Lett. **29**, 775–777.

[72] D. N. Fittinghoff, J. A. Squier, C. P. J. Barty, J. N. Sweetser, R. Trebino, and M. Mueller, "Collinear type ii second-harmonic-generation frequency-resolved optical gating for use with high-numerical-aperture objectives," Opt. Lett. **23**, 1046–1048.

[73] R. Chadwick, E. Spahr, J. A. Squier, and C. G. Durfee, "Fringe-free, background-free, collinear third-harmonic generation frequency-resolved optical gating measurements for multiphoton microscopy," Optics Letters **31**, 3366–3368 (2006).

[74] D. N. Fittinghoff, A. C. Millard, J. A. Squier, and M. Mueller, "Frequency-resolved optical gating measurement of ultrashort pulses passing through a high numerical aperture objective," IEEE J. Quantum Electron. **35**.

[75] J. Jasapara and W. Rudolph, "Characterization of sub-10-fs pulse focusing with high-numerical-aperture microscope objectives," Optics Letters **24**, 777–779 (1999).

[76] W. Amir, T. A. Planchon, C. G. Durfee, J. A. Squier, P. Gabolde, R. Trebino, and M. Mueller, "Simultaneous visualizations of spatial and chromatic abberations by two-dimensional fourier transform spectral interferometry," Optics Letters **31**, 2927–2929 (2006).

[77] M. Balistreri, J. Korterik, L. Kuipers, and N. van Hulst, "Phase mapping of optical fields in integrated optical waveguide structures," Journal of Lightwave technology **19**, 1169 (2001).

[78] M. Balistreri, H. Gersen, J. Korterik, L. Kuipers, and N. van Hulst, "Tracking femtosecond laser pulses in space and time," Science **294** (2001).

[79] A. E. Siegman, *Lasers* (University Science Books, 1986).

[80] J.W.Goodman, *Introduction to Fourier Optics* (New York: McGraw Hill, 1996).

[81] M. Kempe and W. Rudolph, "Femtosecond pulses in the focal region of lenses," Physical Review A **48**, 4721–4729 (1993).

[82] M. Born and E. Wolf, *Principles of Optics* (Pergamon, London, 1989).

[83] Z. Bor, Z. Gogolak, and G. Szabo, "Femtosecond-resolution pulse-front distortion measurement by time-of-flight interferometry," Optics Letters **14**, 862–864 (1989).

[84] W. Amir, T. Planchon, C. Durfee, and J. Squier, "Complete characterization of a spatiotemporal pulse shaper with two-dimensional fourier transform spectral interferometry," Optics Letters **32**, 939–941 (2007).

[85] Z. Bor and B. Racz, "Group velocity dispersion in prisms and its application to pulse compression and travelling-wave excitation," Optics Communications **54**, 165–170 (1985).

[86] S. Akturk, M. Kimmel, P. O'Shea, and R. Trebino, "Measuring pulse-front tilt in ultrashort pulses using grenouille," Opt. Expr. **11**, 491–501 (2003).

[87] S. Akturk, M. Kimmel, P. O'Shea, and R. Trebino, "Measuring spatial chirp in ultrashort pulses using single-shot frequency-resolved optical gating," Opt. Expr. **11**, 68–78 (2003).

[88] A. Kostenbauder, "Ray-pulse matrices: A rational treatment for dispersive optical systems," IEEE J. Quant. Electron. **26**, 1148–1157 (1990).

[89] I. P. Radko, S. I. Bozhevolnyi, and N. Gregersen, "Transfer funcion and near-field detection of evanescent waves," Applied Optics **45**, 4054–4061 (10 June 2006).

[90] J. Buck, *Fundamentals of Optical Fibers, Pure and Applied Optics* (John Wiley and Sons, Inc., 2004).

[91] D. Marcuse, "Loss analysis of a single-mode fiber splices," The Bell System Technical Journal **56**, 703–717 (1976).

[92] P. Bowlan, U. Fuchs, R. Trebino, and U. D. Zeitner, "Measuring the spatiotemporal electric field of tightly focused ultrashort pulses with sub-micron spatial resolution," Optics Express **16**, 13663–13675 (2008).

[93] Z. Bor, "Distortion of femtosecond laser pulses in lenses and lens systems," J. Mod. Opt. **35**, 1907–1918 (1988).

[94] Z. Bor and Z. Horvath, "Distortion of femtosecond pulses in lenses. wave-optical description," Opt. Comm. **94**, 249–258 (1992).

[95] P. Saari, "Evolution of subcycle pulses in nonparaxial gaussian beams," Optics Express **8**, 590–598 (2001).

[96] S. Feng and H. G. Winful, "Spatiotemporal structure of isodiffracting ultrashort electromagnetic pulses," Phys. Rev. E **61**, 862–873 (2000).

[97] Z. Horvath, Z. Benko, and A. Kovacs, "Propagation of femtosecond pulses through lenses, gratings, and slits," Opt. Eng. **32**, 2491–2500 (1993).

[98] E. Betzig, M. Isaacson, and A. Lewis, "Collection mode near-field scanning optical microscopy," Applied Physics Letters **51**, 2088–2090 (1987).

[99] E. Betzig, J. K. Trautman, T. D. Harris, J. S. Weiner, and R. L. Kostelak, "Breaking the diffraction barrier: Optical microscopy of a nanometer scale," Science **251**, 1468–1470 (1991).

[100] Y. H. Fu, F. H. Ho, W. C. Lin, W. C. Liu, and D. P. Tsau, "Study of the focused laser spots generated by various polarized laser beam conditions," J. Microsc. **201**, 225–228 (2002).

[101] U. Fuchs and U. D. Zeitner, *Focusing ultrashort pulses* (preprint).

[102] Y.M.engelberg and S. Ruschin, "Fast method for physical optics propagation of high numerical-aperture beams," J. Opt. Soc. Am. A **1**, 2135–2145 (2004).

[103] E. Weisstein, "Wolfram math world, hankel transform," (2009). `http://mathworld.wolfram.com/HankelTransform.html`.

[104] A. Lewis, U. Ben-Ami, N. Kuck, G. Fish, D. Diamant, L. Lubovsky, K. Lieberman, S. Katz, A. Saar, and M. Roth, "Nsom the fourth dimension: Integrating nanometric spatial and femtosecond time resolution," Scanning **17**, 3–10 (1995).

[105] B. A. Nechay, U. Siegner, M. Achermann, H. Bielefeld, and U. Keller, "Femtosecond pump-probe near-field optical microscopy," Review of Scientific Instruments **70**, 2758–2764 (1999).

[106] L. R. Corporation, "Oslo optical design program," (2004).

[107] K. Reivelt and P. Saari, "Linear-optical generation of localized waves," in "Localized waves," , H. E. Hernndez-Figueroa, M. Zamboni-Rached, and E. Recami, eds. (Wiley, 2007).

[108] H. Sonajalg and P. Saari, "Suppression of temporal spread of ultrashort pulses in dispersive media by Bessel beam generators," Optics Letters **21**, 1162–1164 (1996).

[109] X. Tsampoula, V. Garces-Chavez, M. Comrie, D. Stevenson, B. Agate, C. Brown, F. Gunn-Moore, and K. Dholakia, "Femtosecond cellular transfection using a nondiffracting light beam," Applied Physics Letters **91**, 053902 (2007).

[110] P. Saari and K. Reivelt, "Generation and classification of localized waves by Lorentz transformations in Fourier space," Physical Review. E, Statistical Physics, Plasmas, Fluids, and Related Interdisciplinary Topics **69** (2004).

[111] P. Saari and K. Reivelt, "Evidence of X-shaped propagation-invariant localized light waves," Physical Review Letters **79**, 4135–4138 (1997).

[112] I. Alexeev, K. Kim, and H. Milchberg, "Measurement of the Superluminal group velocity of an ultrashort Bessel beam pulse," Physical review letters **88**, 59 (2002).

[113] E. Hecht, A. Zajac, V. Martynov, and J. Selichov, *Optics* (Addison-Wesley Reading, Mass, 1998).

[114] Z. Horváth and Z. Bor, "Diffraction of short pulses with boundary diffraction wave theory," Physical Review E **63**, 26601 (2001).

[115] A. Rubinowicz, "Thomas Young and the theory of diffraction," Nature **180**, 160–162 (1957).

[116] K. Miyamoto and E. Wolf, "Generalization of the Maggi-Rubinowicz theory of the boundary diffraction wavePart II," J. Opt. Soc. Am **52**, 626–637 (1962).

[117] K. Miyamoto and E. Wolf, "Generalization of the Maggi-Rubinowicz theory of the boundary diffraction wave Part I, Opt Ž," Soc Amer **52**, 615 (1962).

[118] Z. Horváth, J. Klebniczki, G. Kurdi, and A. Kovács, "Experimental investigation of the boundary wave pulse," Optics Communications **239**, 243–250 (2004).

[119] W. Amir, C. Durfee, D. Schafer, E. Gibson, L. Kost, E. Przekwas, R. Jimenez, and J. Squier, "Linear spatio-temporal characterization of a UV microscope objective for nonlinear imaging and spectroscopy by using two-dimensional spectral interferometry," Journal of Microscopy **230**, 4–8 (2008).

[120] M. Guizar-Sicairos and J. Gutiérrez-Vega, "Computation of quasi-discrete Hankel transforms of integer order for propagating optical wave fields," Journal of the Optical Society of America A **21**, 53–58 (2004).

[121] R. W. Gerchberg and W. O. Saxton, "A practical algorithm for the determination of the phase from image and diffraction plane pictures," Optik **35**, 237–46 (1972).

[122] R. W. Gerchberg and W. O. Saxton, "Phase determination from image and diffraction plane pictures in the electron microscope," Optik **34**, 275–84 (1998).